LATVIAN JOURNAL of PHYSICS and TECHNICAL SCIENCES

ISSN 0868 - 8257

1

(Vol. 54)

2017

Ind. pasūt. € 1,50 Indekss 2091
Org. € 15,00 Indekss 2092

SATURS

ENERĢĒTIKAS FIZIKĀLĀS UN TEHNISKĀS PROBLĒMAS

Kudrjavtsev O., Kallaste A., Kilk A., Vaimann T., Orlova S.
Pastāvīgo magnētu materiāla mainīguma ietekme uz vēja ģeneratora darbību 3
Serebrjakovs A., Levins N., Kamoliņš E., Mileiko M.
Induktormašīnas ar gareniski-transversālām ķemmveida zobu zonām 12
Lavrinoviča L., Dirba J., Dobrijans R. *Ārējā rotora izstrāde sinhronajam reaktīvajam dzinējam ar samazinātām momenta pulsācijām* 23
Fedotovs A., Fedotovs E., Bahtejevs K. *Sinhrono mašīnu ar vārstu ierosmes sistēmām matemātiskā modelēšana, izmantojot vietējo Furjē transformāciju* 31

CIETVIELU FIZIKA

Krasovska M., Gerbreders V., Tamanis E., Gerbreders S., Bulanovs A.
Svina jonu adsorbcijas procesu analīze uz labi sakārtotu ZnO cauruļu virsmas 41

FIZIKA

Krupeņins V., Vība J. *Ne Ņūtona vibrotrieciena procesu analīze cauruļu konstrukcijās un paralēlu trieciena pāru sistēmās* 51
Kanders U., Kanders K. *Vakuuma pārklājumu substrātu nanoindentēšanas datu analīze-1: Deformācijas gradienta-diverģences metode* 66

Price to individual subscribers € 1.50/issue Index 2091
Price to collective subscribers € 15.00/issue Index 2092

CONTENTS

PHYSICAL AND TECHNICAL ENERGY PROBLEMS

Kudrjavtsev O., Kallaste A., Kilk A., Vaimann T., Orlova S. *Influence of permanent magnet characteristic variability on the wind generator operation* 3
Serebryakov A., Levin N., Kamolins E., Mileiko M. *Inductor machines with longitudinally-transversal comb-wise tooth zone* 12
Lavrinovicha L., Dirba J., Dobriyan R. *Design of low-torque-ripple synchronous reluctance motor with external rotor* 23
Fedotov A., Fedotov E., Bahteev K. *Application of local Fourier transform to mathematical simulation of synchronous machines with valve excitation systems* 31

SOLID STATE PHYSICS

Krasovska M., Gerbreders V., Tamanis E., Gerbreders S., Bulanovs A. *The study of adsorption process of Pb ions using well-aligned arrays of ZnO nanotubes as a sorbent* 41

PHYSICS

Krupenin V., Viba J. *The analysis of non-Newtonian vibro-impact processes in tube constructions and systems with parallel impact pairs* 51
Kanders U., Kanders K. *Nanoindentation response analysis of thin film substrates-1. Strain gradient-divergence approach* 66

Индивид. заказ. Є 1,50 Индекс 2091
Орг. заказ. Є 15,00 Индекс 2092

СОДЕРЖАНИЕ

ФИЗИКО-ТЕХНИЧЕСКИЕ ПРОБЛЕМЫ ЭНЕРГЕТИКИ

Кудрявцев О., Калласте А., Вайтман Т., Орлова С. *Исследование воздействия изменчивости постоянного магнита на эксплуатацию ветрового генератора* 3
Серебряков А., Левин Н., Камолиньш Е., Милейко М. *Индукторные машины с продольно-поперечной гребенчатой зубцовой зоной* 12
Лавриновича Л., Дирба Я., Добриян Р. *Проектирование внешнего ротора синхронного реактивного двигателя с пониженными пульсациями крутящего момента* 23
Федотов А., Федотов Е., Бахтеев К. *Применение локального преобразования Фурье для математического моделирования синхронных машин с системами возбуждения клапанов* 31

ФИЗИКА ТВЕРДОГО ТЕЛА

Красовска М., Гербредер В., Таманис Е., Гербредер С., Буланов А. *Исследование процесса адсорбции ионов Pb с использованием хорошо выровненных массивов нанотрубок ZnO в качестве сорбента* 41

ФИЗИКА

Крупенин В., Виба Я. *Анализ неньютоновских виброударных процессов в трубных конструкциях и системах с параллельными ударными парами* 51
Кандерс У., Кандерс К. *Анализ характеристик наноиндентирования тонкопленочной подложки-1. Метод дивергенции градиента деформации* 66

LATVIAN JOURNAL of PHYSICS and TECHNICAL SCIENCES

LATVIJAS FIZIKAS un TEHNISKO ZINĀTŅU ŽURNĀLS

ЛАТВИЙСКИЙ ФИЗИКО-ТЕХНИЧЕСКИЙ ЖУРНАЛ

Published six times a year since February 1964
Iznāk sešas reizes gadā kopš 1964. gada februāra
Выходит шесть раз в год с февраля 1964 года

1 (Vol. 54) • 2017

RĪGA

INDEKSĒTS (PUBLICĒTS) | INDEXED (PUBLISHED) IN

www.scopus.com
www.degruyter.com
EBSCO (Academic Search Complete, www.epnet.com), INSPEC (www.iee.org.com). VINITI (www.viniti.ru), Begell House Inc/ (EDC, www.edata-center.com).

Izdevējs: Fizikālās enerģētikas institūts
Reģistrācijas apliecība Nr. 0221
Redakcija: Krīvu iela 11, Rīga, LV-1006
Tel. 67551732, 67558694
e-pasts: ezerniec@edi.lv
Interneta adrese: www.fei-web.lv
Iespiests SIA “AstroPrint”

LATVIAN JOURNAL OF PHYSICS AND TECHNICAL SCIENCES
2017, N 1

DOI: 10.1515/lpts-2017-0001

PHYSICAL AND TECHNICAL ENERGY PROBLEMS

INFLUENCE OF PERMANENT MAGNET CHARACTERISTIC VARIABILITY ON THE WIND GENERATOR OPERATION

O. Kudrjavtsev[1], A. Kallaste[1, 2], A. Kilk[1], T. Vaimann[1, 2], S. Orlova[1, 3]

[1]Tallinn University of Technology, Department of Electrical Engineering
5 Ehitajate Str., 19086 Tallinn, ESTONIA
[2]Aalto University, Department of Electrical Engineering and Automation
5A Otakaari Str., 02150 Espoo, FINLAND
[3]Institute of Physical Energetics,
11 Krivu Str., LV-1006, Riga, LATVIA

The paper discusses problems concerning the influence of permanent magnet material characteristics on the low-speed permanent magnet generator losses and output characteristics. The variability of the magnet material and its effect on the output parameters of the machine has been quantified. The characteristics of six different grades of neodymium permanent magnets have been measured and compared to the supplier specification data. The simulations of the generator have been carried out using transient finite element analysis. The results show that magnet materials from different suppliers have different characteristics, which have a significant influence on the generator output parameters, such as efficiency and power factor.

Keywords: *characteristics variability, permanent magnet, synchronous generator.*

1. INTRODUCTION

There are several types of generators that can be used for small wind turbines [1]. One of them is the low-speed permanent magnet synchronous generator (PMSG), which is gaining more popularity due to its several advantages. It can be used in wind turbine without gearbox resulting in higher reliability and lower maintenance requirements. The PMSG also offers high efficiency and good power density.

There are several types of permanent magnets (PM) that can be used in generator: Alnico, SmCo, NdFeB, ferrites [2]. In this study, neodymium magnets are investigated, as they offer relatively high-energy product and have high coercivity.

The SPMG electrical output parameters are strongly influenced by the PM

characteristics. The variability in PM characteristics can be the result of different aspects, such as wrong usage, demagnetization, wrong manufacturing process, wrong assembly process, etc. In this study, the PM remanence and coercivity variation influence on the generator output parameters are investigated. The investigation is based on the finite element analysis.

The literature that concerns the analysis of fault detection in PM machines is mostly focused on the problems related to demagnetisation [2]–[5]. No importance has been given to variability in the PM characteristics and their effect on the output quantities of the machine.

2. GENERATOR CHARACTERISTICS

For this study, a 5 kVA outer rotor PMSG is designed with surface magnets (Fig. 1). The surface magnet design has been chosen because of the simplified assembly process. The main parameters of the machine are given in Table 1. The generator has 32 poles with grade N42H magnets with the dimensions of 30x10x100 mm.

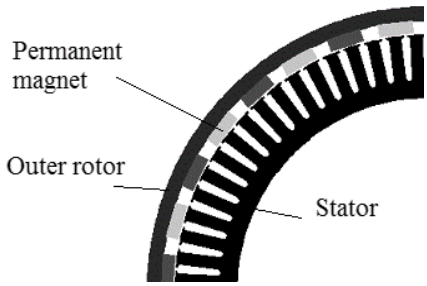

Fig. 1. Cross-section of the designed PM generator with an outer rotor.

Table 1

Generator Parameters

Parameter	Value	Unit
Rated power	5	kVA
Rotational speed	200	rpm
Electromotive force	255	V
Core length	100	mm
Air gap diameter	448.8	mm
Current density	2.56	A/mm^2
Efficiency	89.2	%
Number of pole pairs	16	-

3. MEASUREMENT PROCESS AND RESULTS

To study the PM influence on the generator output variables, six different grades of neodymium magnets were selected. For the first five grades three different suppliers of magnets were selected and for the sixth grade two suppliers of magnets

were selected. Selected magnets were measured with Vibrating Sample Magnetometer (VSM), where the PM hysteresis loop was recorded. Results of the measured magnets are given in Fig. 2 and Fig. 3.

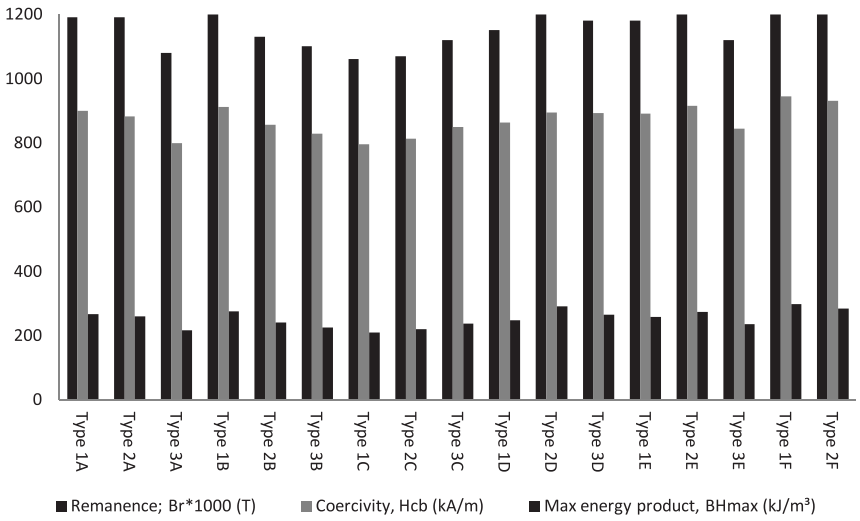

Fig. 2. Comparison graph of permanent magnet characteristics by different suppliers . Type 1A means A grade magnet from the first supplier, type 2A means A grade magnet from the second supplier. The left column indicates the remanence value, middle – the coercivity value and right – the max power product value.

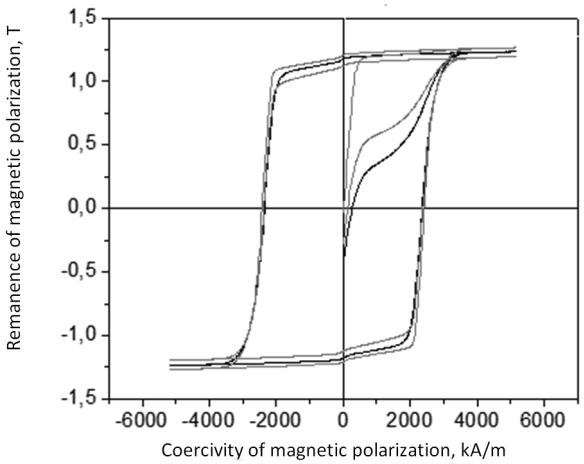

Fig. 3. The curve demonstrates an example of the measuring results made by VSM software for one grade of magnet (Grade A). Different magnet suppliers of the same magnet grade are shown using different hysteresis loops.

For comparison, magnet deviation from its rated value was found. Figure 4 gives the maximum and minimum deviation values of remanence, coercivity and maximum energy product compared to the rated value. The variation of remanence and that of coercivity are approximately 10 %; the maximum variation of maximum energy product is 22.96 %.

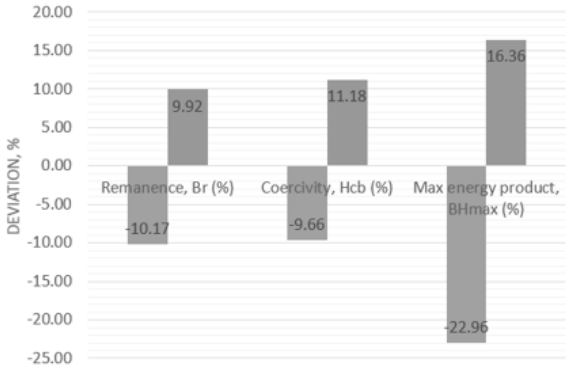

Fig. 4. Measured permanent magnet parameters compared to rated values.

4. CALCULATION RESULTS

The machine is designed according to the reference values given in Table 1. To find the PM characteristic influence on the machine output characteristic, the machine design is kept constant and the magnet remanence and coercivity are changed in ±10 % range from the nominal value. The calculations are carried out so that the machine torque and the output voltage are at the rated value. The calculation has been performed using in-house 2D FEM software.

Performing the calculation, the variation of generator losses was found (Fig. 5). It can be seen that the iron losses have almost a linear response to the magnetic characteristic change and a small nonlinearity comes due to the minor saturation of the core. The copper losses increase when the remanence has a different value from the rated one because of the increase of reactive current in the stator winding.

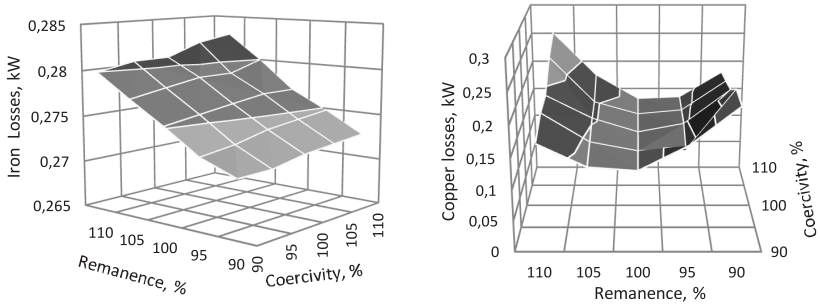

Fig. 5. Calculated variation of iron losses (left) and copper losses (right) as a function of the percentage variation of the remanence and coercivity of the permanent magnet at the rated torque operation of the generator.

The variation of the efficiency and power factor is given in Fig. 6. It can be seen that the efficiency and the power factor decrease when remanence is shifted from the rated value. The reason for such a drop is that the efficiency and power factor are optimal, when remanence is equal to the rated value (100 %).

The reason of the power factor variation is the air gap flux density variation, which is influenced by the remanence of the magnet, and influences the machine

electromotive force (EMF). When remanence is smaller than the rated value, the production of EMF will also be smaller. Similarly, when remanence is larger than the rated value, the production of EMF will be greater. The efficiency and the copper losses both depend on the power factor. For that reason, the power factor and the efficiency curves have similar shapes and the copper loss opposite shape.

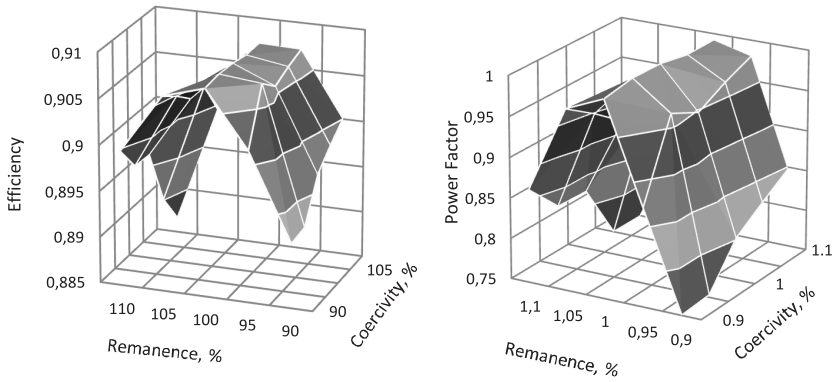

Fig. 6. Calculated variation of efficiency (left) and power factor (right) as a function of the percentage variation of the remanence and coercivity of the permanent magnet at the rated torque operation of the generator.

5. PERMANENT MAGNET DEMAGNETIZATION

One of the most critical parts of the PM generator is permanent magnets. Considering the needs of this PMSG with an outer rotor, the NdFeB magnets were designed to be used in this machine. The permanent magnet parameters are highly dependent on the temperature. The magnet type N42H was chosen to have high operational maximum temperature of 180°C.

The maximum load of the generator corresponds to the short-circuit conditions. Due to the armature reaction influence and significant decrease of flux density in the magnets during the short-circuit situation, the risk of demagnetization occurs.

The working point of the magnet is defined by the length of the magnetic path, which should be passed by the magnetic flux, and eventually the value of the current producing opposing flux. In other words, it is defined by the construction of the generator and the armature reaction magnetic flux density that emerges when the generator is loaded. The work or load point of the magnet can be found using Ampere's law:

$$\int Hdl = nI,$$

where H describes the magnetic field strength, l – the length of the magnetic path, I is the current and n – a number of turns.

As the current is missing in no-load operation, we have to specify magnetic field strength in the magnet, which is non-zero and opposite to the magnetic field strength along the rest of the magnetic path [6].

Partial demagnetization of permanent magnet means that the demagnetization curve drops comparing to its original position.

The fact that the demagnetization curve depends on the temperature of the magnet should be taken into account when using the magnet either in modelling or in constructing the wind generator. Figure 7 demonstrates the test results of temperature rise of the generator. Three curves indicate the temperature of the stator winding. The temperature of the permanent magnet can be approximately estimated from the stator winding temperature. The permanent magnet temperature will be about 20 °C lower than the stator winding temperature due to better cooling conditions.

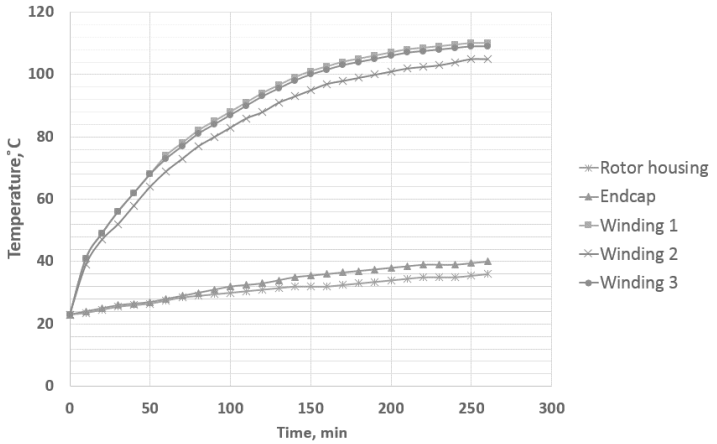

Fig. 7. Transient curves of temperature rise of the studied PM synchronous generator with an outer rotor. Temperature of winding 1 and that of winding 3 were measured in the slot centre. The temperature of winding 2 was measured in the end-winding part.

The simulation of short-circuit condition was performed for the generator with different magnet characteristics. The variation in permanent magnet characteristics was considered according to measurements made in Section 3. The remanence and coercivity varied withn the range of 90 %–110 % of the rated value. Figure 8 shows the calculated demagnetization curves for remanence and coercivity equal to 90 % of the rated values. The minimum remanence during the short-circuit is 0.24 T; therefore, demagnetization is not present.

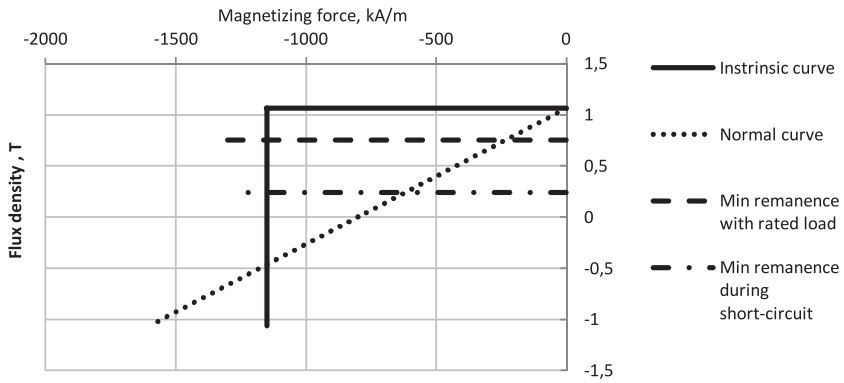

Fig. 8. Operating parameters of N42H grade magnet when remanence and coercivity are reduced by 10 % of the rated value.

Figure 9 shows the calculated demagnetization curves for remanence and coercivity equal to 100 % of the rated values. The minimum remanence during the short-circuit is 0.52 T; therefore, demagnetization is not present.

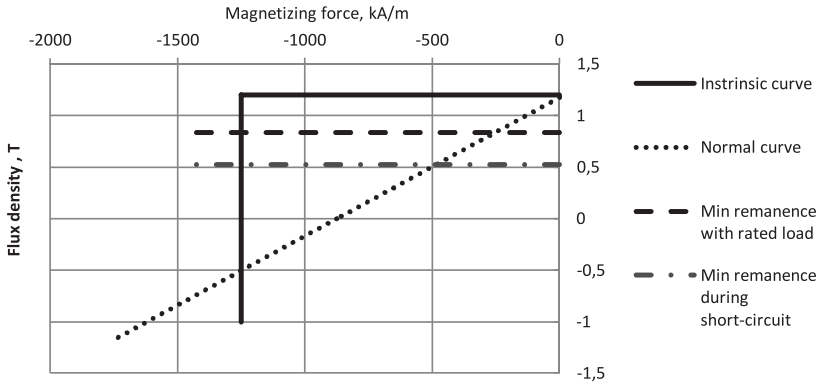

Fig. 9. Operating parameters of N42H grade magnet when remanence and coercivity are equal to the rated values.

Figure 10 shows the calculated demagnetization curves for remanence and coercivity equal to 110 % of the rated values. The minimum remanence during the short-circuit is 0.56 T; therefore, demagnetization is not present.

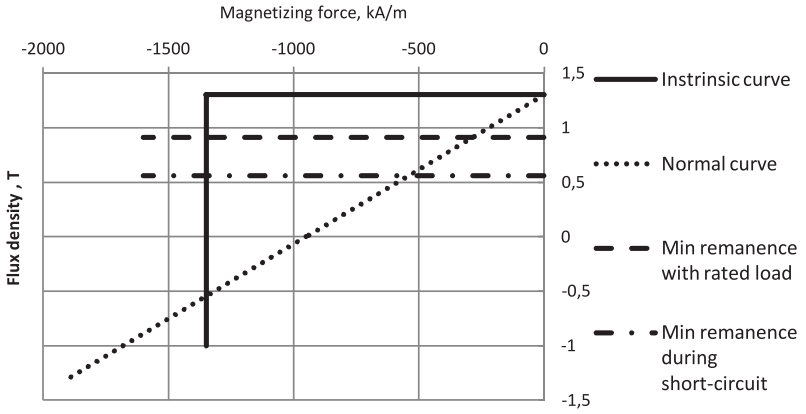

Fig. 10. Operating parameters of N42H grade magnet when remanence and coercivity are increased by 10 % of the rated value.

When remanence and coercivity are relatively high, the minimum flux density is getting higher, reducing the risk of demagnetization of permanent magnet.

The calculation for the studied PMSG with an outer rotor has shown that the armature reaction is not too strong to demagnetize the magnets and the lowest flux density in the magnet during the short circuit is about 0.7 T at 100 °C and at rated values of remanence and coercivity.

To reduce the risk of demagnetization, the proper design of rotor should be considered. The location of magnets should be chosen in the coolest region of the

machine. In the conditions of PMSG with an outer rotor, the magnets are relatively well cooled by the flow of air through the ribs on the outer surface of the rotor.

6. CONCLUSIONS

In the present research, the effect of PM characteristic variation on the generator output characteristic has been studied. For this purpose, various PM materials have been measured. The measuring results have shown a significant variation in magnet characteristics.

This PM variation has been taken into account during the generator calculations and its influence on the machine losses and efficiency has been quantified. The presented calculations have demonstrated a significant influence of the permanent magnet remanence on the machine power factor. As the power factor changes, it also strongly affects the machine efficiency and copper losses.

The influence of permanent magnet characteristic variation on demagnetization has been investigated. The demagnetization curves have been calculated and analysed for remanence and coercivity variation of 90 %–110 %. The results have shown that demagnetization does not appear in all cases. The calculations have demonstrated that the risk of demagnetization is getting higher when remanence and coercivity decrease compared to the rated value.

ACKNOWLEDGEMENTS

The present research has partially been supported by the Estonian Research Council under Grants PUTJD134 and PUT1260.

REFERENCES

1. Kudrjavtsev, O., & Kilk, A. (2012). Study and verification of a slow speed PM generator with outer rotor for small scale wind turbines. In *Proceedings of Electric Power Quality and Supply Reliability Conference (PQ)*, 11–13 June 2012 (pp. 1–6). Tartu, Estonia: IEEE.
2. Kallaste, A., Belahcen, A., & Vaimann, T. (2015). Effect of PM parameters variability on the operation quantities of a wind generator. In *Proceedings of IEEE Workshop on Electrical Machines Design, Control and Diagnosis (WEMDCD)*, 26–27 March 2015 (pp. 242–247). IEEE.
3. Ruoho, S., Dlala, E., & Arkkio, A. (2007). Comparison of demagnetization models for finite-element analysis of permanent-magnet synchronous machines. *IEEE Trans. Magn*., *43*(11), 3964–3968.
4. Ruoho, S., McFarland, J.D., & Jahns, T.M. (2004). Investigation of the rotor demagnetization characteristics of interior PM synchronous machines during fault conditions. *IEEE Trans. Ind. App., 50*(4), 2768–2775.
5. Ebrahimi, B.M., & Faiz, J. (2013). Demagnetization fault diagnosis in surface mounted permanent magnet synchronous motors. *IEEE Trans. Magn.*, *49*(3), 1185–1192.
6. Kallaste, A. (2013). *Low speed permanent magnet slotless generator development and implementation for windmills.* PhD dissertation, Tallinn University of Technology, Estonia.

PASTĀVĪGO MAGNĒTU MATERIĀLA MAINĪGUMA IETEKME UZ VĒJA ĢENERATORA DARBĪBU

O. Kudrjavtsev, A. Kallaste, A. Kilk, T. Vaimann, S. Orlova

K o p s a v i l k u m s

Rakstā tika apskatīta pastāvīgā magnēta materiāla ietekme uz lēngaitas ģeneratora ar pastāvīgajiem magnētiem zudumiem un izejošām raksturlīknēm. Tika noteikts magnēta materiāla mainīgums un tā efekts uz elektriskās mašīnas izejas parametriem. Sešas dažādas neodīmu magnētu pakāpes tika izmērītas un salīdzinātas ar piegādātāja specifikācijas datiem. Rezultāti paradīja, ka magnēta materiālam no dažādiem piegādātājiem ir dažādi raksturlielumi, kas ievērojami ietekmē ģeneratora izejas parametrus, tādus kā lietderības koeficientu un īpatnējo jaudu.

06.01.2017.

LATVIAN JOURNAL OF PHYSICS AND TECHNICAL SCIENCES
2017, N 1

DOI: 10.1515/lpts-2017-0002

INDUCTOR MACHINES WITH LONGITUDINALLY-TRANSVERSAL COMB-WISE TOOTH ZONE

A. Serebryakov[1], N. Levin[2], E. Kamolins[1], M. Mileiko[1]

[1]Riga Technical University
Faculty of Power and Electrical Engineering
12/1 Azenes Str., Riga, LV-1048, LATVIA
[2]Institute of Physical Energetics,
11 Krivu Str., LV-1006, Riga, LATVIA
e-mail: edmunds.kamolins@rtu.lv

The method considered in the present paper concerns the operational efficiency of the inductor electric machine, which can be improved by placing on the stator and rotor teeth the combs combined from differently shaped teeth and slots. The use on the inductor electric machine stator and rotor teeth of combs as a combination of differently shaped hills (teeth) and valleys (slots) allows raising the specific power of the machine. This effect is determined by the chosen type of a comb element as well as by technological possibilities of the manufacturer. The proposed method could be used moderately in the inductor machines with longitudinally-transversal combing.

Keywords: *comb teeth, inductor machines, magnetic permeance*.

1. INTRODUCTION

In the inductor electric machine (IEM), the magnetic flow produced by the excitation system (i.e., by a winding or a permanent magnet) is branched into the flows over the stator teeth. When the tooth-like rotor runs, these flows change depending on the relative position of the stator and rotor teeth. When a rotor tooth is located against a stator tooth, the permeance of the air gap between the teeth as well as the tooth flow, (Λ_{max}) and (Φ_{max}), respectively, are maximal. Change in the flow from Φ_{max} to Φ_{min} (the flow pulsation) causes the corresponding changes in the magnetic-flux linkage of the armature winding and EMF inducing there.

The IEM operational efficiency is determined by the difference $\Delta\Phi = \Phi_{max} - \Phi_{min}$ (or, respectively, $\Delta\Lambda = \Lambda_{max} - \Lambda_{min}$); therefore, the measures taken for increasing $\Phi_{max}(\Lambda_{max})$ and decreasing $\Phi_{min}(\Lambda_{min})$ favour the improvement of its technical indices.

One of the measures directed towards the improvement of IEM operation is

the use of stator and rotor teeth with specific combs, the nature and effectiveness of which are considered below.

2. THE SHAPES OF COMBS OF STATOR AND ROTOR TEETH

The comb of a stator (rotor) tooth is a combination of hills (teeth) and valleys (slots) of definite shape (Fig. 1).

The shape (profile) of the hills-teeth and valleys-slots in a comb might be rectangular (Fig. 1a), triangular (Fig. 1b), etc.

The air gap between the stator and rotor teeth can be presented:

a. for combs according to Fig. 1a – a combination of flat air gaps arranged at an angle and in parallel to the longitudinal axis of the machine;
b. for combs according to Fig. 1b – a combination of flat air gaps arranged at an angle to the longitudinal axis of the machine;

The comb-wise zone of the machine can be presented as individual elements shown in Fig. 1 for the corresponding profiles of the teeth and slots of the stator and rotor tooth combs. Combined arrangement of these elements on the stator and rotor tooth surface along the axial length of these teeth sets up their comb-wise zone.

The geometrical characteristics of the comb elements are as follows:

- $b_{zr}(b_{zs})$ is the width of the root of a rotor (stator) tooth;
- $b_{pr}(b_{ps})$ is the width of the base of a rotor (stator) slot;
- $h_{zr}(h_{zs})$ is the height of the root of a rotor (stator) tooth;
- $h_{pr}(h_{ps})$ is the height of a rotor (stator) slot;
- l_a, l_b is the axial length of a comb element according to Fig. 1a, b, respectively, which is also the length of the element air gap without a comb;
- l'_a, l'_b is the length of the comb element air gap according to Fig. 1, a, b, respectively;
- $k_a = l'_a / l_a; k_b = l'_b / l_b$ are the coefficients of air gap extension;
- δ is the rated air gap of the machine.

Within the framework of the research, geometrical parameters of the tooth zone were set as applied to a low-speed IEM: the diameter of stator bore $D_s \approx 2$ m, the number of rotor teeth $Z_R \geq 200$, the axial length of the stator and rotor cores $L = 200 \div 220$ mm.

Taking into account recommendations [1]–[3], the following geometrical parameters of the tooth zone of such a machine were chosen:

- the rated air gap $\delta = D_s / 400 = 5$ mm;
- the width of stator (rotor) teeth $b_{zs} = b_{zr} = 20$ mm;
- the height of the rotor tooth $h_{ZR} = 30$ mm (i.e., $h_{ZR} = 6\delta$);
- the height of the stator tooth $h_{zs} = 40$ mm.

The listed parameters are shown in Fig. 1 [4]–[6].

The geometrical parameters of the comb elements of the types under consideration are given in Table 1.

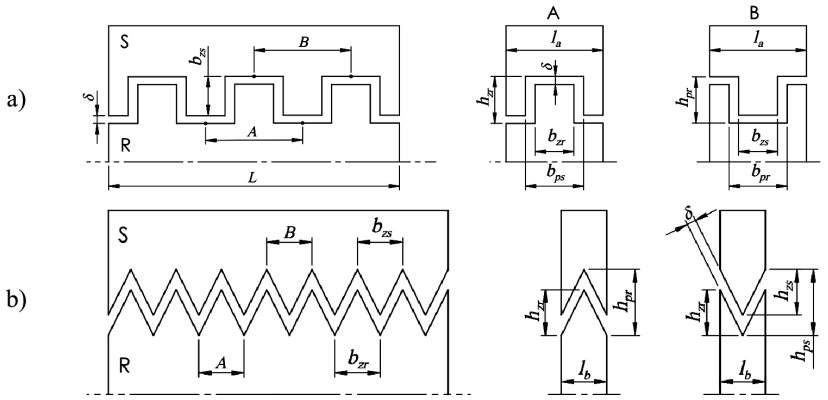

Fig. 1. Rectangular (a), triangular (b), and their elements of A and B types.

Table 1

Geometrical Parameters of Comb Elements

Type of element / Parameter (mm)	R Fig. 1a	T Fig. 1b
$b_{zr}(b_{zs})$	20	20
$b_{pr}(b_{ps})$	30	20
$h_{zr}(h_{zs})$	20	20
$h_{pr}(h_{ps})$	25	25
δ	5	5
$l_{a,b}$	50	20
$l'_{a,b}$	90	40
$K_l = l'/l$	1.8	2

3. THEORETICAL FOUNDATIONS

The permeance of a flat air gap (“protrusion” is not taken into account) is calculated as that between parallel rectangular surfaces facing one another (Fig. 2) according to the formula [4]–[6]:

$$\Lambda = \frac{S\mu_0}{\delta} = \frac{ab\mu_0}{\delta}, \tag{1}$$

where S, a, b, δ are the air gap area, width, length, and height (thickness), respectively; $\mu_0 = 4\pi \cdot 10^{-7}$ H/m is the magnetic constant.

In the analysis of permeance variation for a tooth zone of the IEM with a rectangular flat air gap and with a comb (i.e., with a curvilinear air gap) the *a* and *b* values are invariable (while different for different types of comb). Therefore, the product $ab\mu_0$ can be taken as a conditional unit; then the permeance expressed in conditional permeance units (CPU) will be inversely proportional to the air gap value, i.e.,

$$\Lambda = \frac{1}{\delta}, \text{ CPU.} \tag{2}$$

We assume that the base CPU is the permeance corresponding to the calculated data of a tooth zone without a comb (Λ_B).

To compare the combs as to their permeance values, these are to be reduced to the base permeance, dividing the real permeance (Λ (2)) by the base one (Λ_B).

The magnetic flux across the air layer expressed in conditional units for magnetic flux (CUMF) will be defined as

$$\Phi = \Lambda F = \frac{F}{\delta}, \text{ CUMF,} \tag{3}$$

where F is the MMF of excitation.

It is necessary to express the Λ and Φ values in conditional units for comparative estimation of the effectiveness of using differently shaped tooth combs.

The permeance of the ring-wise air gap (Fig. 3) is determined as [4]–[6]

$$\Lambda = \frac{\mu_0 b \Theta}{\ln\left(1 + \frac{\delta}{r}\right)}, \tag{4}$$

(for parameters b, Θ, δ, r see Fig. 3).

4. INFLUENCE OF COMB ON THE MAXIMUM PERMEANCE OF THE AIR GAP UNDER A STATOR TOOTH

At the position of rotor tooth 1 against stator tooth 2 (at b_{zs} and b_{zr} being equal, Fig. 4), the permeance of the air gap between them is maximal $(\Lambda_{\max})$, and the corresponding magnetic flux – flow per unit is also maximal $(\Phi_{\max})$.

Such being the case, the magnetic flow through the tooth zone can be presented as separate flows through characteristic sections of the air gap:

- flow Φ_z in the path “stator tooth – rated air gap – rotor tooth”;
- flow Φ_p in the path “stator slot – rotor slot” (leakage flux).

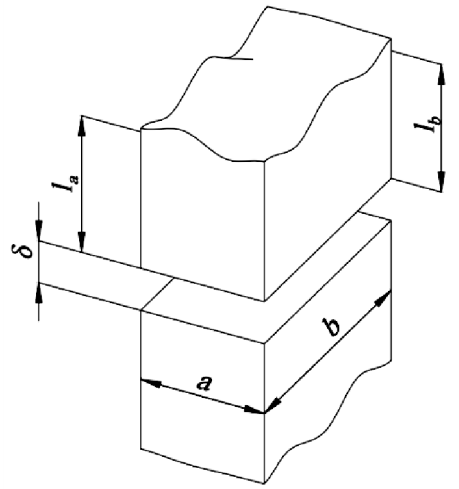

Fig. 2. Parallel rectangular surfaces facing one another.

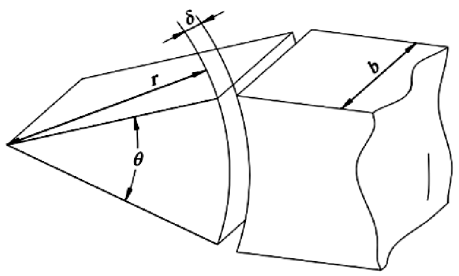

Fig. 3. Parameters of b, Θ, δ, r.

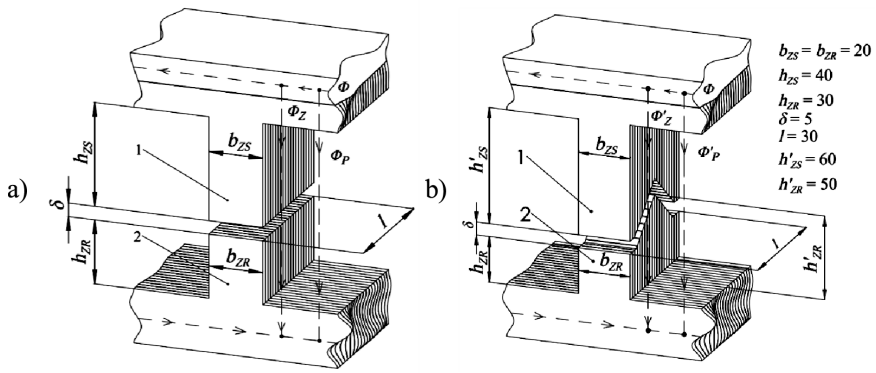

Fig. 4. Arrangement of stator teeth 1 and rotor teeth 2 corresponding to the maximum permeance of rectangular (a) and curvilinear (b) air gaps.

In compliance with the assumed designations for tooth zone parameters, expressions (1) and (4) are transformed, respectively, to the following ones:

$$\Lambda = \frac{b_{zs} l \mu_0}{\delta}. \tag{5}$$

Using teeth with differently shaped combs, the picture of flows passing through teeth and slots (Φ'_z and Φ'_p, respectively, Fig. 4) remains basically invariable, while their number will change. The relevant numerical values are given in Table 2.

As the first theoretical estimate for the extent of increase in the maximum permeance of the tooth zone with combs (and in the maximum flux, accordingly) we could take the air gap extension coefficient $K_{l(a,b)}$ (Table 1). All the more so because such an estimate seems to be valid since this increase occurs owing to that in the air gap length, whereas the calculated values of the efficiency coefficients $K_{(a,b)}$ and $K_{E(a,b)}$ given in Table 2 coincide with the corresponding values of coefficients $K_{l(a,b)}$.

However, using one or another shape of comb some peculiarities arise, which resist the theoretical analysis. Since the comb zone sections are arranged at an angle to the rectangular air gap of a comb-free machine, taking also into account the saturation of stator and rotor cores, the effectiveness of air gap extension decreases.

Therefore, in a comb zone with rectangular teeth and slots the magnetic flows through the side walls (taking into account the saturation of stator and rotor cores) are much weaker than the flows through the bases of teeth and slots of the comb. Assuming these flows to be approximately $10 \div 15$ % of the flows through bases a forecasted efficiency coefficient can be set for the extent of $\Lambda_{\max}$ and $\Phi_{\max}$ increasing:

$$K^o_{Ea} = (0.6 \div 0.65) K_{Ea}.$$

The values of this coefficient are given in Table 2. Using for the tooth and slot walls the steel sheets of $3 \div 5$ times greater thickness with respect to other saturating sheets ($0.5 \div 1$ mm), we can derive the efficiency coefficient for the maximum flow as

$$K^o_{Ea} = (0.63 \div 0.67) K_{Ea}.$$

The greatest increase in the air gap length is in the comb zone with triangular teeth and slots $(K_b = 2)$. However, due to the angular arrangement of flat air gaps and saturation, the air gap size in the zones of triangle vertices (i.e., of teeth and slots) increases two times, while the flow correspondingly decreases. The extent of increase in $\Phi_{\max}$ depending on the slope of tooth and slot walls with respect to their bases can be approximately estimated as follows:

$$K^o_{Eb} = (0.6 \div 0.65) K_{Eb},$$

for K^o_{Eb} values see Table 2.

The slot permeances and the corresponding flows through the slots (see Table 2) do not practically affect the $\Lambda_{\max}$ and $\Phi_{\max}$ values.

Table 2

Values Calculated for Rectangular and Triangular Combs

Comb type / Calculated value	Rectangular Fig. 1a			Triangular Fig. 1b		
	Designation	Formula	$A \cdot \mu_0$ H	Designation	Formula	$B \cdot \mu_0$ H
Maximum permeance of a stator element without a comb (basic)	Λ_{sa}	$\frac{b_{zs} l_a \mu_0}{\delta}$	0.20	Λ_{sb}	$\frac{b_{zs} l_b \mu_0}{\delta}$	0.08
Maximum permeance of a stator element with a comb	Λ_{za}	$\frac{b_{zs} l'_a \mu_0}{\delta}$	0.36	Λ_{zb}	$\frac{b_{zs} l'_b \mu_0}{\delta}$	0.16
Theoretical coefficient of the comb element efficiency	K_a	$\Lambda_{za} / \Lambda_{sa}$	1.8	K_b	$\Lambda_{zb} / \Lambda_{sb}$	2.0
Number of comb elements on the core length of 200 mm	ν_a	L / l_a	4	ν_b	L / l_b	10
Maximum permeance of stator core without a comb (basic)	$\Lambda^a_{\max}$	$\Lambda_{sa} \nu_a$	0.8	$\Lambda^b_{\max}$	$\Lambda_{sb} \nu_b$	0.8
Maximum permeance of stator core with combs	$\Lambda^{La}_{\max}$	$\Lambda_{za} \nu_a$	1.44	$\Lambda^{Lb}_{\max}$	$\Lambda_{zb} \nu_b$	1.6
Theoretical coefficient of comb efficiency with respect to $\Lambda_{\max}$ $(\Phi_{\max})$	K_{Ea}	$\Lambda^{La}_{\max} / \Lambda^a_{\max}$	1.8	K_{Eb}	$\Lambda^{Lb}_{\max} / \Lambda^b_{\max}$	2.0
Slot permeance of a tooth zone without a comb (basic)	Λ_{pa}	$\frac{b_{ps} l_a \mu_0}{h_{zs} + \delta + h_{ZR}}$	0.02	Λ_{pb}	$\frac{b_{ps} l_b \mu_0}{h_{zs} + \delta + h_{ZR}}$	0.008
Slot permeance of a tooth zone with a comb	Λ'_{pa}	$\frac{b_{ps} l'_a \mu_0}{h'_{zs} + \delta + h_{ZR}}$	0.026	Λ'_{pb}	$\frac{b_{ps} l'_b \mu_0}{h'_{zs} + \delta + h_{ZR}}$	0.01
Coefficient of slot permeance variation	K_{pa}	$\frac{\Lambda'_{pa} - \Lambda_{pa}}{\Lambda'_{pa}}$	0.23	K_{pb}	$\frac{\Lambda'_{pb} - \Lambda_{pb}}{\Lambda'_{pb}}$	0.2
Coefficient of the influence of slot permeance on $\Lambda_{\max}$ of the core	K_{ma}	$\Lambda'_{pa} \nu_a / \Lambda^{La}_{\max}$	0.07	K_{mb}	$\Lambda'_{pb} \nu_b / \Lambda^{Lb}_{\max}$	0.06
Forecasted coefficient of comb efficiency with respect to $\Lambda_{\max}$ $(\Phi_{\max})$	K^o_{Ea}	$(0.6 \div 0.63) K_{Ea}$	1.1÷1.15	K^o_{Eb}	$(0.6 \div 0.65) K_{Eb}$	1.2÷1.3

Note: A, B are the numerical values of physical quantities.

The maximum permeance of the air gap of stator core without a comb $\Lambda_{\max} = \frac{b_{zs} L \mu_0}{\delta} = 0.8 \mu_0, H.$

5. COMB INFLUENCE ON THE MINIMUM PERMEANCE OF THE AIR GAP UNDER A STATOR TOOTH

At arrangement of rotor tooth 1 between stator teeth 2 (i.e., against a stator slot, see Fig. 5), the permeance of the air gap between stator and rotor is minimal $(\Lambda_{\min})$; correspondingly, the magnetic flux is also minimal $(\Phi_{\min})$. The latter can be presented as flows/fluxes through characteristic sections of the air gap:

- the flow over the central part of a stator tooth (Φ_{czs}) passing through the section of the air gap, with maximum of $\delta_{\max} = \delta + h_{ZR}$ (δ is the nominal/rated gap; h_{ZR} is the height of the rotor tooth);
- the flow over the side parts of stator and rotor teeth Φ_{bz} passing through the air gap sections with the nominal/rated gap δ;
- the flow over the central part of a rotor tooth (Φ_{czs}) passing through stator slot 3 and the air gap section with gap δ, i.e., through the summary air gap $\delta_{\Sigma} = \delta + h_{zs}$ (h_{zs} is the height of the stator tooth), being therefore a leakage flux.

The minimal flow of stator tooth can be presented in the form:

$$\Phi_{\min} = \Phi_{czs} + \Phi_{bz}\,. \tag{6}$$

When we use in the machine the stator and rotor teeth with a longitudinal comb, the picture of flow passage corresponding to $\Phi_{\min}$ would not basically change (Fig. 6). However, the number of flows according to (6) will change, which is connected with changes in the geometrical sizes of some sections on the way of flow passage, and, accordingly, in their permeance (with stator teeth b_{zs} and rotor teeth b_{ZR} being invariable).

Two basic variants arise as to the arrangement of stator and rotor teeth with combs:

- at the arrangement of a comb in stator slot 3` of comb slot 4`, which applies to the cross-section passing through the axes of comb slots and teeth (see Fig. 6, a);
- at the arrangement in stator slot 3` of comb tooth 5` (Fig. 6b).

In the process of calculation of permeances and flows taking into account the air gap values on the ways of passage of central Φ_{czs} and lateral Φ_{bz} stator tooth flows, it is assumed that the stator tooth width for passage of these flows (Φ_{czs} and Φ_{bz}) is $0.5b_{zs}$ and $0.25b_{zs}$, respectively. This is reflected in the calculation formulas shown in Table 3 along with the calculation results.

Related permeances (we will call them “slot-slot” type) and second ones (“slot-tooth” type) are shown in Fig. 6a and b respectively, where those are arranged at the core half-length each, taking into account the air gap extension.

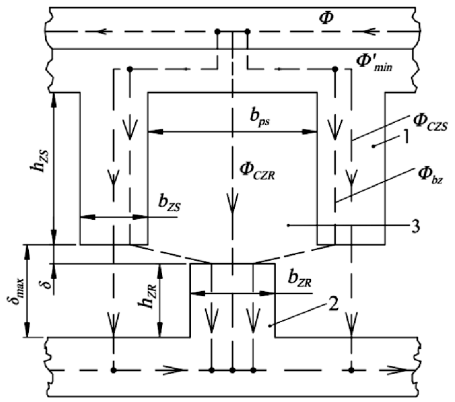

Fig. 5. Arrangement of stator teeth 1 and rotor teeth 2 corresponding to the minimal permeance of a rectangular air gap.

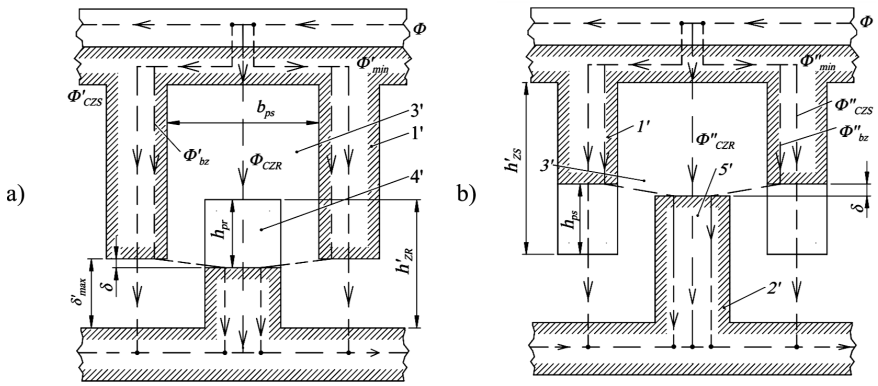

Fig. 6. Arrangement of stator teeth 1 and rotor teeth 2 with combs corresponding to the minimal permeance of a curvilinear air gap at
a) placement in stator slot 3` of comb slot 4`;
b) placement in stator slot 3` of comb tooth 5`; sizes (mm):
$\delta'_{\max} = 20$; $h'_{zs} = 60$; $h'_{zr} = 50$; $h_{ps} = 25$; $h_{pr} = 25$.

The summarised influence of combs favours the increase in permeance and flow pulsations $\Delta\Lambda = \Lambda_{\max} - \Lambda_{\min}$ and, consequently, the increase in induced EMF and power of the machine as well as in the specific power, since the effect of increase in the weight of stator and rotor cores due to the use of combs is significantly weaker as compared with that of increased power.

The theoretical value of permeance pulsation coefficient $K_{\Lambda} = \frac{\Delta\Lambda_{a,b}}{\Delta\Lambda}$ for all considered types of comb in reality coincides with that for air gap extension coefficient K_l (Table 1). This allows for the choice of forecasted coefficients of comb efficiency $K^{\Pi}_{E\Lambda}$ (Table 3) that would be equal to the corresponding comb efficiency coefficients $K^{o}_{E(a,b)}$ (Table 2) as related to the maximal flow.

To verify the statements mentioned above, the mathematical modelling has been performed for the elements of comb-wise tooth zones, which confirms, in principle, that it is possible to employ the effect of combs but with slightly smaller (by $10 \div 15\%$) values of real efficiency coefficients $K^{r}_{E(a,b)}$ given in Table 3.

It is quite natural that the designer should employ the effect from the use of combs taking into account the production expenses.

Table 3

Formula of Modelling

Rectangular air gap (without comb)			Type of comb / Calculated value	Rectangular Fig. 1a			Triangular Fig. 1b		
Designation	Formula	$Y \cdot \mu_0$ H		Designation	Formula	$A \cdot \mu_0$ H	Designation	Formula	$B \cdot \mu_0$ H
Λ_{cps}	$\frac{0.5 b_{ZR} L \mu_0}{2\delta(\delta + h_{ZR})}$	0.03	Permeance for Φ_{czs} of half-comb slots	Λ^a_{cp}	$\frac{0.5 b_{zs} l'_a \nu_a \mu_0}{2 h_{ZR}}$	0.06	Λ^b_{cp}	$\frac{0.5 b_{zs} l'_b \nu_b \mu_0}{2 h_{ZR}}$	0.066
Λ_{bp}	$\frac{0.25 b_{ZR} L \mu_0}{2(b_{ps} - b_{ZR})}$	0.05	Permeance for Φ_{bz} of half-comb slots	Λ^a_{bp}	$\frac{0.25 b_{zs} l'_a \nu_a \mu_0}{2(b_{ps} - b_{ZR})}$	0.09	Λ^b_{bp}	$\frac{0.25 b_{zs} l'_b \nu_b \mu_0}{2(b_{ps} - b_{ZR})}$	0.100
$\Lambda^p_{\min}$	$\Lambda_{cps} + \Lambda_{bp}$	0.08	Permeance for $\Phi_{\min}$ of half-comb slots	$\Lambda^{pa}_{\min}$	$\Lambda^a_{cp} + \Lambda^a_{bp}$	0.15	$\Lambda^{pb}_{\min}$	$\Lambda^b_{cp} + \Lambda^b_{bp}$	0.166
			Permeance for Φ_{czs} of half-comb teeth	Λ^a_{cz}	$\frac{0.5 b_{zs} l'_a \nu_a \mu_0}{2(h_{ps} + h_{ZR})}$	0.036	Λ^b_{cz}	$\frac{0.5 b_{zs} l'_b \nu_b \mu_0}{2(h_{ps} + h_{ZR})}$	0.04
			Permeance for Φ_{bz} of half-comb teeth	Λ^a_{bz}	$\frac{0.25 b_{zs} l'_a \nu_a \mu_0}{2(h_{ps} + h_{ZR})}$	0.09	Λ^b_{bz}	$\frac{0.25 b_{zs} l'_b \nu_b \mu_0}{2(h_{ps} + h_{ZR})}$	0.10
			Permeance for $\Phi_{\min}$ of half-comb teeth	$\Lambda^{za}_{\min}$	$\Lambda^a_{cz} + \Lambda^a_{bz}$	0.126	$\Lambda^{zb}_{\min}$	$\Lambda^b_{cz} + \Lambda^b_{bz}$	0.14
			The mean minimal permeance	Λ_a	$\frac{\Lambda^{pa}_{\min} + \Lambda^{za}_{\min}}{2}$	0.138	Λ_b	$\frac{\Lambda^{pb}_{\min} + \Lambda^{zb}_{\min}}{2}$	0.153
K_m	$\frac{\Lambda^p_{\min}}{\Lambda_{\max}}$	0.1	The minimum/maximum permeance core ratio of the core	K^a_m	$\Lambda_a + \Lambda^a_{\max}$	0.096	K^b_m	$\Lambda_b + \Lambda^b_{\max}$	0.096
$\Delta\Lambda$	$\frac{\Lambda_{\max}}{\Lambda^p_{\min}}$	0.72	Difference between the maximal and minimal permeances of the core	$\Delta\Lambda_a$	$\Lambda^a_{\max} - \Lambda_a$	1.302	$\Delta\Lambda_b$	$\Lambda^b_{\max} - \Lambda_b$	1.447
			Theoretical coefficient of comb efficiency (overall)	K^t_{Ea}	$\Delta\Lambda_a / \Delta\Lambda$	1.81	K^t_{Eb}	$\Delta\Lambda_b / \Delta\Lambda$	2.01
			Forecasted coefficient of comb efficiency	K^{Π}_{Ea}	–	1.1÷ 1.15	K^{Π}_{Eb}	–	1.2÷ 1.3
			Real coefficient of comb efficiency	K^r_{Ea}	Result of modelling	1.21	K^r_{Eb}	Result of modelling	1.16

From the results it follows that even though the use of combs increases to an extent $\Lambda_{\min}$ and $\Phi_{\min}$, the influence of this increase is weaker than that in a comb-free tooth zone (see K_m coefficient value).

6. CONCLUSIONS

The use on the IEM stator and rotor teeth of combs as a combination of differently shaped hills (teeth) and valleys (slots) allows raising the specific power of the machine. This effect is determined by the chosen type of a comb element as well as

by technological possibilities of the manufacturer.

At the same time, it is necessary to take into account that the use of longitudinally-transversal combing can lead to a forced decrease in the MMF excitation (to avoid possible saturation of steel), which would reduce the effect of power increase – or even exclude it.

All this should be taken into account and used moderately in the inductor machines with longitudinally-transversal combing.

ACKNOWLEDGEMENTS

The present research has been supported by the State Research Programme "LATENERGI".

REFERENCES

1. Levin, N. N., & Serebryakov, A.D. (1976). Electric machines and drives. In Proceedings of RVVKKU (Vol. 3). Riga (in Russian).
2. Santalov, A. M., & Serebryakov, A.D. (1976). On the optimal geometry of the tooth zone of inductor machines. In Proceedings of RKIIGA (Vol. 113, pp. 12–23). Riga (in Russian).
3. Serebryakov, A. D. (1982). Optimal tooth zone of the inductor motor. Contactless electric machines (Vol. 21, pp. 157–162). Riga: Zinatne (in Russian).
4. Alper, N. J. (1962). Calculation of magnetic fields in the air gap of the inductor machine with constant flow. In Bulletin of Electronic Industry, Vol. 3. Moscow (in Russian).
5. Bul, B. K. (1964). *Foundations of Theory and Calculation of the Magnetic Fields*. Moscow: Energy (in Russian).
6. Koc, B. E. (1964). Determination of air gap permeances in comb-wise magnetic systems. *Elecrotechnics*, 9. Moscow (in Russian).

INDUKTORMAŠĪNAS AR GARENISKI-TRANSVERSĀLĀM ĶEMMVEIDA ZOBU ZONĀM

A. Serebrjakovs, N. Levins, E. Kamoliņš, M. Mileiko

K o p s a v i l k u m s

Dotajā darbā piedāvātā metode attiecināma uz induktortipa elektriskās mašīnas efektivitātes paaugstināšanu, ko var realizēt, izveidojot mašīnas statora un rotora zobus ar dažāda veida gareniski-transversiālām ķemmveida zobu zonām. Izmantojot induktortipa mašīnās ķemmveida statoru un rotoru un, kombinējot tos ar dažādas formas zobiem un rievām, ir iespējams paaugstināt elektriskās mašīnas īpatnējo momentu. Šis efekts ir atkarīgs no izvēlētā ķemmveida formas elementa kā arī no ražotāja tehnoloģiskajām iespējām. Piedāvātā metode var būt saprātīgi pielietota induktortipa mašīnās ar gareniski-transversiālu ķemmveida zobu zonu.

02.12.2016.

LATVIAN JOURNAL OF PHYSICS AND TECHNICAL SCIENCES
2017, N 1

DOI: 10.1515/lpts-2017-0003

DESIGN OF LOW-TORQUE-RIPPLE SYNCHRONOUS RELUCTANCE MOTOR WITH EXTERNAL ROTOR

L. Lavrinovicha, J. Dirba, R. Dobriyan
Riga Technical University,
12/1 Azenes Str., Riga, LV-1048, LATVIA
e-mail: janis.dirba@rtu.lv

The paper presents new designs for synchronous reluctance motors that have external rotor (segment-shaped rotor, rotor with additional non-magnetic space to the quadrature axis of the rotor, and rotor with several flux barriers). Impact of the external rotor configuration on the electromagnetic torque and torque ripple is analysed. Electromagnetic torque ripple factor is calculated for each studied motor using the results of magnetic field numerical calculations.

Keywords*: external rotor motor, reluctance motor, torque ripple, torque ripple factor.*

1. INTRODUCTION

After intensive import of vector control drive, synchronous reluctance motors have received great attention as a good alternative to other types of motors, such as brushed motors or induction motors. Consequently, there is renewed interest in the design of synchronous reluctance motor in order to obtain results that are comparable with other widely used motors.

Many recent studies [1]–[6] present a variety of new designs of synchronous reluctance motors and techniques for improving the existing motor designs. Most studies are devoted to the determination and justification of the rational design of reluctance motor with high electromagnetic torque, where the goal is achieved by solving such a problem as a reduction of the magnetic flux in the quadrature axis (q-axis) and an increase in the direct axis (d-axis). For example, results obtained in paper [1] show that direct magnetic flux should be increased, but quadrature magnetic flux should be reduced. The fact that one of the ways to increase the electromagnetic torque is the simultaneous execution of synchronous reluctance motor as a two-pole motor ($2p = 2$) is also presented in paper [1].

In many cases, increasing the electromagnetic torque by increasing difference of magnetic fluxes in the direct and quadrature axes causes a problem of emergence of high torque ripple due to uneven air gap in the motor.

Papers [4]–[5] present the study of difference methods for reducing torque ripple, which in some cases does not have effective results. In order to find the

effective solution to suppress the electromagnetic torque ripple and at the same time to maintain the average value of the electromagnetic torque, it is necessary to carry out a deep analysis of the distribution of the magnetic field in the active part of the studied machine depending on the configurations of ferromagnetic and non-magnetic parts of the rotor.

The goal of the research is to show a general approach to the design of external rotor synchronous reluctance motor and reduction of electromagnetic torque ripple in such motors.

2. ANALYSIS OF ROTOR DESIGNS FOR SYNCHRONOUS RELUCTANCE MOTOR

Published patent [2] describes the developed designs for synchronous reluctance motor with the external rotor, where the rotor is made up of mutually magnetically isolated laminated packages of electrical steel (see Fig. 1). The rotor packages have narrow sides of segmental shape, each with its active surface directed to the stator and separated from it by an air gap. Pole coverage factor for such a motor is increased to 0.95–0.98, which increases specific electromagnetic torque in comparison with a motor with salient poles.

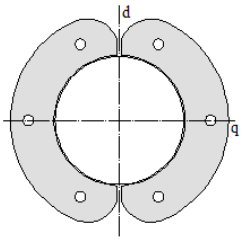

Fig. 1. A cross-section illustration of segment-shaped external rotor for a synchronous reluctance motor.

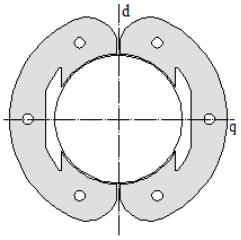

Fig. 2. A cross-section of segment-shaped external rotor with non-magnetic spaces along quadrature axis for a synchronous reluctance motor.

Results presented in paper [4] show that synchronous reluctance motor with a segment-shaped external rotor has significant electromagnetic torque ripple. In addition, the known method of torque ripple reduction – skewed rotor packages by value of the stator slot pitch in such a motor can significantly reduce torque ripple; however, in such a case the average value of electromagnetic torque greatly decreases. Furthermore, in this case, copper losses will be greater, and automatic creation of winding will be quite complicated due to longer stator winding.

In order to increase electromagnetic torque of segment-shaped synchronous reluctance motor, studies [6]–[7] propose making an additional non-magnetic space in each segment of the rotor (see Fig. 2). In this case, the non-magnetic spaces are created in the direction of quadrature axis of the motor, which reduce quadrature magnetic flux. As a result, electromagnetic torque increases. In addition, non-magnetic spacing in the rotor segments reduces weight and, thus, increases motor specific torque.

Results published in paper [7] show that torque ripple in the synchronous reluctance motor is strongly influenced by a number of stator slots and width of slot opening. According to the results obtained in paper [7], it has been concluded that after increasing the number of stator slots, torque ripple is substantially reduced, while an amplitude value of the fundamental harmonic of electromagnetic torque is slightly increased. Thus, increasing the number of stator slots from Z = 6 to Z = 18 leads to an approximately twofold decrease in the torque ripple factor and to an increase in the amplitude value of fundamental harmonic of electromagnetic torque by 5 %.

Research results for a synchronous reluctance motor with an inner rotor presented in papers [5] and [8] show that the effective difference between the direct and quadrature magnetic fluxes can be achieved using the rotor design with several non-magnetic flux barriers (see Fig. 3).

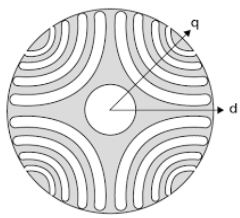

Fig. 3. A cross-sectional illustration of an inner rotor with flux barriers for a synchronous reluctance motor.

The analysis of design characteristics of the inner rotor of reluctance motor, which is presented in Fig. 3, requires studying torque ripple reduction opportunities by creating the external rotor of reluctance motor with several non-magnetic flux barriers (see Fig. 4 a). In order to increase mechanical strength, rotor flux barriers are designed with fasteners as shown in Fig. 4 b. The width of the flux barriers is equal to that of stator slot opening, and thickness of fasteners is 4 mm.

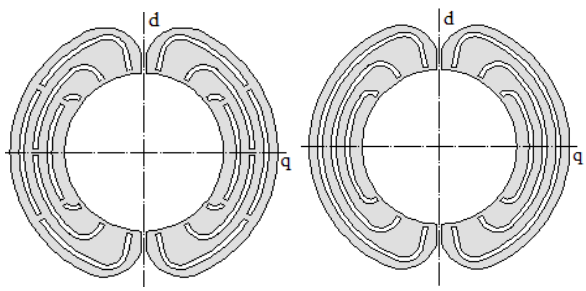

(a) *(b)*

Fig. 4. Cross-sectional illustrations of external rotor with flux barriers for a synchronous reluctance motor.

3. ELECTROMAGNETIC TORQUE AND TORQUE RIPPLE FACTOR

As it is known [9] from equation (1), electromagnetic torque of synchronous motor with an unsaturated magnetic circuit depending on the angle ε between the rotor direct axis and axis of armature magnetizing force has sinusoidal changing.

$$T_{em} = \frac{1}{2} mpL_{ad} I_1^2 \left(1 - \frac{k_q}{k_d} \right) \sin(2\varepsilon), \tag{1}$$

where m is the number of phases;

p is the number of pole pairs;

L_{ad} is the inductance corresponding to the armature magnetic flux along the direct axis;

I_1 is the armature current;

k_q/k_d is the armature reaction factors along the direct and quadrature axis ratio.

That is why it is appropriate to distribute the fundamental harmonic T_{1em} of the motor electromagnetic torque curve, which has a sinusoidal shape. In turn, torque ripple can be evaluated by comparing the calculated electromagnetic torque curve with the fundamental harmonic. For this purpose, the torque ripple factor (2) is derived:

$$k_p = \frac{\sum_{i=1}^{n} |\Delta a|}{n \cdot T_{\max 1}}, \tag{2}$$

where n is the number of evenly selected points on the half interval of the electromagnetic torque sinusoidal curve;

Δa is the difference between values of the electromagnetic torque T_{em} and the fundamental harmonic of electromagnetic torque T_{em1} in relevant points;

$T_{\max 1}$ is the maximum of electromagnetic torque fundamental harmonic.

4. SIMULATION OF MAGNETIC FIELD OF THE STUDIED MOTOR AND RESULT ANALYSIS

In order to assess the possibilities to reduce torque ripple in a synchronous reluctance motor at the same time ensuring high torque, the motor with different rotor designs is investigated with the help of magnetic field simulation by a finite element method. In this case, the electromagnetic torque of the motor is calculated using the Maxwell stress tensor method that is described in [10]. Using the Maxwell stress tensor, electromagnetic torque is described by surface integral (3) of the surface in the middle of motor air gap:

$$T_{em} = \oint_S \left(\bar{r} \times \left[\frac{1}{2\mu_0} \left(B_n^2 - B_t^2 \right) \times \bar{n} - \frac{1}{\mu_0} B_n B_t \bar{t} \right] \right) dS , \tag{3}$$

where T_{em} is the electromagnetic torque;
μ_0 is vacuum magnetic permeability;
$\bar{n}$ is the normal vector of the point on a closed surface *S*;
$\bar{r}$ is the radius-vector of the point on a closed surface *S*;
$\bar{t}$ is the tangent vector of the point on a closed surface *S*;
B_n is the normal component of the magnetic flux density;
B_t is the tangential component of the magnetic flux density.

The accuracy of the electromagnetic torque calculation by the Maxwell tensor depends essentially on the spatial position of integrating contour, degree and evenness of the mesh in the computational domain. In order to eliminate the influence of these factors on the calculation results, the contour of integration is offered to put in the so-called box, as shown in Fig. 4.

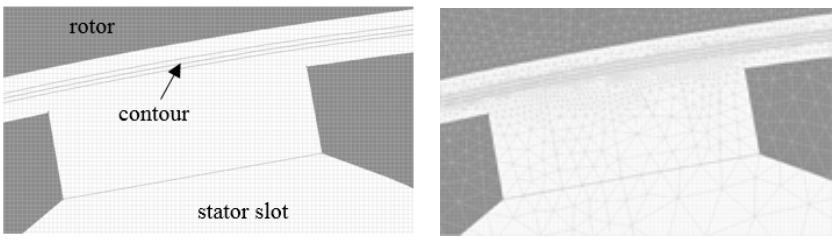

Fig. 4. Illustration of integration contour in the rotor air gap.

The following sizes of the motor under analysis are taken as constant: the outer diameter is 170 mm, the axial length of the motor active part is 100 mm, the anchor outer diameter is 100 mm and air gap is 0.5 mm. The results presented in [7] show that the effective number of stator slots for the motor with the accepted dimensions is Z = 18. Larger slot number is no desirable from the perspective of dental mechanical strength and winding creation.

Figures 5 and 6 present the magnetic flux distribution and the electromagnetic torque curves for the studied motor with different rotor designs. The calculated torque ripple factor for the studied motor with different rotor designs is presented in Table 1. Figures 5 and 6 demonstrate results for the following synchronous reluctance motor designs: (a) – the motor with a segment-shaped external rotor; (b) – the motor with a segment-shaped external rotor having non-magnetic space in quadrature axis; (c) – the motor with a segment-shaped external rotor with three non-magnetic flux barriers; (d) – the motor with a segment-shaped external rotor with three non-magnetic flux barriers and mechanical fasteners in barriers. Slot number of the stator is selected as Z = 18.

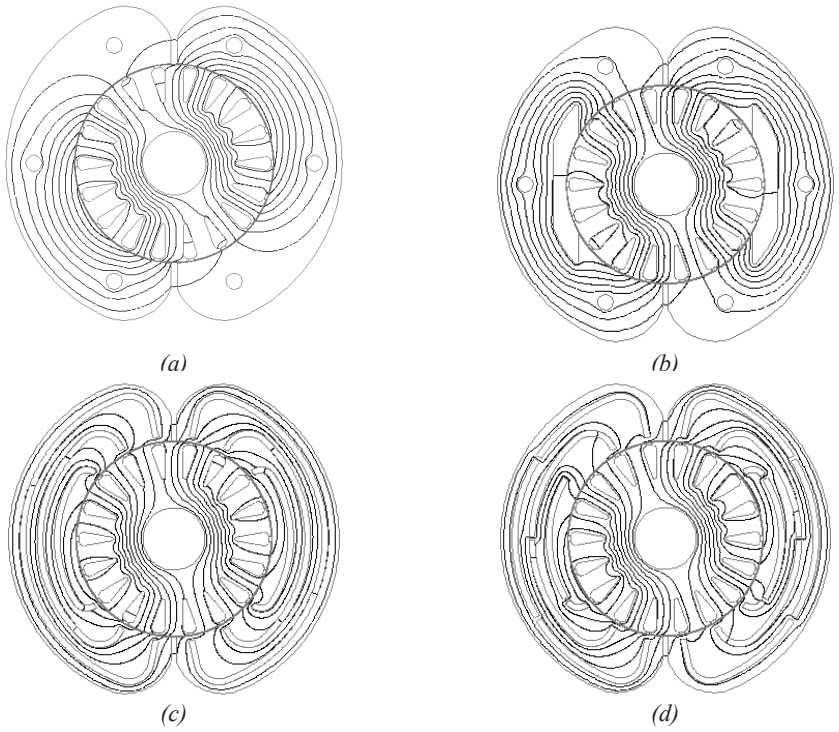

Fig. 5. Magnetic field distribution of the studied motor at ε = 30 deg.

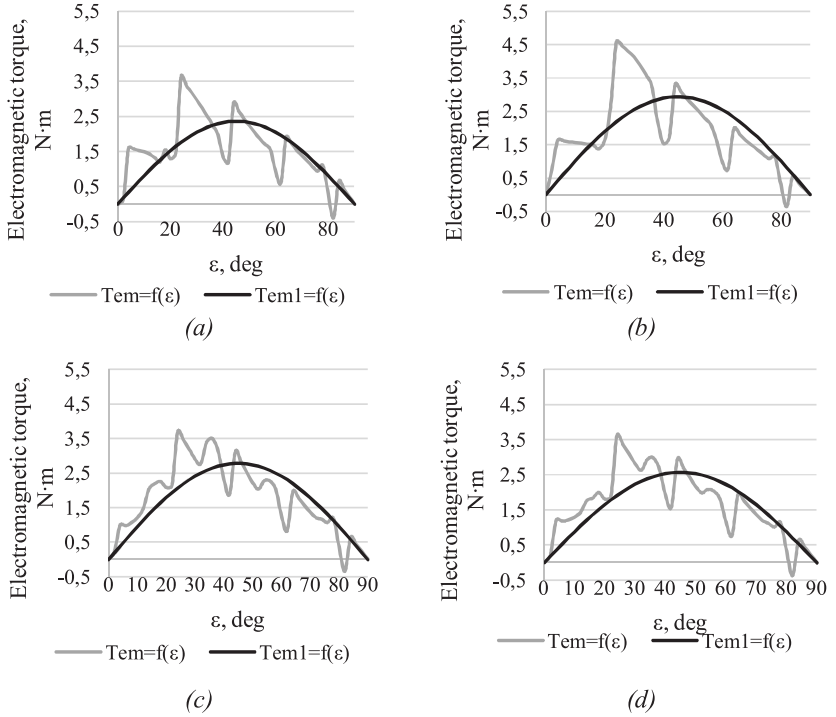

Fig. 6. Electromagnetic torque curves for the studied motor with different rotor designs.

Table 1

Calculated Results for the Studied Motor with Different Rotor Designs

	Design *(a)*	Design *(b)*	Design *(c)*	Design *(d)*
Torque ripple factor, k_p	0.204	0.227	0.174	0.177
Fundamental harmonic, T_{max1}	2.365 N·m	2.931 N·m	2.776 N·m	2.576 N·m

From the obtained results (see Table 1) it can be concluded that the highest value of the fundamental harmonic amplitude of electromagnetic torque is demonstrated by the motor with a segment-shaped external rotor having non-magnetic spacing in the quadrature axis. However, the motor with such rotor design has the highest torque ripple coefficient. In order to reduce torque ripple, it is necessary to establish an even air gap as much as possible. For example, the first motor design (design (a)) has a small gap between rotor segments (pole coverage factor is 0.95) so that the torque ripple is smaller in comparison with design (b), but since the air gap is uneven due to stator slots, ripple is also significant. However, the motor design (a) has a smaller value of electromagnetic torque fundamental harmonic amplitude. By creating flux barriers in the rotor segments, it reduces quadrature magnetic flux, thereby increasing the electromagnetic torque. As inner surface of this rotor is even and the width of barriers is equal to that of slot opening, torque ripple is smaller.

5. CONCLUSIONS

Based on the results obtained in the present research, the following conclusions can be drawn:

1. Comparison of the studied rotor designs for a synchronous reluctance motor shows that the motor with a segment-shaped external rotor with non-magnetic space in the quadrature axis has the highest value of the electromagnetic torque fundamental harmonic amplitude. However, the same value for the motor with an external rotor with flux barriers is less than 5 %, and for the motor with an external segment-shaped rotor is less than 19 %.
2. The motor with non-magnetic barriers in the rotor has the smallest torque ripple. Torque ripple factor for the motor that has the rotor with non-magnetic space in quadrature axis is higher than 30 %.
3. In practice, the creation of the mechanical fastening in the flux barriers of the rotor does not affect the torque ripple, but slightly reduces the fundamental harmonic amplitude of electromagnetic torque.

ACKNOWLEDGEMENTS

The present research has been supported by the State Research Programme "LATENERGI".

REFERENCES

1. Levins, N., Pugachev, V., Dirba, J., & Lavrinovicha, L. (2013). High-reliability brushless synchronous motors for hand tools and household appliances. *Latvian Journal of Physics and Technical Sciences*, *50*(3), 3–11.DOI:10.2478/lpts-2013-0015
2. Pugachevs, V., Dirba, J., Kukjane (Lavrinovicha) L., Levins, N., & Orlova, S. (2012). Patent No. LV 14418 B. Riga: Patent Office of the Republic of Latvia (in Latvian).
3. Levins, N., Pugachevs, V., Dirba, J., Lavrinovicha, L., & Brakanskis, U. (2012). Patent No. LV 14627 B. Riga: Patent Office of the Republic of Latvia (in Latvian).
4. Lavrinovicha, L., Brakanskis, U., & Dirba, J. (2013). Synchronous reluctance motor without rotor ferromagnetic yoke. In *IEEE Eurocon 2013: IEEE Region 8 EuroCon 2013 Conference*, 2013, (pp. 1020–1024). Croatia, Zagreb. ISBN 9781467322317.
5. Bomela, X.B., & Kamper, M.J. (2002). Effect of stator chording and rotor skewing on performance of reluctance synchronous machine. *IEEE Transactions on Industry Applications*, *38*(1), 91–100.
6. Dirba, J., Lavrinovicha, L., & Dobriyan, R. (2015). Prospects of synchronous reluctance motors usage in low power electrical devices. *Latvian Journal of Physics and Technical Sciences*, *52*(2), 40–48. DOI: 10.1515/lpts-2015-0010
7. Dirba, J., Lavrinovicha, L., & Dobriyan, R. (2016). Study of the synchronous reluctance motor design. *Latvian Journal of Physics and Technical Sciences*, *53*(4), 22–29. DOI: 10.1515/lpts-2016-0025
8. Matyska, P. (2014). Advantages of synchronous reluctance motors. *Transactions on Electrical Engineering*, *3*(2), 44–47.
9. Lavrinovicha, L., & Dirba, J. (2015). *Brushless Synchronous Motors with External Rotor*. Riga: RTU Press (in Latvian).
10. Bianchi, N. (2005). *Electrical Machine Analysis Using Finite Elements.* USA: CRC Press, Taylor & Francis.

ĀRĒJĀ ROTORA IZSTRĀDE SINHRONAJAM REAKTĪVAJAM DZINĒJAM AR SAMAZINĀTĀM MOMENTA PULSĀCIJĀM

J. Dirba, L. Lavrinoviča, R. Dobrijans

Kopsavilkums

Aplūkotas jaunākās sinhrono reaktīvo dzinēju konstrukcijas ar ārējo rotoru. Analizēta ārējā rotora izpildījuma (segmentveida rotors, rotors ar papildu gaisa atstarpi pa šķērsasi un rotors ar vairākām nemagnētiskām barjerām) ietekme uz elektromagnētiskā momenta pulsācijām. Izmantojot magnētiskā laukā aprēķinus, iegūti momenta pulsāciju skaitliskie rezultāti dažādām ārējā rotora konstrukcijām.

08.09.2016.

LATVIAN JOURNAL OF PHYSICS AND TECHNICAL SCIENCES
2017, N 1

DOI: 10.1515/lpts-2017-0004

APPLICATION OF LOCAL FOURIER TRANSFORM TO MATHEMATICAL SIMULATION OF SYNCHRONOUS MACHINES WITH VALVE EXCITATION SYSTEMS

A. Fedotov, E. Fedotov, K. Bahteev

Kazan State Power Engineering University
51 Krasnoselskaya Str, Kazan, 420034, RUSSIA

The article proposes a method of mathematical simulation of electrical machines with thyristor exciters on the basis of the local Fourier transform. The present research demonstrates that this method allows switching from a variable structure model to a constant structure model. Transition from the continuous variables to the discrete variables is used. The numerical example is given in the paper.

Keywords: *mathematical modelling, thyristor exciter, local Fourier transform, synchronous machine, electromagnetic transients.*

1. INTRODUCTION

Mathematical models of synchronous machines used for the study of transients in the majority of cases are based on continuous mathematical methods. It is justified for dynamoelectric drivers because both processes and modelled objects are continuous in essence, as well as in principles of operation. However, there are key elements – thyristors – in an excited circuit of the synchronous machine. The complete system of differential equations describing the synchronous machine together with valve exciter contains periodic coefficients and has the variable structure, which is changing non-linearly in time.

Development of methods of mathematical simulation [1], [2] has allowed justifying feasibility of transition to the discrete sampling of regime parameters that, on the one hand, provides the fastest processing of information, and, on the other hand, reflects specifics of operation of valve elements present in the excitation system of the synchronous generators and engines.

The methods of the organisation of discrete mathematical models for electrical circuits with valve converters are well developed in [2]–[6]. It has been shown that by means of the local Fourier transform (LFT) it is possible to obtain mathematical models in a finite-difference form or rather step images for the synchronous machines with an independent thyristor and self-excitation. The switching of the

valves causing local indignations of the mode is not taken into consideration, and the created models describe macro processes as they are the main object of the research.

2. METHOD

The LFT method is as follows. We consider continuous function $f(t)$ (Fig. 1) and also allocate some m interval to borders $[t^{(m)}; t^{(m)} + h^{(m)}]$. We periodically continue the function $f(t)$, considered only within the limits of the allocated interval, on the both sides of the allocated interval (Fig. 1). Thereby we receive new function $f_p(t)$, which has the following properties: first, it is periodic with the period $h^{(m)}$; secondly, on the interval of values of argument $t \in (t^{(m)}; t^{(m)} + h^{(m)})$, it identically coincides with the required function, i.e., $f_p(t) \equiv f(t)$; thirdly, in boundary points $t = t^{(m)}$ and $t = t^{(m)} + h^{(m)}$ function $f_p(t)$ has ruptures of the first type.

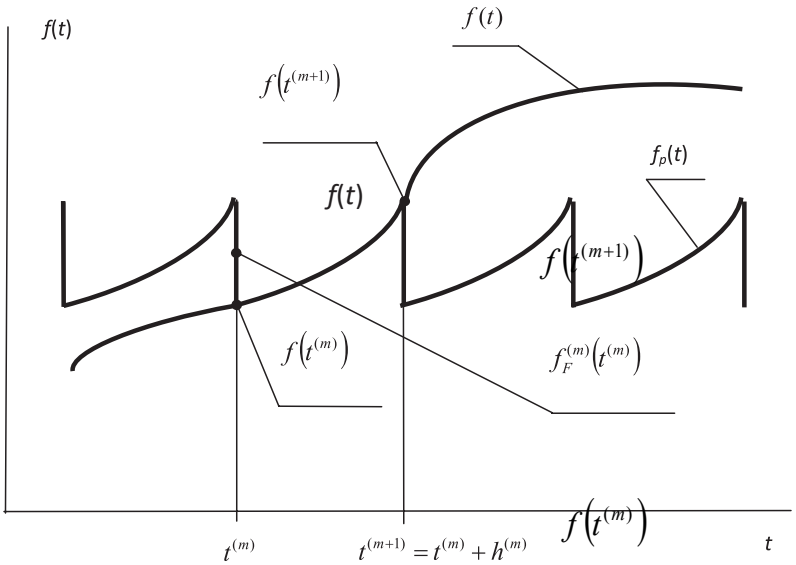

Fig. 1. The periodization of non-periodic functions.

It is known that such a function can be represented by the Fourier series $f_F(t)$, in addition

$$f_p^{(m)}(t) \equiv f_F^{(m)}(t) = C_0^{(m)} + \sum_{n=1}^{n=\infty} C_k^{(m)} \cos k(t - t^{(m)}) + S_k^{(m)} \sin k(t - t^{(m)}), \qquad (1)$$

$$k = \frac{2\pi n}{h^{(m)}}; \qquad n = 0, \pm 1, \pm 2, \ldots; \quad t \in (t^{(m)}; t^{(m)} + h^{(m)});$$

$$C_0^{(m)} = \frac{1}{h^{(m)}} \int_{t^{(m)}}^{t^{(m)}+h^{(m)}} f(t) d\theta; \quad C_k^{(m)} = \frac{2}{h^{(m)}} \int_{t^{(m)}}^{t^{(m)}+h^{(m)}} f(t) \cos k(t - t^{(m)}) d\theta;$$

$$S_k^{(m)} = \frac{2}{h^{(m)}} \int_{t^{(m)}}^{t^{(m)}+h^{(m)}} f(t) \sin k(t - t^{(m)}) d\theta.$$

Since the function $f_p(t)$ in points $t = t^{(m)}$ and $t = t^{(m)} + h^{(m)}$ has discontinuities, for the Fourier series the following relations are valid:

$$f_F\left(t^{(m)}\right) = f_F\left(t^{(m)} + h^{(m)}\right) = f\left(t^{(m)}\right) + \frac{1}{2}\left\{f\left(t^{(m)} + h^{(m)}\right) - f\left(t^{(m)}\right)\right\} = \\ = f_l^{(m)} + \frac{1}{2}\Delta f_l^{(m)} = C_0^{(m)} + \sum_{n=1}^{\infty} C_k^{(m)}. \tag{2}$$

Expression (2) is one of the main equations used in this method, because it relates the continuous parameters (Fourier series) with discrete – with the countdown of function $f_l^{(m)}$ (i.e., with its value in the point $t = t^{(m)}$ and with its final difference $\Delta f_l^{(m)}$.

The following integral is the local Fourier transform (F-conversion):

$$F\{f(t)\} = F(m,k) = \frac{2}{h^{(m)}} \int_{t^{(m)}}^{t^{(m)}+h^{(m)}} f(t) e^{-jk\left(t - t^{(m)}\right)} dt, \tag{3}$$

where $k = \dfrac{2\pi n}{h^{(m)}} = \omega^{(m)} n$; $n = 0, \pm 1, \pm 2, \ldots$; $m = 1, 2, \ldots$, and $F(m,k)$ is a local image (image A) of function $f(t)$, wherein

$$f\left(t^{(m)}\right) = \frac{1}{2}\sum_{n=-\infty}^{\infty} F(m,k) - \frac{1}{2}\Delta f\left(t^{(m)}\right) = \frac{1}{2}F(m,0) + \sum_{n=1}^{\infty} C_k^{(m)} - \frac{1}{2}\Delta f\left(t^{(m)}\right). \tag{4}$$

Expression (4) is already sufficient to organise numerical procedures of the solution of the linear differential equations with the constant coefficients, leading them in accordance with (4) to the final-difference equations. We consider the analytical possibilities of the F-image summation according to (4). If they can be presented in the form

$$F(m,k) = \sum_{i=1}^{I} D(jk) A_i(m)$$

on the basis of the theorem of deductions, we obtain

$$\sum_{n=-\infty}^{\infty} F(m,k) = -j\pi \sum_{i=1}^{I} A_i(m) \sum_{s=1}^{S} b_{si}\, ctg\left(j\pi a_{si}\right), \tag{5}$$

where S – the number of the function poles (simple) of a complex variable $D(p)$, whose deductions in poles $p = a_{si}$ are equal to b_{si}. $D(p)$ turns out from $D(jk) = D\left(j\omega^{(m)} n\right)$ by replacement $jn = p$. It is convenient to use in case of the valid values a_{si}.

$$j\pi ctg\left(j\pi a_{si}\right)=\pi cth\left(\pi a_{si}\right).$$

If $D\left(jk\right)$ forms final sequence of the n, formula (6) is inapplicable and it is necessary to use formula (5) of direct summation.

Thus, we receive $f\left(t^{(m)}\right)=\frac{-j\pi}{2}\sum_{i=1}^{I}A_i\left(m\right)\sum_{s=1}^{S}b_{si}ctg\left(j\pi a_{si}\right)-\frac{1}{2}\Delta f\left(t^{(m)}\right).$

We show the use of local Fourier transform for the formation of the discrete mathematical model of the synchronous machine with the system of independent thyristor excitation from the transformer connected to an electrical network (Fig. 2.)

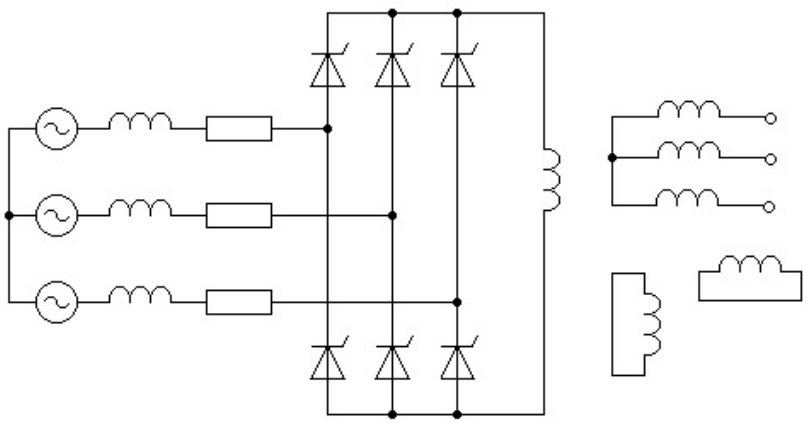

Fig. 2. The schematic diagram of the synchronous machine and its exciter.

Resistances r_c, x_c correspond to a field winding supply circuit from alternating current, EMFs *E* forms a direct sequence.

We accept the following assumptions: input equations of the synchronous machine use the model of Park-Goreva with the equivalenting conversion of damping circuits of one winding in a longitudinal axis and one winding in a lateral axis; the axis *d* advances an axis *q*. The valves of the managed converter, which is collected on a three-phase bridge circuit, are considered ideal; they work in the main mode – the mode of the serial conductivity of two and three valves, and the angle of thyristors control α is digitized from null value of the corresponding phase EMF. In the equations of the synchronous machine, we save the standard designations [7]. In the equations of discrete model, we use the "walking" coordinate system, which is displaced giving the next control signal on thyristor in an angular measure of π/3 radians (duration of an interval of repeatability of the converter).

The classical equations of Park-Goreva for the synchronous machine are written using a system of the relative units x_{ad}:

$$
\left.
\begin{aligned}
&-u_d = ri_d + \frac{d}{d\theta}(x_d i_d + x_{ad} i_f + x_{ad} i_{1d}) + x_q i_q + x_{aq} i_{1q},\\
&-u_q = ri_q + \frac{d}{d\theta}(x_q i_q + x_{aq} i_{1q}) - (x_d i_d + x_{ad} i_f + x_{ad} i_{1d}),\\
&u_f = r_f i_f + \frac{d}{d\theta}(x_{ad} i_d + x_f i_f + x_{ad} i_{1d}),\\
&0 = r_{1d} i_{1d} + \frac{d}{d\theta}(x_{ad} i_d + x_{ad} i_f + x_{1d} i_{1d}),\\
&0 = r_{1q} i_{1q} + \frac{d}{d\theta}(x_{aq} i_q + x_{1q} i_{1q}).
\end{aligned}
\right\} \qquad (6)
$$

We connect through the equations the electric field of a winding of excitement and a power line. In the m-th local interval of recurrence of the converter within duration of the commutation of the phases γ connected to switching of valves, the following equation is obtained in the system of the walking coordinates:

$$
u_f^{(m)} = \sqrt{3}E\cos\left(\theta - \pi/3\right) - 2r_c i_f^{(m)} - 2x_c \frac{di_f^{(m)}}{d\theta} + r_c i_\gamma^{(m)} + x_c \frac{di_\gamma^{(m)}}{d\theta}, \qquad (7)
$$

where $\theta = \omega t$, $\theta \in [\alpha; \alpha + \gamma]$; $i_\gamma^{(m)}$ – the exciter current phase, ending switching, and $i_\gamma^{(m)}(\alpha) = i_f^{(m)}(\alpha)$, $i_\gamma^{(m)}(\alpha + \gamma) = 0$.

Outside the switching interval, when $\theta \in [\alpha + \gamma;\ \alpha + \pi/3]$ it is also possible to use equation (7) in case $i_\gamma^{(m)} \equiv 0$.

If we apply the local integral conversion [1], which is a special case of LFT, to equation (7), i.e., according to terminology [1] to pass to the "step images" of variables

$$
F_s = \frac{3}{\pi} \int_\alpha^{\alpha+\pi/3} f(\theta) d\theta,
$$

considering boundary conditions for switching current $i_\gamma^{(m)}$ we receive

$$
U_{fs}^{(m)} = \frac{3\sqrt{3}}{\pi} E\cos(\alpha - \pi/6) - 2r_c I_{fs}^{(m)} - \frac{3}{\pi}(x_c - r_c\gamma/2) I_{fl}^{(m)} - \frac{6}{\pi} x_c \Delta I_{fl}^{(m)}, \qquad (8)
$$

where the lower *s* index belongs to the mean value of a required variable on *m* interval of recurrence of the converter, the index *l* corresponds to the value of the variable in the switching point, i.e., at the time of submission of the controlling signal to the next thyristor of the converter that is illustrated by the following formula:

$$
\Delta I_{fl}^{(m)} = i_f^{(m)}(\alpha + \pi/3) - i_f^{(m)}(\alpha) = I_{fl}^{(m+1)} - I_{fl}^{(m)}.
$$

The rectilinear approximation is used in integration of equation (7). Expression (8) describes a response external characteristic of the transformer in the discrete variables. It is obtained mathematically within the accepted assumptions. Taking into consideration smoothness of the straightened current, we assume that $I_{fs}^{(m)} = I_{fl}^{(m)}$.

Let us assume that the synchronous generator mentioned above has outputs connected to the active and inductive load r_w, x_w.

$$\left.\begin{aligned} u_d &= r_w i_d + x_w \frac{di_d}{d\theta} + x_w i_q, \\ u_q &= r_w i_q + x_w \frac{di_q}{d\theta} - x_w i_d. \end{aligned}\right\} \tag{9}$$

Having applied LFT to equations (6), (7) and (9), we receive the equations of the synchronous generator together with its activator in the field of F-images

$$\left.\begin{aligned}
&(r_s + jkx_{ds})\dot{I}_d(m,k) + jkx_{ad}\dot{I}_f(m,k) + jkx_{ad}\dot{I}_{1d}(m,k) + x_{qs}\dot{I}_q(m,k) + \\
&+ x_{aq}\dot{I}_{1q}(m,k) = -\frac{6}{\pi}x_{ds}\Delta I_d^{(m)} - \frac{6}{\pi}x_{ad}\Delta I_f^{(m)} - \frac{6}{\pi}x_{ad}\Delta I_{1d}^{(m)}, \\
&- x_{ds}\dot{I}_d(m,k) - x_{ad}\dot{I}_f(m,k) - x_{ad}\dot{I}_{1d}(m,k) + (r_s + jkx_{qs})\dot{I}_q(m,k) + \\
&+ jkx_{aq}\dot{I}_{1q}(m,k) = -\frac{6}{\pi}x_{qs}\Delta I_q^{(m)} - \frac{6}{\pi}x_{aq}\Delta I_{1q}^{(m)}, \\
&jkx_{ad}\dot{I}_d(m,k) + (r_{fs} + jkx_{fs})\dot{I}_f(m,k) + jkx_{ad}\dot{I}_{1d}(m,k) = -\frac{6}{\pi}x_c I_{fl}^{(m)} + \\
&+ \dot{B}(m,k)(r_c + jkx_c)I_{fl}^{(m)} - \frac{6\sqrt{3}}{\pi}E\frac{\cos(\alpha - \pi/6) + jk\sin(\alpha - \pi/6)}{k^2 - 1} - \\
&- \frac{6}{\pi}x_{ad}\Delta I_d^{(m)} - \frac{6}{\pi}x_{fs}\Delta I_f^{(m)} - \frac{6}{\pi}x_{ad}\Delta I_{1d}^{(m)}, \\
&jkx_{ad}\dot{I}_d(m,k) + jkx_{ad}\dot{I}_f(m,k) + (r_{1d} + jkx_{1d})\dot{I}_{1d}(m,k) = \\
&= -\frac{6}{\pi}x_{ad}\Delta I_d^{(m)} - \frac{6}{\pi}x_{ad}\Delta I_f^{(m)} - \frac{6}{\pi}x_{1d}\Delta I_{1d}^{(m)}, \\
&jkx_{aq}\dot{I}_q(m,k) + (r_{1q} + jkx_{1q})\dot{I}_{1q}(m,k) = -\frac{6}{\pi}x_{aq}\Delta I_q^{(m)} - \frac{6}{\pi}x_{1q}\Delta I_{1q}^{(m)},
\end{aligned}\right\} \tag{10}$$

where $r_s = r + r_w$, $x_{ds} = x_d + x_w$, $x_{qs} = x_q + x_w$, $r_{fs} = r_f + 2r_c$, $x_{fs} = x_f + 2x_c$.

The complex coefficient $\dot{B}(m,k)$ that enters equation (10) pays off in the following equation:

$$\dot{B}(m,k) = \frac{6}{\pi}\frac{1 - jk\gamma - e^{-jk\gamma}}{k^2\gamma}.$$

Complex variables are convenient if we pass to the finite-difference equations in the analytical view from equation (5). If in equations (10) we pass from complex to the valid variables by changeover

$$\dot{I}_i(m,k) = I_i^c(m,k) + jI_i^s(m,k), \quad i = d,\ q,\ f,\ 1d,\ 1q$$

and calculate a limited row:

$$f_l^{(m)} = \frac{1}{2}F(m,0) + \sum_{n=1}^{N}F^c(m,k) - \frac{1}{2}\Delta f^{(m)}, \quad k = \frac{2\pi n}{h}, \tag{11}$$

where N – the number of the considered members of a row, we obtain the convenient numerical method for formation of a mathematical model of the synchronous machine of the discrete type of constant structure, in which internal switching transient phenomena are not taken into account.

Irrespective of existence of the gate transformer in a generator exciting circuit the speed of computation in the discrete model is significantly higher than in case of integration of the equations in the instantaneous values of variables in the Runge-Kutta method.

It is interesting to consider and evaluate the possibility of using the simplified discrete model when the entire range of EMF of network and switching current is not considered in the field of images. In this case, the appropriate equation for a circuit of the excitation winding of the synchronous machine takes the following form:

$$\left.\begin{aligned} & jkx_{ad}\dot{I}(m,k)+(r_{fs}+jkx_{fs})I_f(m,k)+jkx_{ad}\dot{I}_{1d}(m,k)= \\ & =C\frac{6\sqrt{3}}{\pi}E\cos(\alpha-\pi/6)-\frac{6}{\pi}(x_c-Cr_c\gamma/2)I_{fl}^{(m)}- \\ & -\frac{6}{\pi}x_{ad}\Delta I_d^{(m)}-\frac{6}{\pi}x_{fs}\Delta I_{fl}^{(m)}-\frac{6}{\pi}x_{ad}\Delta I_{1d}^{(m)}, \\ & C=\begin{cases}1, & k=0,\\ 0, & k\neq 0.\end{cases} \end{aligned}\right\} \qquad (12)$$

It is done in order not to complicate needlessly the mathematical model of the synchronous machine. This example shows that the results of calculations for both models, which show that transition from the continuous model to the discrete one, provide more exact reflection of the occurring processes even in the case of the same initial simplifications.

Example 1. We consider the mode of the three-phase short circuit on the outputs of the idling synchronous generator without damping windings. The generator parameters in relative units:

$x_d=1.0;\quad x_q=0.7;\quad x_{ad}=0.6;\quad x_f=1.43;\quad r=0.0145;\quad r_f=0.0015;$
$r=0.0145;\quad r_f=0.0015;$ excitement data: $x_c=0.001; r_c=0.0002; E=0.004$.

The initial value of current of excitement is $i_f(0)=1.014$. The comparison of calculation results for the instantaneous values of variables during intervals of the persistence of structure of the transformer (reference model) and in the discrete model (10) showed their almost complete coincidence in switching points.

We also estimate the accuracy of calculations using the simplified model of the exciter (12) where the power-supply circuit of a winding of excitement is described by equation (8). At the same time, we show the sequence of the numerical calculations.

Having passed from complex to the valid variables, we obtain the following equations:

$$\begin{bmatrix} r & -kx_d & 0 & -kx_{ad} & x_q & 0 \\ kx_d & r & kx_{ad} & 0 & 0 & x_q \\ 0 & -kx_{ad} & r_{fs} & -kx_{fs} & 0 & 0 \\ kx_{ad} & 0 & kx_{fs} & r_{fs} & 0 & 0 \\ -x_d & 0 & -x_{ad} & 0 & r & -kx_q \\ 0 & -x_d & 0 & -x_{ad} & kx_q & r \end{bmatrix} \begin{bmatrix} I_d^c(m,k) \\ I_d^s(m,k) \\ I_f^c(m,k) \\ I_f^s(m,k) \\ I_q^c(m,k) \\ I_q^s(m,k) \end{bmatrix} =$$

$$\begin{bmatrix} -x_d & -x_{ad} & 0 & 0 & 0 \\ 0 & 0 & 0 & 0 & 0 \\ -x_{ad} & -x_{fs} & 0 & -x_c + C\frac{r_c\gamma}{2} & C\frac{\pi}{3} \\ 0 & 0 & 0 & 0 & 0 \\ 0 & 0 & -x_q & 0 & 0 \\ 0 & 0 & 0 & 0 & 0 \end{bmatrix} \begin{bmatrix} \Delta I_d^{(m)} \\ \Delta I_f^{(m)} \\ \Delta I_q^{(m)} \\ I_{fl}^{(m)} \\ E_f \end{bmatrix}, \tag{13}$$

where $E_f = \dfrac{3\sqrt{3}E}{\pi}\cos(\alpha - \pi/6).$

We make the calculation of the system coefficients of differential equations in the following sequence. We add a matrix column $\begin{bmatrix}1 & 0 & 0 & 0 & 0\end{bmatrix}_t$ to the right part of equations (13) instead of the existing matrix column with variables. We assume that $k=6n$ concerning variables with upper index c and we add to each of them the results of calculation according to formula (11). Thus, we obtain the column of system coefficients of differential equations at the final difference $\Delta I_d^{(m)}$. Then we substitute a matrix $\begin{bmatrix}0 & 1 & 0 & 0 & 0\end{bmatrix}_t$ and so on. The following system of differential equations is obtained at the number of members of row N=55 and the control angle α=1 radian for the accepted parameters:

$$\begin{bmatrix} I_{dl}^{(m)} \\ I_{fl}^{(m)} \\ I_{ql}^{(m)} \end{bmatrix} = \begin{bmatrix} 180.36 & 431.69 & 0.58601 & 0.27693 & -315.69 \\ -301.56 & -720.22 & 0.034457 & -0.46168 & 526.32 \\ -4.9849 & -9.6852 & -0.51573 & -0.0057363 & 6.5394 \end{bmatrix} \times$$
$$\times \begin{bmatrix} \Delta I_{dl}^{(m)} & \Delta I_{fl}^{(m)} & \Delta I_{ql}^{(m)} & I_{fl}^{(m)} & E_f \end{bmatrix}_t \tag{14}$$

The lower index t means the transposed matrix.

This equation serves for the determination of the switching angle γ:

$$\cos(\alpha + \gamma - \pi/6) = \left(1 - \frac{6x_c}{\pi(r_{fs} - 3\gamma r_c/2\pi + 3x_c/\pi)}\right)\cos(\alpha - \pi/6).$$

Equations (14) now need to be written with respect to finite differences. Using the same algorithm (except for summation), we find that

$$\begin{bmatrix} \Delta I_d^{(m)} \\ \Delta I_f^{(m)} \\ \Delta I_q^{(m)} \end{bmatrix} = \begin{bmatrix} -0.67421 & -0.39295 & -0.79238 & -0.58020 \\ 0.28235 & 0.16254 & 0.33175 & 0.97371 \\ 1.2143 & 0.73470 & -0.51012 & 0.0020833 \end{bmatrix} \begin{bmatrix} I_{dl}^{(m)} \\ I_{fl}^{(m)} \\ I_{ql}^{(m)} \\ E_f \end{bmatrix}. \tag{15}$$

The calculation results of the transition process for the reference method and the equations (15) are given in Fig. 3 at α=1 and α=2.

3. DISCUSSION

The values of currents of the reference model are caused only in switching points and connected for the descriptive reasons by continuous bending. The values of currents of the discrete model are caused in the form of circles.

The step of discretization is set by the diagram of thyristor exciters of the synchronous machine. Six points for the period of industrial frequency are quite sufficient for adequate display of electromagnetic transition process. The local transient process can be restored in each interval of discretization, if necessary. In this case, the initial values of the variables are the values of discrete variables of the previous interval.

The comparison shows that the simplified accounting of the exciter is quite correct both at low and at high control angles.

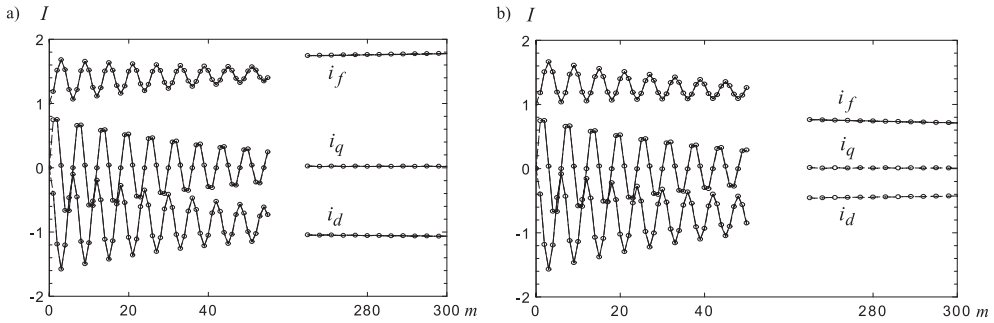

Fig. 3. Currents i_d, i_f, i_q of the synchronous generator calculated in the reference and discrete mathematical models.

a – the angle of management, α=1; b – the angle of management, α=2;

4. CONCLUSION

Thus, the local Fourier transform allows creating the mathematical model of the dynamoelectric and gate system, which initially represents the system of variable structure in a finite-difference type of constant structure. In this case, information on a transient phenomenon is provided in switching points at a frequency of 6 times during the industrial frequency (a bridge circuit of rectification). The present research has provided both numerical and analytical opportunities for further use of the obtained mathematical model for research of transient phenomena in electrical power systems without introduction of the simplifying assumptions in relation to gate drivers.

ACKNOWLEDGEMENTS

The presented results have been obtained in the scientific research "Methods of Increase of Reliability and Quality of Electric Power Supply in Distribution Net-

works" (the task number 2014/448 on the implementation of government works in the field of scientific activities of the base portion of the state task of the Ministry of Education and Science of Russia).

The research has been supported by the autonomous non-profit organisation "Kazan Open University Talent 2.0".

REFERENCES

1. Boldea, I., & Tutelea, L.N. (2009). *Electric Machines: Steady State, Transients, and Design with MATLAB*. New York: CRC Press, Taylor & Francis.
2. Kovacs, P.K. (1984). *Transient Phenomena in Electrical Machines* (1st ed.). Budapest: Akadémiai Kiadó.
3. Lipo, T.A. (2012). *Analysis of Synchronous Machines* (2nd ed.). Florida: CRC Press.
4. Simões, M.G., & Farret, F.A. (2015). *Modeling and Analysis with Induction Generators* (3rd ed.). Florida: CRC Press, Taylor & Francis Group.
5. Milano, F. (2010). *Power System Modelling and Scripting*. London: Springer-Verlag Limited.
6. Sood, V.K. (2004). *HVDC and FACTS Controllers. Applications of Static Converters in Power Systems*. Boston: Kluwer Academic Publishers.
7. Kolcun, M., Griger, V., & Mühlbacher, J. (2003). *Electric Power System Operation Control*. Czech Republic: Pilsen.
8. Kolcun, M., Mühlbacher, J., & Haller, R. (2004). *Mathematical Analysis of Electrical Networks*. Prague: BEN – technica literatura.
9. Takeuchi, T.J. (1968). *Theory of SCR Circuit and Application to Motor Control.* Tokyo: Electrical Engineering College Press.

SINHRONO MAŠĪNU AR VĀRSTU IEROSMES SISTĒMĀM MATEMĀTISKĀ MODELĒŠANA, IZMANTOJOT VIETĒJO FURJĒ TRANSFORMĀCIJU

A. Fedotovs, E. Fedotovs, K. Bahtejevs

K o p s a v i l k u m s

Raksta autori piedāvā elektrisko mašīnu ar tiristoru ierosinātāju matemātiskās modelēšanas metodi, izmantojot vietējo Furjē transformāciju. Pētījums parāda, ka šī metode ļauj pārslēgties no mainīgās struktūras modeļa uz pastāvīgās struktūras modeli. Pētījumā tiek izmantota pāreja no nepārtrauktiem mainīgajiem uz diskrētiem mainīgajiem lielumiem. Rakstā piedāvāts arī skaitlisks piemērs.

23.09.2016.

LATVIAN JOURNAL OF PHYSICS AND TECHNICAL SCIENCES
2017, N 1
DOI: 10.1515/lpts-2017-0005

SOLID STATE PHYSICS

THE STUDY OF ADSORPTION PROCESS OF PB IONS USING WELL-ALIGNED ARRAYS OF ZnO NANOTUBES AS A SORBENT

M. Krasovska, V. Gerbreders, E. Tamanis, S.Gerbreders, A.Bulanovs
G.Libert's Innovative Microscopy Centre, Daugavpils University
1 Parades Str., Daugavpils, LV-5401, LATVIA

Well-structured ZnO nanotubes are obtained by a self-selective etching method with lowering temperatures of growth during the hydrothermal process.

The structural and optical properties of the obtained nanostructures are investigated by various conventional methods.

The goal of the research is to compare the efficiency of ZnO nanotubes to that of ZnO nanorods during lead adsorption process from aqueous solution and demonstrate that hollow nanostructures are more effective than solid nanostructures of the same morphology due to their larger effective surface.

Both nanotubes and nanorods are obtained under similar growth conditions: neither growth solution composition, nor concentration is changed. ZnO morphology is switched only by changing temperature during the growth process.

The measurements are carried out to assess the efficiency of the adsorption per unit weight of ZnO nanorod and nanotube capacity of static adsorption.

Keywords: *hydrothermal crystal growth, lead adsorption, nanotube, ZnO.*

1. INTRODUCTION

Nowadays, due to increased manufacturing and traffic intensity pollution of the environment by heavy metals, such as lead, cadmium, mercury, cobalt, cuprum, arsenic, has become one of the most topical problems [1]–[6].

Heavy metal ions are toxic and cancerogenic; they are accumulated by living organisms causing long-term intoxication and a lot of chronicle and acute diseases [1], [2].

One of the most dangerous environmental pollutants is lead [7]–[9]. As a result of manufacturing, such as leather and textile treatment and fabrication, metal-working, pharmacy, chemical and battery manufacturing etc., it is released into the atmosphere and subterranean waters as well as into soil with further accumulation by plants.

Due to high hazardous properties of heavy metals, it is very important to minimise humans' contact probability with sources of lead ions, and one of the solutions to this problem is higher purification of wastewater to prevent lead ions from entering the environment.

Various treatment techniques have been developed for the removal of toxic contaminants from wastewater, such as adsorption, ion exchange, chemical precipitation, membrane-based filtration, reverse osmosis, coagulation-sedimentation and so on; however, the most promising and effective method is adsorption [1], [2].

This method is easily performed, inexpensive and sensitive to both organic and nonorganic pollutants, for example, for removal of several kinds of metal ions, organic dues and so on.

In many studies, special attention is devoted to mesoporous and nanostructured materials as a sorbent due to a significantly larger effective area and a higher number of active bounds compared to bulk material of similar composition [4], [7], [10], [11].

ZnO nanostructures are a promising candidate for many purposes: they are sensitive to all heavy metal ions to a greater or lesser extent and show excellent adsorption results for most hazardous ones, such as lead, cadmium and mercury [2]–[5], [10], [12]. ZnO nanostructures are presented in multiple morphologies and that is why it is possible to change sorption properties depending on the intended purpose and kind of pollutant without changing initial chemicals and sorbent obtaining method. Another important feature is that ZnO is chemically inactive; therefore, it does not cause secondary pollution.

As shown in [4], ZnO nanostructures demonstrate good regeneration and reusability without significant loss of sorption capacity for subsequent cycles after three desorption cycles that lower the overall cost of the adsorption process and are environmentally friendly.

2. MATERIALS AND METHODS

2.1 Seed Layer Growth

Seed layer was obtained to provide orientation of nanotubes along vertical direction during epitaxial growth process and ensure good connection of nanostructure with smooth surface of the substrate.

Previous research [13] shows that one of the most optimal methods for obtaining the seed layer is growing from zinc acetate ethanol solution. Acetate-delivered seed layer provides good crystallinity and orientation along z-direction, and only acetate seed provides needle-like nanorod with sufficiently large diameter for further transformation into nanotubes during a two-step hydrothermal growth process.

Samples were prepared under the following conditions. Glass plates were cleaned by consistent immersing in alkaline and acidic aqueous solutions, several times rinsed with deionized water and dried at 90˚C for 30min. Then glass plates were dipped into ultrasonically shaken flask containing 5 mmol Zinc acetate $Zn(CH_3COOH)_2*2H_2O$ ethanol solution, then rinsed in pure ethanol and dried with

nitrogen gas flow.

This procedure was repeated 2–4 times depending on the desired fineness of seed layer. After dipping procedure the samples were annealed at 250˚C for 30 min to convert acetate layer to ZnO during calcination.

2.2 ZnO Nanotube Growth

ZnO nanotubes were obtained using the hydrothermal growth method.

For this purpose 0.1M equimolar zinc nitrate hexahydrate ($Zn(NO_3)_2*6H_2O$) and hexametientetramine HMTA ($C_6H_{12}N_4$) aqueous solution were prepared and several chemical reactions took place:

$$C_6H_{12}N_4+6H_2O\rightarrow 6HCHO+4NH_3 \quad (1)$$

$$NH_3+H_2O\rightarrow NH_4^{+}+OH^{-} \quad (2)$$

$$2OH^{-}+Zn^{2+}\leftrightarrow Zn(OH)_2 \quad (3)$$

$$Zn(OH)_2\leftrightarrow ZnO+H_2O \quad (4)$$

In these reactions, zinc nitrate provided the source of Zn^{2+} ions, but HMTA produced slightly alkaline medium and provided Zn^{2+} ions with OH^{-}.

All mentioned reactions were in equilibrium and might be shifted from equilibrium condition by changing physical parameters of reaction such as growth temperature, concentration of precursor, pH and growing time.

In this way, it is possible to obtain nanostructures with tunable morphology, size and density of distribution depending on the initial purposes of research [13].

Working solution was poured into a beaker with lid and then glass plates with seed layer were immersed face downward with the aim to prevent undesirable sedimentation during the chemical reaction.

Beaker was placed into the preheated LINN HIGH THERM furnace and then temperature was maintained 90 ˚C.

The growing process occurred during two stages:

a. Temperature was set to 90 ˚C and maintained for 3h;

b. Temperature was lowered to 50 ˚C–60 ˚C and maintained for 18h–20h;

This sequence of the process corresponds to the principles of self-selective etching method, when at the first stage in relatively short time at a high temperature the growing process of ZnO nanorods intensively occurs in both lateral and axial directions, but after lowering the temperature in a significantly longer time period, compared to the first stage, the aging process occurs when ZnO metastable planes are etched during the chemical reaction with residual chemicals of growth solution [14]–[17].

It should be noted that the growth and aging processes occur at both stages, but at the second stage in constant volume of solution after a long period of growth supply of Zn^{2+} ions is already exhausted; therefore, growth process of nanotubes is suppressed and the etching processes begin to dominate.

In comparison with obtaining the nanotubes during chemical etching, the self-selective method has a lot of advantages: it is mild, selective and non-degradable for the whole surface of nanorod (during the indicated time period only metastable planes are etched) and there is no contact with additional chemicals that raises purity of the obtained sample.

As shown in Fig. 1, there are two kinds of nanotubes: the fully etched nanotubes with a deep hole and the ones that are partially formed with low walls and easily visible basis.

The second type of nanotubes may experience another mechanism of growth [18].

According to the nucleation theory, growth species with higher probability will condense at places with a higher number of neighbour particles such as defects, steps, edges.

For an atomically flat 2D growth surface without defects and steps, higher binding energies at the edges will enable selective condensation of growth species at the edges. For ZnO, it is well known that the growth rate along the c-axis is relatively faster; thus, if the decreased growth temperature is low enough to suppress migration along the 2D surface of the c-plane but high enough to sustain the growth along the c axis, the condensation and growth will be limited at the edges of the c-plane of ZnO that causes the formation of nanotubes on the nanorod base.

The dominating growing mechanism depends on Zn-terminated or O-terminated plane completes {002} plane at the end of the first stage of growth before lowering the temperature.

Experimentally found duration of growth stages provides optimal dimensions and etching intensity of the obtained nanostructures, when nanotubes are sufficiently etched, but are not fully destroyed [13].

2.3 Analysis of Morphology and Structural Properties

Morphological and structural composition of the obtained sample was determined using the scanning electron microscope TESCAN-VEGA LMU II.

For structural and phase composition determination, XRD spectra were obtained using RIGAKU Smart Lab Cu-Kα (λ=1.543 Å) at parallel beam scanning geometry and additional Ge(220)x2 bounce monochromator.

2.4 Analysis of Lead Ion Adsorption Process

Optical measurements were carried out by Shimatzu spectrophotometer.

With the aim to analyse adsorption processes of Pb^{2+} ions using ZnO nanotubes as a sorbent, lead nitrate aqueous solution of different concentrations (30mM/l-300mM/l) was obtained (see reaction 5).

$$Pb(NO_3)_2 \leftrightarrow Pb^{2+} + 2NO_3^- \quad (5)$$

Glass plates covered with nanotubes were placed into cuvette containing zinc nitrate aqueous solution and transmittance spectrum measurements for each concentration were carried out.

For comparison purposes, the same procedure was carried out for nanorod-covered plates obtained at 0.1M equimolar $Zn(NO_3)_2$ and HMTA solution at 90 ˚C for 3h.

Chemical composition of adsorbed layer was determined by INCA EDS, but for phase composition determination XRD spectra were taken.

Deposition mechanism was explained as precipitation due to covalent bond formation between Pb (II) ions and ZnO surface (A bond). Donor-acceptor or coordination bond is also possible between surface of ZnO and Pb (II) (B bond) (Fig. 2 e) [4].

As shown in [2], the adsorption process depends on pH of solution. When pH> pH_{pzc}, where pH_{pzc} is pH level at a zero charge point, chelate complexes between ZnO nanoparticles and Pb ions form. At a low pH level, chelate sites occupy H^+ making them neutral. This adsorption mechanism is preferential, but also a small amount of Pb (II) can be adsorbed at pH < pHpzc during the ion exchange mechanism. It means that Pb^{2+} has greater affinity to ZnO compared with H^+ so that H^+ can be exchanged by metal ion during ion exchange. Ion exchange process occurs more slowly than surface complexation (formation of chelate complexes) during presence of organic molecular impurities on surface of ZnO nanostructures, which causes steric factor during the metal ion adsorption process.

3. RESULTS AND DISCUSSION

SEM images and XRD spectra of the obtained ZnO nanotubes samples are shown in Fig. 1.

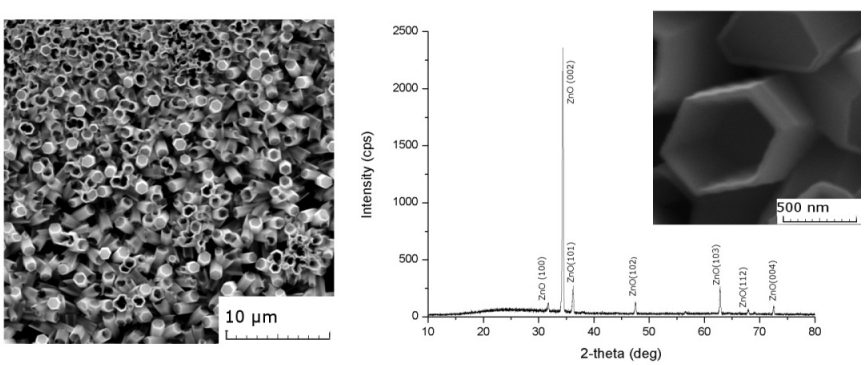

Fig. 1. SEM image of the prepared ZnO nanotubes and XRD pattern of the obtained nanostructures. Inset displays high-resolution SEM image of single nanotube with wall thickness of about 50nm.

The array of obtained nanotubes is well aligned with the preferred orientation along vertical direction as evidenced by higher peak intensity compared to another that corresponds to {002} plane. Low intensity of amorphous background indicates that samples are highly crystallized and the analysis of the obtained peak shows no mismatching in the presence of ZnO crystalline phase.

For Pb^{2+} ion adsorption process analysis, samples were cut into narrow strips and placed to the Petri dish containing 300mM/l-30mM/l $Pb(NO_3)_2$ aqueous solution under continuous stirring.

SEM images display (Fig. 2) that by decreasing concentration of working solution the size of crystallites, which were formed due to the adsorption process, significantly increases. This is due to the fact that at high concentration of precursor growth particles with higher probability cooperate to create new seed grain instead of participating in the existing grain.

Chemical composition determined by EDS shows that deposition of lead ions occurs intensively, the sediment contains only Zn and O and XRD pattern of sample after adsorption procedure confirms (Fig. 3) that sediment consists of different kinds of lead oxides and monoclynic α- modification of Pb_2O_3 and rhombic $Pb_3O_2(NO_3)_2$ are the most widely represented ones. Corresponding to the shape of each crystal system, crystallites are observed from SEM images.

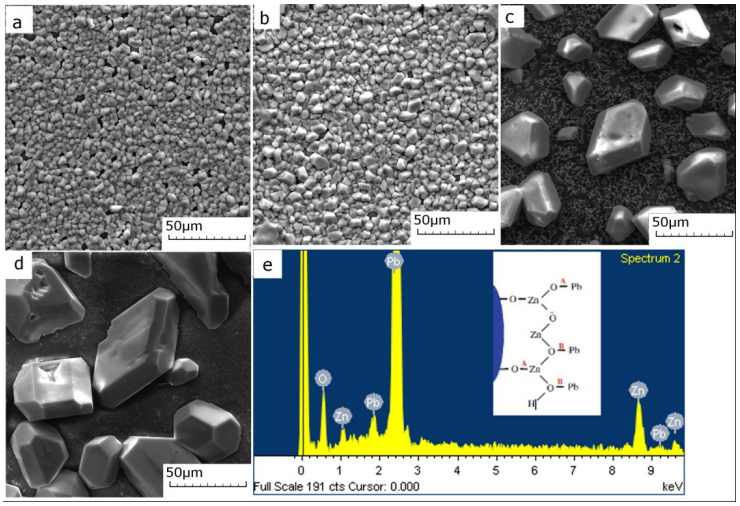

Fig. 2. SEM images of lead sediment on surface of ZnO nanotubes obtained at different concentrations of $Pb(NO_3)_2$ aqueous solution (a) 300mM/l, (b) 150 mM/l, (c)75 mM/l,(d) 30 mM/l, (e) EDS spectra of the obtained sample and schematic description of lead ion adsorption mechanism.

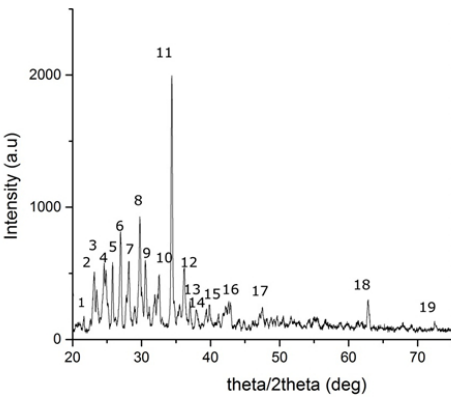

1	α-Pb_2O_3 (0,1,5)
2	$Pb_3O_2(NO_3)_2$ (2,0,0),Pb_3O_4(2,0,1), α-Pb_2O_3(1,2,3)
3	α-Pb_2O_3(2,0,-1),
4	β-Pb_2O_3(2,0,1), α-Pb_2O_3(2,1,-1) $Pb_3O_2(NO_3)_2$ (2,0,2), α-Pb_2O_3(1,2,4)
5	α-Pb_2O_3 (2,0,-3)
6	α-Pb_2O_3 (0,0,7)
7	α-Pb_2O_3 (0,1,7)
8	Pb(1,0,0), $Pb_3O_2(NO_3)_2$ (2,0,4),PbO(0,1,1)
9	Pb_3O_4(2,0,2)
10	ZnO(1,0,0) ,PbO (1,0,1)
11	ZnO(0,0,2), Pb(1,0,1), $Pb_3O_2(NO_3)_2$ (1,1,6), α-Pb_2O_3(2,3,2)
12	ZnO(1,0,1), Pb(0,0,2)
13	β-Pb_2O_3(1,2,0),Pb_3O_4(3,2,1),α-Pb_2O_3(2,2,-6)
14	Pb_3O_4(0,0,3), α-Pb_2O_3(1,4,4),PbO(0,2,0)
15	α-Pb_2O_3 (2,0,-8), $Pb_3O_2(NO_3)_2$ (2,2,1),
16	α-Pb_2O_3 (0,2,1) $Pb_3O_2(NO_3)_2$ (3,0,5), α-Pb_2O_3(2,1,9)
17	ZnO(1,0,2), $Pb_3O_2(NO_3)_2$ (0,3,1),Pb_3O_4(2,2,3), α-Pb_2O_3(4,1,1)
18	ZnO(1,0,3),Pb(1,0,3), α-Pb_2O_3(1,7,-4)
19	ZnO(0,0,4), $Pb_3O_2(NO_3)_2$ (2,3,9), Pb_3O_4(0,4,4), α-Pb_2O_3(1,8,-1)

Fig. 3. XRD pattern of ZnO sample after lead ion adsorption.

Capacity of static adsorption was determined by equation (1).

$$q_e = \frac{(C_0 - C_e)V}{m}, \quad (1)$$

where q_e is the amount of adsorbed Pb(II) (mg g^{-1}), C_0 and C_e are the initial and equilibrium concentration of Pb(II) ions in solution (mg L^{-1}), respectively, V is volume of solution (L) and m is sorbent mass (g).

Calculations show that static adsorption capacity of ZnO nanotubes and nanorods obtained under the same conditions is 611 mg/g and 256mg/g, respectively. Measurements were taken at room temperature using 300mM/l solution and immersing for 5min.

The obtained values mean that ZnO nanotubes in comparison with nanorods show better sorption properties per mass unit of sorbent for Pb^{2+} ion due to a larger effective surface and they are higher than that of ZnO nanorods and hollow microspheres as indicated in [2], [4], [10].

Optical transmittance spectra were taken with the aim to obtain the additional information about lead adsorption process on surface of ZnO nanotubes.

For this purpose, ZnO nanotube-coated glass plates were placed into a cuvette containing distilled water and the obtained spectra were accepted as a reference. Then water was replaced with 300mM/l-30mM/l $Pb(NO_3)_2$ aqueous solution and spectra were carried out repeatedly, with different time delay of 0–30 min, in order to track lead sedimentation process in time and find out differences.

As shown in Fig. 4, during the reference experiment only one absorption edge at 380 nm corresponding to pure ZnO was observed.

When water was replaced with different concentrations of lead nitrate solution, distinct differences were observed for each concentration: ZnO corresponding adsorption edge was shifted to a shorter wavelength area that indicated structural changes in ZnO due to precipitation of lead oxide and, apart from the main absorption edge corresponding to ZnO, the second absorption edge appeared and its value at 350 nm corresponded to the value specified for lead oxide by [19].

According to time differences of the obtained spectra, the adsorption process occurred rapidly: strong differences in shape of transmittance spectra were observed only for “as immersed” sample compared to the reference sample when the second absorption edge appeared immediately after immersion and the shape of spectra was constant during the entire experiment: by increasing time delay between two measurements only a change in intensity was observed, and there was no shape change. Differences in the intensity of spectra increased along with a decrease in lead nitrate concentration: at maximal 10 % concentration spectra almost had no changes in time and after 30 min immersion had a slight difference in intensity compared to spectra of “as immersed” sample.

It should be noted that at higher concentration, changes in the transmittance value compared to the reference measurement with distilled water were observed immediately without time delay when lead nitrate solution was poured (“as immersed” samples), but in case of less concentration such as 2.5 % and 1 % an increase in transmittance was not observed during “as immersed” measurement (spectra were practically the same to the reference with the only difference being the second adsorption edge) and appeared only after 15–30min of time delay.

By comparing transmittance spectra of ZnO nanotubes and nanorods (Fig. 5), it can be concluded that nanorods have a time lag according to the adsorption

process: after changing distilled water to lead nitrate solution no changes in intensity and no second adsorption edge corresponding to lead oxide are observed at first (Fig. 5a) and they appear only in 20–30 min, despite the fact that for tubes obtained under the same condition the second adsorption edge appears immediately (Fig. 5b).

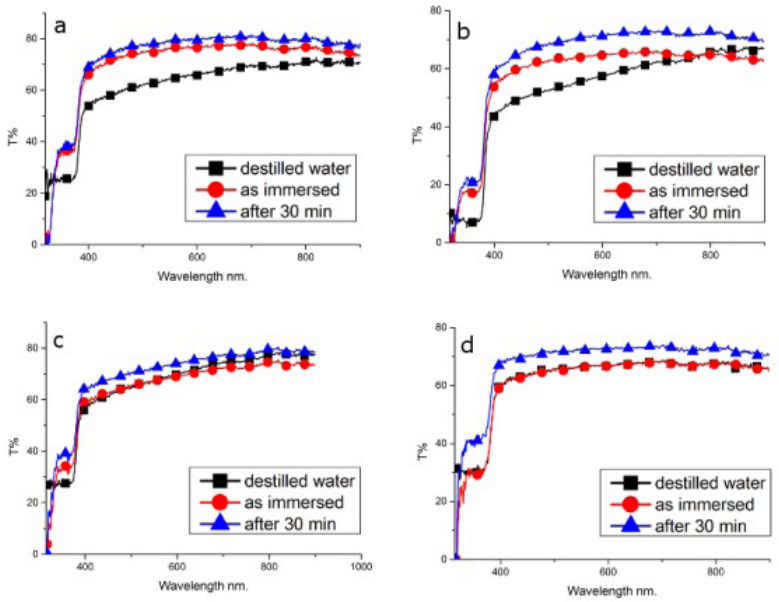

Fig. 4. Transmittance spectra of ZnO nanotubes immersed in various concentrations of $Pb(NO_3)_2$ aqueous solution. a)10 %, b) 5 %, c) 2.5 %, d)1 %.

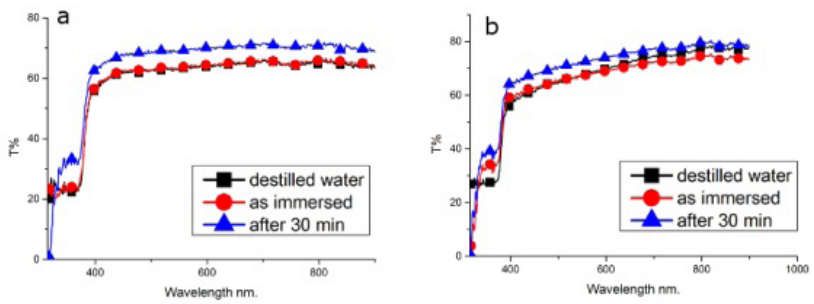

Fig. 5. Comparison of transmittance spectra of ZnO nanorods and nanotubes. Measurements were carried out using 2.5 % $Pb(NO_3)_2$ aqueous solution. a) ZnO nanorods, b) ZnO nanotubes.

4. CONCLUSIONS

In the present research, well-aligned ZnO nanotube arrays have been obtained using a hydrothermal growth method, and then they have been used as a sorbent to evaluate efficiency of sedimentation process of lead ions on ZnO surface with the aim to apply ZnO nanostructures as a sorbent for water purification from lead contaminants.

It has been determined that lead precipitates to ZnO as a blend of different kinds of lead oxides (PbO, Pb_2O_3, Pb_3O_4) and pure lead (Pb).

The experiment has shown that ZnO nanotube array demonstrates an approximately twofold higher value of static adsorption capacity (>600 mg/g) than that of ZnO nanorods grown under the same conditions.

Optical measurements have shown that ZnO nanotubes have higher responsiveness and sensibility to changes in the concentration of lead nitrate solution.

Detection of lead ions in aqueous solution can be carried out through the analysis of change in the shape of transmittance spectra: due to sedimentation process, the second absorption edge appears and ZnO adsorption edge shifts to a short wave region.

REFERENCES

1. Amin, M.T., Alazba, A.A., & Manzoor, U. (2014). A review of removal of pollutants from water/wastewater using different types of nanomaterials, *Adv. Mater.Sci. Eng.*, 1–24.DOI: http://dx.doi.org/10.1155/2014/825910.
2. Singh, S., Barick, K.C., & Bahadur, D. (2013). Functional oxide nanomaterials and nanocomposites for the removal of heavy metals and dyes. *Nanomater. Nanotechnol, 3*(20). DOI 10.5772/57237.
3. Rahman, M.M., Bahadar, K., Hadi, S., & Marwani, M. (2014). Low dimensional Ni-ZnO nanoparticles as marker of toxic lead ions for environmental remediation, *J.Ind. Eng. Chem. 20*(3), 1071–1078. DOI: 10.1016/j.jiec.2013.06.044.
4. Zolfaghari, G., Esmaili-Sari, A., Anbia, M., Younesi, H., Ghasemian, M.B. (2013). A zinc oxide-coated nanoporous carbon adsorbent for lead removal from water: optimization, equilibrium modeling, and kinetics studies. *Int. J. Environ. Sci. Technol.,* 10, 325–340. DOI: 10.1007/s13762-012-0135-6.
5. Srivastava, S., & Srivastav, Y. (2013). Removal of arsenic from waste water by using ZnO nano-materials. *J.Mater. Sci.Eng. B, 3*(8), 483–492.
6. Khan, S.B., Rahman, M.M., Marwani, H.M., Asiri A.M., & Alamry, K.A. (2013). An assessment of zinc oxide nanosheets as a selective adsorbent for cadmium. *Nanosc. Res. Lett.* 8, 377. DOI: 10.1186/1556-276X-8-377.
7. Rahman, M.M., Khan, S.B. Asiri, A.M., Marwani, H.M., & Qusti, A.H. (2013). Selective detection of toxic Pb (II) ions based on wet-chemically prepared nanosheets integrated CuO–ZnO nanocomposites, *Comp. B,* 54, 215–223. DOI:http://dx.doi.org/10.1016/j.compositesb.2013.05.018.
8. Kannadasan, N., Shanmugam, N., Sathishkumar, K., Cholan, S., Ponnguzhali, R., & Viruthagiri, G. (2015).Optical behavior and sensor activity of Pb ions incorporated ZnO nanocrystals. *Spectrochim. Acta A: Molecul. Biomolecul. Spectrosc. 143*, 179–186. DOI: http://dx.doi.org/10.1016/j.saa.2015.01.113.
9. Erdem, M., Ucar, S. Karagöz, S., & Tay, T. (2013). Removal of Lead (II) Ions from Aqueous Solutions onto Activated Carbon Derived from Waste Biomass. *Sci.World. J., 7*. DOI: http://dx.doi.org/10.1155/2013/146092.
10. Xianbiao, W., Weiping, C., Shengwen, L., Guozhong, W., Zhikun, W., & Huijun Z. (2013). ZnO hollow microspheres with exposed porous nanosheets surface: Structurally enhanced adsorption towards heavy metal ions. *Colloids and Surfaces A: Physicochem. Eng. Aspects,* 422, 199–205. DOI:http://dx.doi.org/10.1016/j.colsurfa.2013.01.031.
11. Wang, X., Guo, Y., Yang, L., Han, M., & Zhao, J. (2012). Nanomaterials as sorbents to remove heavy metal ions in wastewater treatment. *J. Environ. Anal. Toxicol. 2*(7), 154. DOI:10.4172/2161-0525.1000154.

12. Yeong, H.K., Dandu, K.V.R., and Jae, S.Y. (2013). Electrochemical synthesis of ZnO branched submicrorods on carbon fibers and their feasibility for environmental applications. *Nanoscale Research Letters, 8*, 262.
13. Krasovska, M., Gerbreders, V., Paskevics, V. Ogurcovs, A., & Mihailova, I. (2015). Obtaining a well- aligned ZnO nanotube array using the hydrothermal growth method. *Latvian J. Phys.Techn.Sci. 5*(52), 28–40. DOI: 10.1515/lpts-2015-0026.
14. Chae, K., Zhang, Q., Kim, J.S, Jeong, Y., & Cao, G. (2010). Low-temperature solution growth of ZnO nanotube arrays. *Beilstein J.Nanotechnol,* 1, 128–134. DOI:10.3762/bjnano.1.15.
15. Roza, L., Rahman, M.Y.A., Umar, A.A., & Salleh, M.M. (2015). Direct growth of oriented ZnO nanotubes by self-selective etching at lower temperature for photo-electrochemical (PEC) solar cell application. *J. All.Comp., 618*, 153–158. DOI:10.1016/j.jallcom.2014.08.113.
16. Song, Y., Xi, J., Xu S., Yang, R., Gao, Z., Hu, C., & Wang, Z. (2009). Growth of ZnO nanotube arrays and nanotube based piezoelectricnanogenerators. *J. Mater. Chem., 19*(48), 9260–9264. DOI: 10.1039/B917525C.
17. Hongqiang, W., Guanghai, L., Lichao, J., Guozhong, W., & Chunjuan, T. (2008). Controllable preferential-etching synthesis and photocatalytic activity of porous ZnO nanotubes. *J. Phys. Chem. C, 112*(31), 11738–11743. DOI: 10.1021/jp803059k.
18. Yap, Y.K. (2009). Growth mechanisms of vertically-aligned carbon, boron nitride, and zinc oxide nanotubes. *AIP Conf. Proc. 1150*, 126. DOI: 10.1063/1.3192226.
19. Alfind, A., Frit, P., Deepalakshmi, K., Prithivikumaran, N., & Jeyakumaran, N. (2014). The effect of annealing time on lead oxide thin films coated on indium tin oxide substrate. *Int. J. ChemTech Res.*, *6*(13), 5347–5352.

SVINA JONU ADSORBCIJAS PROCESU ANALĪZE UZ LABI SAKĀRTOTU ZnO NANOCAURULĻU VIRSMAS

M. Krasovska, V. Gerbreders, E. Tamanis, S.Gerbreders, A.Bulanovs

K o p s a v i l k u m s

Darba procesā izmantojot hidrotermālo metodi tika iegūtas labi sakārtotas ZnO nanostieņu un nanocauruļu kopas.

Tika izpētītas doto paraugu sorbcijas īpašības attiecībā uz svina jonu nogulsnēšanos no svina nitrātu saturoša ūdens šķīduma ar mērķi noteikt abu veidu efektivitāti izmantošanā kā sorbentu ūdens attīrīšanai no svinu saturošiem piemaisījumiem.

Ir konstatēts, ka ZnO virsma piesaista svina jonus dažādu oksīdu maisījuma veidā (PbO, Pb_2O_3, Pb_3O_4) un arī kā tīru metālu (Pb).

Eksperiments pierāda, ka nanocaurulēm piemīt ievērojami lielāka statiskās absorbcijas kapacitātes vērtība, nekā nanostieņiem (≈600 mg/g) un (≈ 256mg/g) atbilstoši. Svina jonu eksistenci var konstatēt arī spektroskopiski, analizējot ZnO nanostruktūru caurlaidības spektra izmaiņas: nogulsnēšanās procesā parādās otrā absorbcijas mala, kā arī primārā ZnO atbilstoša absorbcijas mala tiek nobīdīta īsviļņu apgabalā.

10.11.2016.

LATVIAN JOURNAL OF PHYSICS AND TECHNICAL SCIENCES
2017, N 1

DOI: 10.1515/lpts-2017-0006

PHYSICS

THE ANALYSIS OF NON-NEWTONIAN VIBRO-IMPACT PROCESSES IN TUBE CONSTRUCTIONS AND SYSTEMS WITH PARALLEL IMPACT PAIRS

V. L. Krupenin[1], J. Viba[2]

[1] A. Blagonravov Institute of Machines Science (IMASH RAN)
4 Maly Kharitonievskiy Per., Moscow, 101990, RUSSIA
e-mail: krupeninster@gmail.com
[2] Riga Technical University
1 Kalku Str., Riga, LV-1658, LATVIA
e-mail: Janis.Viba@rtu.lv

The present paper studies the problems of creation of techniques for the analysis of vibro-impact processes in systems with a large number of impact pairs. The used method of singularisation allows refusing from the ideas of the momentary impact and considering interaction hypotheses, which are more realistic than Newtonian ones. We consider the features of synchronous modes of movements of the clap type in systems with parallel impact elements as well as in tubes colliding with intermediate supports. Such modes are most dangerous in terms of the vibration wear of structural elements. The examples of calculation are given for specific designs.

Keywords: *2N-parametrical representation, calculation for tube constructions, degrees of freedoms, integral equation of nonlinear oscillations, interaction momentum, interaction time, non-momentary impact, periodic Green's function, singularisation, synchronous impact.*

1. INTRODUCTION

The problem of modelling and analysis of non-Newtonian vibro-impact systems, where the forces of shock interaction are described by threshold nonlinearities, was discussed in [1]. Apparently, V. K. Astashev was the first to consider such problems [2]. Any threshold nonlinearity represents the hypothesis of the impact interaction. Having used the hypothesis of instantaneous impact interaction, the author of [3] proposed a method of singularisation, which allowed creating approximate solutions to the problems requiring consideration of the finite duration impact. Singularisation method, developed in [4], [5], consists in the following: at interaction the concept of impact in first approximation still remains Newtonian (elastic impact),

but the obstacles are set not as fixed but "floating" depending on the time of interaction defined by the non-Newtonian impact hypothesis. Thus, it makes possible to take into account different characteristics of elastic loading during the impact of the interacting subsystems, as well as to consider more realistic models of the dispersion energy during interaction. These issues are discussed below.

2. OPERATOR EQUATION OF MOTION

We consider a periodic vibro-impact process in a mechanical system of the general type comprising N impact pairs. In the construction process, we use in some modified form the methods of time-frequency analysis of vibro-impact processes [1], [4]–[10] based on the record of the desired laws of motion using periodic Green's function of the interacting linear mechanical subsystems. As an example, we consider a linear scleronomous, stationary mechanical system with an arbitrary finite number (N_1) of degrees of freedom. For simplicity reasons, we restrict ourselves to assumption being, in general terms, insignificant that each point of the system performs a one-dimensional movement along a certain axis. Let us suppose that a family of operators of dynamic compliance of the given system $L(u,y; p)$, where u and y are its arbitrary points, is known. Each such operator associates a force applied in the point u with the displacement of the point y; $p \equiv d/dt$.

We suppose that at $N \le N_1$ points $\{u_k\}$: $L(u_k, u_k) = O(p^{-2})$ $(p\to\infty)$. This assumption means, in particular, that at points $\{u_k\}$ some bodies with mass m_k are concentrated. We assume further that each such point contains an impact pair, which is supposed to be asymmetric and unilateral for definiteness, i.e., there is an ordered set of numbers $\{\Delta_k\}$ such that $u_k \le \Delta_k$ and at $u_k = \Delta_k$ a direct and central non-Newtonian impact interaction takes place. We denote the impact force in the k-th pair as $\Phi_k(u_k;\dot{u}_k)$; we particularize the form of $\Phi_k(u_k;\dot{u}_k)$ below. It is common to set $\Phi_k(u_k;\dot{u}_k) = \Phi_{1k}(u_k) + \Phi_{2k}(u_k;\dot{u}_k)$, where $\Phi_{1k}(u_k)$ is an elastic component and $\Phi_{2k}(u_k;\dot{u}_k)$ is a dissipative one.

Assuming, finally, that periodic (with period T_0) external excitatory forces $P_h(u_h;\dot{u}_h;t)$ are applied in some selected $H \le N_1$ points $\{u_h\}$, we can write for the points u_k:

$$u_k(t)=\sum_{h=1}^{H} L(u_k, u_h;p)P_h(u_h;\dot{u}_h;t) - \sum_{n=1}^{N} L(u_k,u_n;p)\Phi_k(u_k;\dot{u}_k;s)\,. \tag{1}$$

We should also point out that similarly we can consider the case where concentrated bodies of the studied system collide among themselves [4].

Let us assume that the family $\{P_h\}$ is T-periodic. To find the T-periodic laws of motion $u_k(t)$, one can use a system of integral equations of the periodic fluctuations of Hammerstein type [4]–[7] when $k = 1,...,n$:

$$\begin{aligned} u_k(t)=&\sum_{h=1}^{H}\int_0^T \chi(u_k,u_h;t-s)P_h[u_h(s);\dot{u}_h(s);s]ds - \\ &-\sum_{n=1}^{N}\int_0^T \chi(u_k,u_n;t-s)\Phi_k[u_k(s);\dot{u}_k(s);s]ds\ . \end{aligned} \tag{2}$$

Here $\chi(u_k, u_h; t\text{-}s)$ is a periodic Green's function (PGF) corresponding to the operator $L(u_k, u_h; p)$:

$$\chi(u_k, u_h; t)=T^{-1}\sum_{q=-\infty}^{\infty}L(u_k, u_h; iq\omega t)\exp(iq\omega t)\ . \tag{3}$$

PFG properties are described in detail in [4], [6]; they represent the response of linear systems to periodic sequence of Dirac δ-functions (Dirac comb):

$$\delta^T(t)=\sum_{n=-\infty}^{\infty}\delta(t\text{-}nT)=T^{-1}\sum_{q=-\infty}^{\infty}\exp(iq\omega t). \tag{4}$$

The first term on the right side (4), thus, turns out to be the solution to the linear problem (all $\Phi_k \equiv 0$). If all the excitatory forces are symmetric and impact pairs are also symmetric, then in order to find the symmetric motion modes $u_k(t)=- u_k(t+T/2)$ of the system (1) we can use symmetrizable integral equations (2), where the integration is taken in the interval [0, T/2], while symmetric PFG-s serve as kernels:

$$\chi^*(u_k, u_h; t)=2T^{-1}\sum_{q=-\infty}^{\infty}L\{u_k, u_h;[i(2q+1)\omega t]\}\exp[i(2q+1)\omega t], \tag{5}$$

which proves to be a linear system response to a double Dirac comb:

$$\delta^{T/2}(t)=\sum_{n=-\infty}^{\infty}[\delta(t\text{-}nT)\text{ - }\delta(t\text{-}T/2\text{-}nT)=T^{-1}\sum_{q=-\infty}^{\infty}\exp[i(2q+1)\omega t]. \tag{6}$$

The representation of PFG-s is useful in their final form at intervals of periodicity (symmetry) – see [4], [6], [9] and below.

3. HYPOTHESIS OF IMPACT

In terms of collisions, we need to consider the hypothesis of an impact. We will initially assume that the impact is perfectly elastic and direct. Let us consider the so-called threshold functions from the class $\{\Phi\}_\Delta$ [1], [4], [5]. We denote the threshold as a coordinate, after passing of which the impact interaction between two bodies or a body and a fixed limiter begins. The coordinate is counted along the axis of impact. If the impact is absolutely rigid and the deformation of colliding bodies can be neglected, then the duration of the impact is zero (momentary impact).

In the event of momentary impact, a well-known Newtonian hypothesis is applied. The impact force, in this case, is written using a singular generalized function [1], [3], [4], [6]. However, if it is important to take into account either finite duration of impact force or energy losses during the interaction, one should take into account some theories of contact damping based, for example, on the material properties of the interacting bodies, and here it is necessary to abandon assumptions about the momentary nature of the interaction.

First, let us consider an elastic impact. Generally speaking, the choice of

hypothesis of impact is a problem of designation of representation of the interaction force. If an impact pair is one-sided and asymmetric as shown in Fig.1, then a responding threshold function $\Phi_l(u_k) = = \lambda\Phi_k(u_k)$ is also asymmetric. In fact, with the help of this function, the hypothesis of the impact in this pair can be determined. Here $\lambda >> 1$ is a large parameter. The class of threshold functions for a given task is defined as follows (Fig. 1):

$$\Phi_k \in \{\Phi\}_\Delta \equiv$$
$$\equiv \{\Phi_k(u_k); \Phi(u_k) = \psi_k(u_k - \Delta)\eta(u_k - \Delta), \Delta \geq 0; \psi_k(u_k - \Delta) \equiv 0; u_k \geq 0\}. \qquad (7)$$

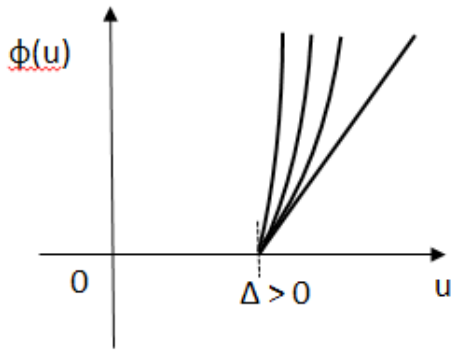

Fig. 1. One-sided and asymmetric impact pair. Φ(u) – threshold function; u – local displacement.

It is assumed that $\psi_k(u_k)$ is continuously differentiable on the entire number axis, is convex and monotonically increases at $x \geq 0$; $\eta(x)$ is a unit function.

Following the first works, this approach was later developed in the book [4], while for systems with multiple impact pairs – in [6]. We fix the hypothesis of elastic interaction in each impact pair in form (3) and consider problem (1) [(2)] using the method of singularisation.

4. THE REPRESENTATIONS OF PERIODIC MODES

We consider a conservative analogue of the system of operator equations of motion (1). For all k and h we put $P_h = \Phi_{2k} = ImL(u_n, u_q; i\omega) = 0$ for all points in the system. Then the equation of motion of a conservative system with the operator $L_0(u_k, u_n; p)$ for all k takes the form:

$$u_k = \sum_{n=1}^{N} L_0(u_k, u_n; p)[\lambda\Phi_n(u_n)],\ k = 1, \ldots, N. \qquad (8)$$

In order to find periodic modes of motion in a conservative system, we use the integral equation of nonlinear oscillations, which in this case takes the form:

$$u_k(t) = -\sum_{n=1}^{N} \int_0^T \chi(u_k, u_n; t-s)\,)\lambda \Phi_n[u_n(s)]ds \ , \ k = 1, N. \tag{9}$$

Works [1], [4] under similar assumptions show that when $\lambda \to \infty$, the solutions of equations similar to (8) transform into the solutions that meet the hypothesis of a momentary (in this case elastic) impact.

It is postulated that during the interaction in arbitrary impact pair one can neglect the effect of any forces applied in the point of the pair localization, as well as of any forces, including interaction forces applied at other points of the system.

Let us use the method of singularisation that associates a non-momentary short interaction with a momentary impact, which takes place at a "shifted time". In accordance with the method, we can approximate the forces from equation (8) as a singular generalized function. In particular, for T-periodic process under the assumption of a single interaction for the period of movement in each impact pair:

$$\lambda \Phi_n[u_n(t)] = J_{\lambda n} \delta^T(t - t_n - \tau_{\lambda n}); \quad n = 1, \ldots, N, \tag{10}$$

where t_n is a fixed moment of the beginning of interaction in the n-th impact pair (phase); furthermore, $t_{nk} \in [0, T]$; $\tau_{\lambda n} = \frac{1}{2} t_{\lambda n}$ – half time of interaction in this pair determined from the previously obtained formulas [10], [6], [11] (see also below).

Representation (9)–(10) is caused by the fact that, first, we find the modes of motion namely of periodic type in a conservative system, and, secondly, the forces of interaction, as in the case of hypothesis of momentary impact, are given by equations of motion containing singular generalized functions. Such equations of motion are called singularized. In formula (10), $J_{\lambda n}$ is a momentum of interaction in each n-th impact pair:

$$J_{\lambda n} = \left| \int_0^{t_{\lambda n}} \lambda \Phi_n[u_n(s)] \mathrm{d}s \right|, \quad k = 1, \ldots, N. \tag{11}$$

Now from (8) we obtain:

$$u_k(t) = -\sum_{n=1}^{N} J_{\lambda n} \chi_{kn}(t - t_n - \tau_{\lambda n}), \quad k = 1, \ldots, N. \tag{12}$$

Representation (12) determines the solution using $2N$ parameters that are momenta of interaction and the moments of the beginning of interaction. As in problems with momentary impact, we will call such a solution as $2N$ – parametric representation [6]. To find N unknown motion parameters, we use the terms of the beginning (or the end) of the interaction:

$$u_k(t_n) \equiv u_k(t_n + t_{\lambda n}) = \Delta_k, \quad k = 1, \ldots, N, \tag{13}$$

where Δ_k – the values of the installation clearance (preload) and

$$\Delta_k = \sum_{n=1}^{N} J_{\lambda n} \chi_{kn}(t_n + \tau_{\lambda n}); \quad k = 1, \ldots, N. \tag{14}$$

Relations (14) represent a system of N linear algebraic equations; the quantities $\tau_{\lambda n}$ will be given below. Furthermore, N conditions for quantities t_n can be obtained from the additional relations resulted from (13) and concretized hypotheses of interaction. When addressing a conservative task, it is expedient to involve consideration of symmetry. To obtain analytical design equations, it is advisable to remain within the analytical design formulas, assume for all *k:* $\Delta_k \equiv \Delta$. On the use of numerical methods in such systems, see [12].

5. PERIODIC CLAPS IN THE ELASTIC CHAIN

By a clap we mean a driving mode, in which all or a part of massive bodies move in-phase and interact synchronously, for example, with limiters. With a clap, the vibro-impact process turns out to be most intensive [8]. We consider a model system with periodic structure (Fig. 2) [8]–[10]. Let us consider an elastic model. So as not to limit generality, we assume, for simplicity, $m = c = 1$. In addition, it is natural to assume that all impact pairs act under the same hypothesis of interaction.

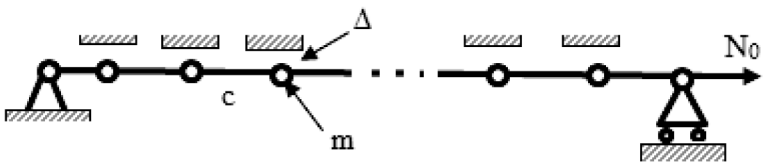

Fig. 2. Elastic model system with a periodic structure: m – local mass; Δ – gap.

Under the assumption of a conservative system, the equations of motion for k=1,...,N and boundary conditions take the form

$$\ddot{u}_{kq} + 2u_k - u_{k-1} - u_{k+1} + \lambda\Phi(u_k) = 0,\ u_0 = u_{N+1} = 0, \tag{15}$$

where $u_k \le \Delta$ and the clap, first, is assumed to be perfectly elastic (see below).

Let the system experience a clap in which all the particles take part. Then $2N$-parametric representation (12) and defining relations (13), (14), when k =1,...,N and t_n=0, describe the clap, in which the beginning of the interaction is combined with the reference point of time. PFG system in this case is determined by a series (3), which, taking into account the representation of the operators of dynamic compliance given in [4], can be written in final form on an interval of periodicity for $t \in [0, T]$:

$$\chi_{kn}(t) = \sum_{q=1}^{N} \frac{1}{N+1} \sin\left(\frac{\pi jq}{N+1}\right) \sin\left(\frac{\pi kq}{N+1} \frac{\cos[\Omega_q (t - T/2)]}{\Omega_q \sin(\frac{1}{2}\Omega_q T)}\right), \tag{16}$$

further, natural frequencies of the linear chain

$$\Omega_q = 2\sin\left[\frac{\pi q}{2(n+1)}\right]. \tag{17}$$

To obtain a finite representation for PFG $\chi_{kN}(t)$ outside the interval [0, T], we have to extend the function (16) periodically, using the condition $\chi_{kn}(t)=\chi_{kn}(t+T)$ for all $t \in \boldsymbol{R}$.

Formulas (12) and (14) contain the quantity $\tau_{\lambda n}$ which is a half of the interaction time in the n-th impact pair.

Quantities $\tau_{\lambda nj}$, generally speaking, depend on the selected hypotheses and impulse of interaction. Works [4]–[6] give the defining relations when choosing the hypothesis of interaction in form:

$$\lambda \Phi_n(x) = (x-\Delta)^{\alpha} \eta(x-\Delta) \ , \ \alpha \geq 1. \tag{18}$$

In a common case of the hypothesis of linear dependence of the interaction force in the contact zone, i.e., when in (19) $\alpha=1$, it is shown that at a fixed parameter λ and large momenta, the interaction time does not depend on the quantity of the latest and

$$\tau_{\lambda n} = \pi / 2\sqrt{\lambda}, \tag{19}$$

so, by choosing this hypothesis (18), in representation (12) for all n we can assume $\tau_{\lambda n} \equiv \tau_{\lambda} = \text{const}(J_{\lambda})$. In this case $m = 1$.

While abandoning the assumption that the momenta of interaction are large, the interaction becomes dependent but this dependence is rather weak. When $\alpha>1$ (always $\tau_{\lambda n} \equiv \tau_{\lambda} \neq \text{const}(J_{\lambda})$), for large momenta, this dependence is weak. Expressions for the parameters of singularitarian equations and representations of movement when $\alpha>1$ are not given here, as they are not used further; see [4]–[6]. Note that the interaction time $\sim \tau_{\lambda}$ can also be taken from experimental data.

6. EXAMPLE: A THREE-SPAN CHAIN

Consider a three-span chain (N=2). From (14) it follows:

$$\Delta = J_1 \chi_{11}(\tau_{\lambda}) + J_2 \chi_{12}(\tau_{\lambda}); \ \Delta = J_1 \chi_{,21}(\tau_{\lambda}) + J_2 \chi_{22}(\tau_{\lambda}). \tag{20}$$

As $\chi_{11}(\tau_{\lambda}) = \chi_{22}(\tau_{\lambda})$ and $\chi_{12}(\tau_{\lambda}) = \chi_{,21}(\tau_{\lambda})$, then $J_1 = J_2 = J$. For natural frequencies we find from (17): $\Omega_1 = 1$, $\Omega_2 = \sqrt{3}$.

The quantity of J uniquely depends on the total energy and appears to be the integral of motion. Another integral of motion is arbitrary moment of the interaction beginning [4]–[7].

Thus, from formula (14) we obtain an approximate representation of the solution (m=1):

$$u_1(t) = u_2(t) \equiv u(t) = J[\chi_{11}(t - \pi / 2\sqrt{\lambda}) + \chi_{12}(t - \pi / 2\sqrt{\lambda})]. \tag{21}$$

For example, from the first equation (18), considering (20) and (22), we find for large momenta of the interaction:

$$J=\Delta\,[\chi_{11}(\pi/2\sqrt{\lambda})+\chi_{,12}(\pi/2\sqrt{\lambda})]^{-1}. \tag{22}$$

Given PFG properties [4] inside the interval of periodicity and using the Taylor's formula we write: $\chi_{kq}(\tau_\lambda)\approx\chi_{kq,nj}(0)+\pi/4\sqrt{\lambda}$ …. Then formula (23) can be represented as follows:

$$J\approx\Delta\,[\chi_{11}(0)+\chi_{12}(0)+\pi/4\sqrt{\lambda}\,]^{-1}\approx J_0-\pi/4\sqrt{\lambda}\ , \tag{23}$$

where J_0 is the momentum of the interaction at the synchronous clap under the assumption that the hypothesis of momentary impact takes place ($\lambda\to\infty$). As

$$\begin{aligned}\chi_{11}(0)&=\chi_{22}(0)=\frac{1}{3}\left(\frac{3}{4}\operatorname{ctg}\frac{1}{2}T+\frac{\sqrt{3}}{4}\operatorname{ctg}\frac{\sqrt{3}}{2}T\right);\\ \chi_{12}(0)&=\chi_{21}(0)=\frac{1}{3}\left(\frac{3}{4}\operatorname{ctg}\frac{1}{2}T-\frac{\sqrt{3}}{4}\operatorname{ctg}\frac{\sqrt{3}}{2}T\right),\end{aligned} \tag{24}$$

in an approximation of momentary impact:

$$J_0=-2\Delta tg\frac{1}{2}T=-2\Delta tg\frac{\pi}{\varpi}\ . \tag{25}$$

This formula exactly corresponds to the representation for the traditional "impact oscillator" [4], [8]. From the condition $j\geq 0$, it follows that the claps are possible in the frequency range $1<\Omega_\lambda\leq\omega<2$, further $\Omega_\lambda=O(\lambda^{-1/2})$. Given the performed calculations, from (21) for laws of motion we obtain:

$$u(t)=\Delta\frac{\cos(t-\pi/2\sqrt{\lambda}-\pi\omega^{-1})}{\cos(\pi\omega^{-1})};\ \pi/2\sqrt{\lambda}<t<T-\pi/2\sqrt{\lambda}\ , \tag{26}$$

i.e., the motion of each body is similar to the motion of singularitariased impact oscillator. For large N the picture becomes slightly more complicated, because the claps are accompanied by unequal momenta in impact pairs.

Representation (23) appears to be most accurate for large values of the momentum, i.e., it presumes being close to the frequency $\omega=2$.

It is shown that in the case of three bodies, the momentum of the impact of the central body is somewhat larger than the momenta of the lateral bodies. In the case of four bodies, two central and two lateral ones, the momenta are pairwise equal, and so on. The dependence of $J(\omega)$ is given in [4].

7. RESONANT MODES IN A THREE-SPAN CHAIN

Let us consider the equation of motion (15), assuming that at the interaction in the contact zone the bodies are subjected to equal dissipative forces $g(\dot{u}_k)$. Let us assume, in addition, that during the motion the interacting bodies are subjected to a force of viscous friction that depends on the absolute velocities of the bodies. Then, assuming the excited oscillation to be sinusoidal with frequency ω_0, instead of (15) we obtain (in the case studied here N=2; $u_0=u_{N+1}=0$):

$$\ddot{u}_k + 2u_k - u_{k-1} - u_{k+1} + \lambda \Phi(u_k) = -g(\dot{u}_k)\eta(u_k - \Delta) - 2\varepsilon b\dot{u}_k + \varepsilon P_k \cos(\omega_0 t + \varphi_k). \quad (27)$$

Analysing the problem of finding of periodic modes of frequency ω_0 in the system (27), we restrict ourselves to in-phase resonant modes, by which we imply the motions similar to the above-mentioned periodic modes of the correspondent conservative system. Let us assume that the levels of forces of excitation and dissipation are low, so that at the resonant modes a mutual compensation of their work takes place. We see such understanding of resonance in [4]–[11], in particular.

Let us consider the basic resonance modes. The frequencies ω_0 ($1<\Omega_\lambda \le \omega_0<2$) lie in the interval of existence of simultaneous claps. Let us assume that all external effects $P_k(t)=\varepsilon P_k \cos(\omega_0 t+\varphi_k)$ are in-phase and of equal amplitudes, i.e., for all $\varphi_k=\varphi$; $P_k=P$. Let us denote the modes of the conservative system (15) at $\omega=\omega_0$ as $u^{(0)}(\omega_0; t)$. Thus, in this case for all k we approximately assume:

$$u_{kq}(t) \approx u^{(0)}(\omega_0; t) \quad (28)$$

In the studied case N=2. Therefore, the impulses of the interaction for both impact pairs are equal; at the increasing number N the form of the equation given below appears to be more complicated.

The momentum of the interaction $J^{(0)}(\omega_0)$ is given using the second relation (23) with $\omega=\omega_0$. The assumption made above about large momenta, leading to the simplification of the expression for the time of interaction, is consistent with the view of the resonant nature of the movement.

Considering that the beginning of the interaction coincides with the beginning of the zero time, we assume that the phase φ is unknown. To find the phase, we write the equation of the balance of the works of non-conservative forces for motion $\dot{u}^{(0)}(\omega_0; t)$ for the period T_0:

$$\int_0^{T_0} \{g[\dot{u}^{(0)}(t)]\eta(\dot{u}^{(0)} - \Delta) + 2\varepsilon b\dot{u}^{(0)}(t) - \varepsilon P \cos(\omega_0 t + \varphi)\}\dot{u}^{(0)}(\omega_0; t)dt = 0. \quad (29)$$

Strictly speaking, this ratio should be written for all coordinates u_k. After transformation and computing of the number of quadrature, and being given the notation introduced in equation (28), we find:

$$E_c[g; J^{(0)}(\omega_0); \tau_\lambda] + \frac{\varepsilon b}{\sin^2(\frac{1}{2}\Omega T_0)} J^{(0)}(\omega_0)\left(1 - \frac{\sin(\Omega T_0)}{\Omega T_0}\right) = \frac{2\omega_0^2 P \sin[\omega_0(\varphi + \tau_\lambda)]}{\pi(\omega_0^2 - \Omega^2)}. \quad (30)$$

Here $E_c[g; J^{(0)}(\omega_0); \tau_\lambda]$ is the energy loss during contact. It should be noted that as the force $\Phi_2(u_k; \dot{u}_k)$ acts in a short time $\tau_\lambda \sim \lambda^{-1/2}$, in order to account this force in the present approach, we should consider $\Phi_2 \sim 1$. From equation (30) we define

two quantities of phase, one of which corresponds to the unstable mode as well as to the condition of the resonant mode existence: $|\sin[\omega(\varphi+\tau_\lambda)]\le 1|$. Thus, we have:

$$\left|\frac{\pi(\omega^2-\Omega^2)}{2P\omega_0^2}[E_c[g;J^{(0)}(\omega_0);\tau_\lambda]+\frac{\varepsilon b}{\sin^2(\frac{1}{2}\Omega T_0)}J^{(0)}(\omega_0)(1-\frac{\sin(\Omega T_0)}{\Omega T_0})]\right|\le 1.$$

The driving modes of the clap type were registered experimentally and studied quite extensively [4], [8]–[11].

8. CALCULATION OF PIPE VIBRO-IMPACT SYSTEM

In heat exchanger pipes of power equipment, wear of tubes occurs due to continuous collisions with elements of spacer grids [13]. Periodic (in particular, sine wave) excitation of pipe vibration is conditioned by the unsteadiness of fluid flow, impinging on the pipe with velocity v. Let us consider the system presented in Fig. 3. A simply supported rod simulating a pipe at oscillations in the plane (u, x) can interact with $\boldsymbol{n}$ flat extended with limiters h_j (j=1, 2, … , N). Parameters of the system are: rod length l >> hj; tensile force N_0, the rigidity and linear mass of the rod K and ρ, respectively; adjusting clearances $\Delta_{j1,2}$; coordinates of the beginning and the end of the limiters x_j and x_j+h_j, respectively. We consider a symmetric system and assume: $\Delta_{j1}=\Delta_{j2}\equiv\Delta$. In order to take into account the finite duration of impact, let us assume that the interaction occurs in elastic-dissipative buffers equipped with a dry friction damper, i.e., the interaction corresponds to some hysteresis characteristic.

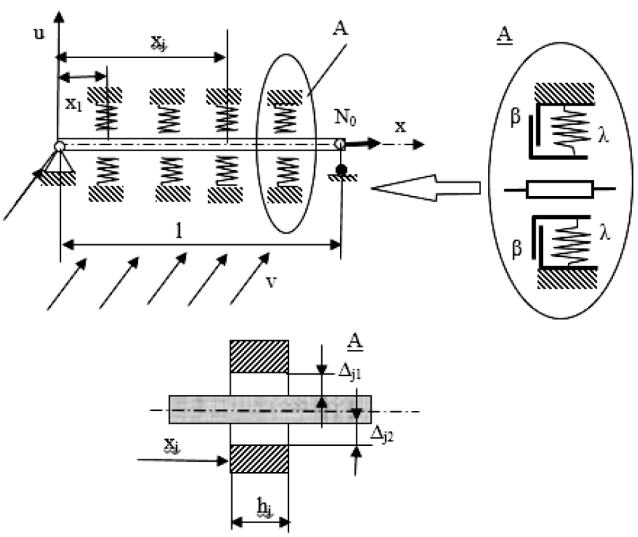

Fig. 3. A simply supported rod simulating a pipe at oscillations in the plane (u, x).

Assuming that small dissipation is taken into account only at interaction and in the case the level of excitation is low, we write the equation of motion under the assumption that the rod is modelled by the Bernoulli beam

$$\rho u_{tt}+Ku_{4x}-N_0u_{xx}+\lambda\Phi^*(u)=\varepsilon P(x,t)-\beta\,\mathrm{sign}u_t[\eta(u-\Delta)-\eta(u+\Delta)]. \qquad (31)$$

Let the boundary conditions correspond to simple support: $u(0, t)=$

$= u(l, t)= u_{xx}(0, t)= u_{xx}(l, t)=0$; $\varepsilon=O(\lambda^{-1/2})$ – a small parameter; quantities $h_{j,}\sim \varepsilon$; b~1; T_0 – a periodic external excitement.

Let us suppose that the symmetric elastic force of the interaction is described by a function from the class of symmetric threshold functions: $\Phi^* \in \{\Phi^*\}_{\Delta}$ - [4].

At first, let us assume that $\varepsilon=\beta=0$ and consider a conservative model. Let us assume that in the system free periodic fluctuations settle. Then, in definitory relations in Section 4 and below we turn to the density of the parameters and record the density of the elastic impact forces acting at $x\in[x_k, x_k+h_k]$ through the density of the impact momentum $I(x)$, the phase distribution $\varphi(x)$ and the distribution of the interaction time $\tau_\lambda(x)$ [15]

$$\lambda\Phi^*[u(x,t)]=\sum_{k=1}^{N} I(x)\delta^{T/2}[t-\varphi(x)-\tau_\lambda(x)][\eta(x_k)-\eta(x_k+h_k)], \qquad (32)$$

where a double Dirac comb $\delta^{T/2}$ is given in (6). Therefore, for the searched displacement field an integral representation, analogous to the 2N-parametric representation (12) [7], holds:

$$u(x,T)=\ ,\ u(x,t)=-\sum_{n=1}^{N}\int_{x_k}^{x_k+h_k}\chi^*[x,z,t-\varphi_k(z)-\tau_{\lambda k}(z)]I_k(z)dz\,, \qquad (33)$$

where $\varphi_k(z),\tau_{\lambda k}(z),I_k(z)$ are the corresponding distributions in k-th impact element. Symmetric PFG for the beam for $0\le t\le T/2$ has the form [4], [5]:

$$\chi^*(x,z,t)=$$
$$=\frac{1}{\rho l}\sum_{n=1}^{\infty}[\Omega_n\cos(\tfrac{1}{4}\Omega_n T)]^{-1}\sin(\pi n x l^{-1})\sin(\pi n z l^{-1})\sin[\Omega_n(t-\tfrac{1}{4}T)]. \qquad (34)$$

It also corresponds to the operator of dynamic compliance, which acts from point z to point x. The natural frequencies of the linear system are $\Omega_n=(\pi^4 n^4 K\rho^{-1}l^{-4}+\pi^2 n^2 N_0\rho^{-1}l^{-2})^{1/2}$. Outside the interval [0, T/2], function (34) is extended on the whole axis in terms of frequency, based on conditions of symmetry.

We will use the fact that the values h_k are small and the dynamic processes in the impact element itself have little influence on the settling regime. Furthermore, the interaction time, obviously, in all impact elements can be taken constant: $\tau_{\lambda k}(z)\approx\tau_\lambda$=const($x$; k) and instead of (33) we can switch to 2n-parametric representation in the form

$$u(x,t)=-\sum_{k=1}^{N}J_{\lambda k}\bar{\chi}^*(x,x_k;h_k;t-\varphi_k-\tau_\lambda)dz\ ;\ J_{\lambda k}=\int_{x_k}^{x_k+h_k}I_k(z)dz=\text{const}(x), \qquad (35)$$

where $J_{\lambda k}$ – the full momenta in the k-th element.

Representation (35) also contains PFG $\bar{\chi}^*$ being averaged over the small length of the impact element:

$$\overline{\chi}^*(x,x_k;h_k;t)=h_k^{-1}\int_{x_k}^{x_k+h_k}\chi^*(x,z,t)dz=$$

$$=-\frac{2}{\pi\rho h_k}\sum_{n=1}^{\infty}\frac{\sin(\pi nxl^{-1})\sin[\pi n(x+\frac{1}{2}h_k)l^{-1}]\sin(\frac{1}{2}\pi nh_k l^{-1})\sin[\Omega_n(t-\frac{1}{4}T)]}{n\Omega_n\cos(\frac{1}{4}\Omega_n T)}.$$

Representation (35) is quite similar to (12). It implies that the mass of the reduced point contacting body $m_k=\rho h_k$., while the momenta J_k can be found from the system that follows from representation (35) and from the additional conditions, such as conditions of in-phase beginning of the interactions in all impact pairs of shock or other allowable additional conditions. For in-phase motions, we obtain (compare with (14))

$$\Delta_j=-\sum_{k=1}^{N}J_{\lambda n}\overline{\chi}^*(x_j,x_k;h_k;\tau_{\lambda k})\ ;\ \ j=1,\ldots,N. \tag{36}$$

Now, assuming that during the implementation of resonant condition the mode of movement approximately corresponds to a motion in a conservative system, we find the condition of existence of resonant modes based on the principle of energy balance, whereby the works of non-conservative forces are balanced on periodic motion.

In the conservative case, period T is a function of $J_{\lambda n}$ (n= 1,.., N). Further, when examining single-frequency resonant modes, we assume that the period of the exciting effect is among the possible periods of oscillation of a conservative system $T_0=T$.

It should also be noted that in the practical use of singularized representations of type (35), we can use the estimated quantities obtained empirically and do not resort to calculations arising from the representation of power $\lambda\Phi^*[u(x,t)]$, on the basis of which the values of $\tau_{\lambda k}$ should be calculated.

9. A THREE-SPAN TUBE

Let us consider a three-span tube (N=2) modelled through Bernoulli beams.

Let us assume that $h_1=h_2\equiv h$; $\Delta_1=\Delta_2\equiv\Delta$; $x_2=l-x_1-h$. Solving system (24) and denoting the frequency of free oscillations, from system of equations (35) we find: $J_{\lambda 1}=J_{\lambda 2}\equiv J_\lambda$, where:

$$J_\lambda=$$

$$=\frac{1}{4}\pi\rho\Delta h\left\{\sum_{j=1}^{\infty}\frac{\sin[\rho(2j-1)x_1l^{-1}]\sin[\frac{1}{2}\pi(2j-1)hl^{-1}]\sin[\pi(2j-1)l^{-1}(x_1+\frac{h}{2})]}{(2j-1)\Omega_{2j-1}\cos(\frac{1}{2}\Omega_{2j-1}\pi\omega)[\sin\Omega_{2j-1}(\tau_\lambda-\frac{\pi}{2\omega})]^{-1}}\right\}^{-1}, \tag{37}$$

moreover, this entry holds only when $\tau_\lambda\in[0,\ \pi\omega^{-1}]$. Formula (37) together with (35) describes the claps with alternate interaction with the limiters in a conservative

system. Equating to zero brace (27), it is possible to find the frequency corresponding to the infinite pulses, i.e., the frequencies of maximum vibration wear.

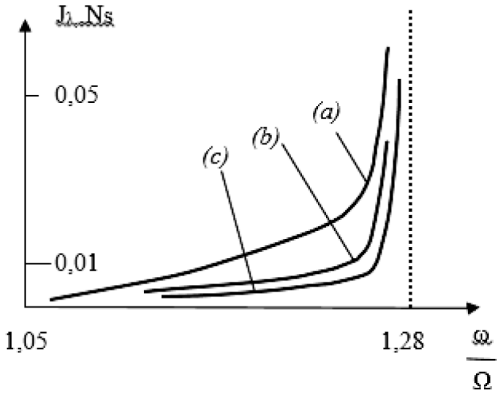

Fig. 4. Results of experimentally observed claps. Curves (*a*), (*b*) and (*c*) correspond to the cases x_1=0.7, 0.85 and 1, respectively.

Let us perform calculations using the following geometrical and physical characteristics of round tube [15]: the outer and inner diameters D=16.10^{-3} and d= 13.10^{-3} m, respectively, Young's modulus E=2·10^{11} N·м$^{-2}$, whence it follows that K=1/64πE(D^4-d^4) = 363 N·м$^{-2}$; tube length l=3 м, ρ =1.1 kG/м, N_0=4·10^{3}H, h=10^{-2}м, τ_λ =5 10^{-4}c.

The frequency zones, where the modes of motion of clap type may exist formally, are defined by the condition $J_\lambda \geq 0$. In order to find their boundaries, it is necessary to determine the frequencies at which J_λ=0 и $J_\lambda \to \infty$.

Numerical calculations reveal that one such zone exists on the right of the first natural frequency of the linear system and occupies the interval [$1.05\,\Omega_1$,$1.28\,\Omega_1$]. The calculations took account of 22 terms of the series (37). Verification of convergence was carried out numerically. Along with the specified zone, the others were identified, which turned out to be very narrow. Consideration of them in this case makes no practical sense. The observation made is in agreement with the experiment [10], [11].

We restrict our consideration to experimentally observed claps – the modes, settling to the right of the first natural frequency of the linear system. This makes possible to obtain the dependences shown in Fig. 4 (curves (*a*), (*b*) and (*c*) correspond to the cases x_1=0.7, 0.85 and 1, respectively).

Let $P(x,t) = P_1 \sin(\pi x l^{-1})\cos(\omega_0 t + \varphi)$ in equation (31). We consider the forced resonant oscillations of the synchronous type, which can only be carried out in case the frequency ω_0 belongs to the interval of natural frequencies [$1.05\,\Omega_1$, $1.28\,\Omega_1$]. We describe the movement through (35)–(37), (39), assuming, as noted above, that the studied regime is close to the regime of free vibrations $u^{(0}$ and ω_0=ω: $u(x,\ t)\approx u^{(0)}(\ J_\lambda\ ;x,\ \mathrm{t})+\ldots$, where the momentum J_λ is given by formula (37).

Aligning the impact with the zero time, we assume that the phase φ is unknown. To find it, we will use the principle of energy balance [see (31)], which in this case can be written for the half-period:

$$\int_0^l \int_0^{T/2} P_1 \sin(\pi x l^{-1}) \cos(\omega_0 t + \varphi)\, u_t^{(0)}(x, t - \tau_\lambda)\, dt =$$

$$= \int_0^l \int_0^{T/2} \beta \operatorname{sign} u_t^{(0)} [\eta(u^{(0)} - \Delta) - \eta(u^{(0)} + \Delta)] u_t^{(0)}(x, t - \tau_\lambda)\, dt, \tag{38}$$

where the left part of the equation contains the work of external source force on the motion $u^{(0)}(x, t)$ ($T=T_0$); with the expression for energy loss in the interaction [see (32)] being in the right part. Equation (38), given the correlations, enables us to obtain the condition of the existence of the resonant mode ($|\sin(\varphi + \tau_\lambda)| \le 1$):

$$P_1 \ge \left| \frac{E_c[\beta; J^{(0)}(\omega_0); \tau_\lambda; h; x_1] \pi (\Omega_1^2 - \omega^2 + \alpha)}{4 l \omega \sin(\pi h / 2l) \sin[\pi / l\, (x_1 + 0{,}5h)]} \right| ; \quad \alpha = O(\lambda^{-1/2}).$$

Here the incoming quantity $E_c[\beta; J^{(0)}(\omega_0); \tau_\lambda; h; x_1]$ in accordance with the structure of the right side of (38) determines the energy loss during the interaction. We similarly analyse an asymmetric case as well as other types of movement settling in such systems.

An overview of the issues discussed here is available in [14], [15].

ACKNOWLEDGEMENTS

The authors are grateful to V.K Astashev and M. G. Zhizhchenko for valuable comments.

The present research has been supported by the Russian Science Foundation under grant No. 15-19-30026.

REFERENCES

1. Krupenin, V.L. (1983). Vibration of the systems with large threshold elastic forces. *Mechanics of Solids, 4,* 76–84.
2. Astashev, V. K. (1965). *Periodic Motion of an Elastic Rod with Limiters. The Dynamics of Machines with Given the Elasticity and Masses Variability*. Moscow: Nauka.
3. Krupenin, V.L (1984). Calculation of mechanisms with threshold nonlinearities by a singularisation method. *Mashinovedenie, 1,* 6–12. (In Russian).
4. Babitsky, V.I., & Krupenin, V.L. (2001). *Vibration of Strongly Nonlinear Discontinuous Systems*. Berlin: Springer-Verlag.
5. Krupenin, V.L (2014). Vibroimpulsive processes in the family of elastic systems with boundary elements interacting through non-Newtonian impacts. *Journal of Machinery Manufacture and Reliability, 43*(4). 261–269. DOI: 10.3103/S1052618814040098.
6. Krupenin, V.L (2010). The representation of periodic vibration–impact processes via pulse–phase motion parameters. *Journal of Machinery Manufacture and Reliabil*ity, *39*(1), 28–34. DOI: 10.3103/S1052618810010048.

7. Krupenin, V.L. (2006). Calculation of vibration processes in two-dimensional lattices. *Journal of Machinery Manufacture and Reliability*, *4*, 26–34.
8. Astashev, V.K., & Krupenin, V.L. (1998). Waves in distributed and discrete vibroimpact systems and in strongly non-linear mediums. *Journal of Machinery Manufacture and Reliability*, *5*, 13–30.
9. Krupenin, V.L. (1998). Vibro-impact processes in systems with large number impact pairs and distributed impact elements. In *Dynamics of Vibro-Impact Systems. Euromech Colloquium 386*, 15–18 September 1998. England: Loughborough University.
10. Babitsky, V.I., Krupenin, V.L., & Veprik, A.M. (1988). Vibroimpact phenomena due to limited oscillations of one-dimensional elasto-connected particles. *Dokl. AN USSR* (*Proc. USSR Academy of Sciences*), *3*(3), 562–566.
11. Astashev, V.K., Krupenin, V.L., & Tresvyatskii, A.H. (1996). Experimental study of impacts synchronization in distributed systems with a variable number of impacts. *Journal of Machinery Manufacture and Reliability*, *2*, 96–101.
12. Viba, J., & Lavendelis, E. (2006). Algorithm of synthesis of strongly non-linear mechanical systems. In *Industrial Engineering - Innovation as Competitive Edge for SME*, 22 April 2006 (pp. 95–98). Tallinn, Estonia.
13. Krupenin, V.L. (2011). Representation of vibro-impact processes by physical parameters defining the movement "momentum – phase", Part II: Calculation of beam and tubular structures. *Bulletin of Scientific and Technological Development, 10*(50), 25–30.
14. Ibrahim, R.A. (2009). *Vibro-Impact Dynamics*. Berlin: Springer-Verlag.
15. Luo, A.C.J., & Guo, Y. (2013). *Vibro-Impact Dynamics*. Chichester, West Sussex, UK: A John Wiley & Sons, Ltd.

NE ŅŪTONA VIBROTRIECIENA PROCESU ANALĪZE CAURUĻU KONSTRUKCIJĀS UN PARALĒLU TRIECIENA PĀRU SISTĒMĀS

V. L. Krupenin, J. A. Vība

K o p s a v i l k u m s

Šajā rakstā ir izpētīta iespēja radīt jaunu teoriju tādu vibro trieciena sistēmu analīzē, kurās ir liels skaits sadursmju pāru.

Izmantotā metode (ar singularitāti) atļauj atteikties no idejas par īslaicīgu objektu sadursmi un izvērtēt tam nolūkam jaunu mijiedarbības hipotēzi, kas ir tuvāka īstenībai, nekā Ņūtona metode. Rakstā izmantotās funkcijas apraksta sinhronas sadursmes kustības "plaukšķināšanas" veidā sistēmās ar paralēliem trieciena pāriem, kā arī caurules sadursmēs ar starpposmu balstiem. Šādi sadursmju režīmi no vibrācijām ir visbīstamākie konstrukciju elementos to nodilumu ziņā. Doti aprēķināšanas piemēri no reālajām konstrukcijām.

23.08.2016.

LATVIAN JOURNAL OF PHYSICS AND TECHNICAL SCIENCES
2017, N 1

DOI: 10.1515/lpts-2017-0007

NANOINDENTATION RESPONSE ANALYSIS OF THIN FILM SUBSTRATES-I: STRAIN GRADIENT-DIVERGENCE APPROACH

U. Kanders[1], K. Kanders[2]

[1]Institute of Mechanical Engineering,
Riga Technical University,
6 Ezermalas Str., LV-1006, Riga, LATVIA
uldis.kanders@gmail.com
[2]Institute of Neuroinformatics, University & ETH of Zurich
190 Winterthurerstr., CH-8057 Zurich, SWITZERLAND
kkanders@ini.phys.ethz.ch

Nanoindentation is a widely-used method for sensitive exploration of the mechanical properties of micromechanical systems. We derive a simple empirical analysis technique to extract stress-strain field (SSF) gradient and divergence representations from nanoindentation data sets. Using this approach, local SSF gradients and structural heterogeneities can be discovered to obtain more detail about the sample's microstructure, thus enhancing the analytic capacity of the nanoindentation technique. We demonstrate the application of the SSF gradient-divergence analysis approach to nanoindentation measurements of bulk silicon.

Keywords: *elastic-plastic deformation, nanoindentation, strain gradient plasticity, stress-strain field, true hardness, true elastic modulus*.

1. INTRODUCTION

Nanoindentation is a powerful experimental technique to characterise the mechanical properties of small volume samples, such as thin films and coatings, subsurface layers of bulk solids or biological materials such as bone, tooth enamel and even viruses [1]–[5]. The measurement usually has high variability at shallow penetration depths. Consequently, the material hardness and elastic modulus are commonly calculated from data averaged over around ten or more single indentation tests at depths exceeding at least 200–300 nm. Preferably the measured variable has then approached some stable steady state value that corresponds to the so-called material bulk property, often measured by the micro- or macro-indentation techniques. However, there are also situations when a steady state nanoindentation response at increasing penetration depth cannot be generally achieved or expected. For example,

it is not always possible to observe a stationary plateau in the nanoindentation measurement of hardness or elastic modulus in thin film samples when a strong reverse indentation size effect is present [6], [7] or when the sample substrate is influencing the experiment [8], [9]. Similarly, the subsurface layer of bulk solids is usually highly heterogeneous, which might preclude the apparent hardness and/or elastic modulus to approach a stationary value [3].

In this study, we derived a simple empirical approach to extract the local stress-strain field (SSF) gradient and divergence representations from the nanoindentation experiment dataset. The strain-gradient representations, in principle, facilitate the discovery of weak structural heterogeneities, indicating, for example, interfaces between mechanically distinct local microzones within the near surface region or work hardening and softening processes induced underneath the indenter. Furthermore, the SSF gradient representations allow defining an analytic criterion for determining the values of true hardness and true elastic modulus. We show the strain gradient-divergence analysis results of the nanoindentation response of a bulk solid silicon sample. Further application to bulk samples of various thin film substrates, such as different types of bearing and tooling steels as well as fused silica, is presented in the second part of the present research [10].

2. METHODS

2.1. Derivation of the Stress-Strain Field Gradient and Divergence Representations

In the nanoindentation experiment, each new indentation increment causes a mechanical shock that generates an elastic-plastic deformation wave, which propagates throughout the sample and fades when the system is relaxed. As a result, a stress-strain tensor field of restoring forces is induced periodically in the sample. In this section, we propose that useful information about the SSF can be extracted from the nanoindentation measurement, namely the representations of SSF gradient and divergence. The analysis technique derived below builds upon the strain gradient plasticity theory where the stress-strain relationship at any given point is considered in the context of deformation events in the long range vicinity of that point [11], [12].

In the expanding cavity model, a heavily deformed hydrostatic core encases the indenter tip as deep and wide as the contact radius, a_c. The hydrostatic core is surrounded by superimposed hemispherical plastic and elastic deformation zones [1], [13]. The contact radius differs from penetration depth, h, by a constant factor, e.g., about 3 times ($a_c \approx 2.79h$) in the case of the sharp Berkovich indenter. However, when using logarithmic coordinates instead of linear ones for the penetration depth, the choice between $\log(h)$ or $\log(a_c)$ only shifts the function plot along h-axis and does not change its form. This reason and the fact that the peak pressure between the core and the plastic deformation zone is quite diffuse allows us to simplify the analysis of the SSF and use h as an independent variable instead of a_c. The hydrostatic core is considered an incompressible, homogeneous extension of the indenter tip that transduces the applied test load, $P(h)$, into the SSF. The indented system resists to further elastic-plastic deformation and compensates the applied test load

according to Newton's third law. There is no such probe to measure directly the SSF components at each point $R(x,y,z \geq h)$ throughout the sample during a nanoindentation experiment, but one can measure the integrated echo of the SSF on the interface between the core and the plastic deformation zone $R(z = h)$ as the restoring force $F(h) = -P(h)$, or the total stress $\sigma_t(h) = F(h)/(2\pi h^2)$. The force field in the X-Y plane at each $z=h$ here and thereafter is assumed to be central symmetric. Therefore, all the restoring force components F_{xy} in the infinite X-Y plane compensate each other resulting in zero value. Thus, the only $F_z=F(h)$ component resists to loading force $P(h)$ exerted by the indenter. Note that total stress $\sigma_t(h)$ can be interpreted as the potential deformation energy density function of SSF. This allows us to introduce a generalized quantity, the SSF potential function $U(h)$ that is proportionally related to the stored potential deformation energy. Application of the nabla operator to $U(h)$ creates a gradient field $\nabla U(h)$. Strong gradient of the SSF at a point $R(x,y,z = h)$ is evidence that the indented system is highly heterogeneous in a short-range vicinity of this point, whereas a weak or zero gradient is a good sign that the system is homogeneous even in a long-range vicinity. We define the normalized gradient of the generalized potential function $U(h)$ as

$$U'(h) \equiv \frac{h}{U(h)} \nabla U(h) \tag{1}$$

The gradient $U'(h)$ is a very simplified force vector field (here and thereafter a vector sign is omitted due to simplicity), which represents to some extent the much more complex actual stress-strain tensor field beneath the loaded indenter. In turn, we define the SSF divergence as the divergence of the $U'(h)$ vector field by

$$U''(h) \equiv \nabla U'(h). \tag{2}$$

Divergence is closely related to stress-strain field flux density – the amount of stress-strain flux entering or leaving a given point $R(x,y,z = h)$. $U''(h)$ tells us at which h values the interface between the hydrostatic core and the plastic deformation zone acts as a stress-strain flux source or sink. It is easy to see that positive divergence means that the interface acts as a stress-strain flux source resulting in strain hardening effect, whereas negative divergence means that the interface acts as a stress-strain flux sink resulting in strain softening effect.

The total stress, $\sigma_t(h)$, can be broken down into elastic, $\sigma_e(h)$, and plastic, $\sigma_p(h)$, components, and each of these can be further separated into normal and shear stresses. Therefore, we can describe the total stress or the total potential strain energy density of the SSF as a superposition of the elastic normal, $\sigma_{en}(h)$, the elastic shear, $\sigma_{e\tau}(h)$, the plastic normal, $\sigma_{pn}(h)$, the plastic shear, $\sigma_{p\tau}(h)$, stress components. It remains to be shown how to link these stress components to the appropriate experimental datasets obtained during a nanoindentation experiment. Knowing the area of the interface between the hydrostatic core and the plastic deformation zone, one can calculate the average total stress:

$$\sigma_t(h) = \frac{F(h)}{2\pi h^2} = \frac{-P(h)}{2\pi h^2} \Rightarrow \sigma_t(h) \propto \frac{-P(h)}{h^2} \tag{3}$$

We assume that the elastic and plastic stress fields are superimposed and have a joint interface with the core [14]. The total elastic stress, $\sigma_e(h)$, can be evaluated using the harmonic contact stiffness, $S(h)$, experimental dataset:

$$\sigma_e(h) = \frac{S(h)h}{2\pi h^2} = \frac{S(h)}{2\pi h} \Rightarrow \sigma_e(h) \propto \frac{S(h)}{h} \tag{4}$$

Elastic normal stress component is represented by the well-known relationship containing elastic modulus, $E(h)$: $\sigma_{en}(h) = E(h)\varepsilon_{en}$, where ε_{en} is the elastic normal strain. In the nanoindentation experiment, the increment δh is changed progressively so that the incremental strain, $\varepsilon_{en} = \delta h/h$, is usually kept almost constant. Step by step indentation with a constant incremental strain has the advantage of logarithmically scaling the data density so that there are equal amounts of data at low and high loads. Therefore, we can treat the incremental strain as a constant variable and simplify to

$$\sigma_{en}(h) \propto E(h). \tag{5}$$

The total plastic stress component can be represented by hardness, $H(h)$:

$$\sigma_p(h) \propto H(h). \tag{6}$$

Using the definition of SSF gradient from Eq. 1, we derived the specialised elastic-plastic strain gradients from Eqs. 3–6:

$$\begin{aligned} P'(h) &\equiv \frac{h}{P(h)}\frac{dP(h)}{dh} - 2 \\ S'(h) &\equiv \frac{h}{S(h)}\frac{dS(h)}{dh} - 1 \\ E'(h) &\equiv \frac{h}{E(h)}\frac{dE(h)}{dh} \\ H'(h) &\equiv \frac{h}{H(h)}\frac{dH(h)}{dh} \end{aligned} \tag{7}$$

where $P'(h)$ represents total strain gradient, $S'(h)$ represents elastic total strain gradient, $E'(h)$ represents elastic normal strain gradient, and $H'(h)$ represents plastic total strain gradient induced beneath the indenter. In the rest of the text, we will refer to these functions as the corresponding strain gradients instead of strain gradient representations because they differ by a constant factor only. In an analogous way, we also derive the specialised total, $P''(h)$, elastic total, $S''(h)$, elastic normal, $E''(h)$, and plastic total, $H''(h)$ divergences using the definition in Eq. 2:

$$\begin{aligned} P''(h) &\equiv \nabla P'(h), \\ S''(h) &\equiv \nabla S'(h), \\ E''(h) &\equiv \nabla E'(h), \\ H''(h) &\equiv \nabla H'(h). \end{aligned} \tag{8}$$

In practice, we estimated the gradient and divergence representations by calculating the analytic derivative of a polynomial fit to the measurement data and gradient representation, respectively. The fit was applied to a sliding window of $2m+1$ points. Results with 1st (i.e., linear) and 2nd order fits were already found to be satisfactory, with m = 8, 9 or 10 providing the optimal window lengths indicated by robust accuracy of the fits (generally, R-squared value about 0.9 at shallow and greater than 0.99 at deeper indenter penetration depths). The differences between the linear and 2nd order fit were less than 2 % of peak amplitude at very shallow penetration depths (h < 32 nm). In the present paper, we present the results obtained using a linear fit with m=8. The exact length of the window did not affect the results strongly.

2.2 Experimental Details

The instrumented depth sensing nanoindentation experiments were performed on silicon substrates Si(100). The sample (20x20x0.381 mm^3) was cut off from silicon wafer. Surface roughness parameter RMS of the sample was lower than 1 nm.

G200 Nano Indenter (Agilent, USA) with a sharp Berkovich diamond indenter (tip radius < 20 nm) was used. Measurements were made in the continuous stiffness measurement (CSM) mode [15] and in the BASIC mode at different values of the maximum load. The load capability of the Nano Indenter G200 can reach up to 600 mN with the standard option. The hardness and elastic modulus of the samples were calculated by the MTS TestWorks 4 software using Oliver-Pharr method [16].

3. RESULTS AND DISCUSSION

We performed nanoindentation experiments on different bulk samples often used as substrates for thin film coatings: faceted and polished tooling and bearing steel samples, glass and fused silica slides, and silicon wafers. Here, we give a brief demonstration of the indentation response analysis from the Si(100). Perfectly smooth Si(100) sample was chosen as a material with single crystal structure and well-known mechanical properties to validate the strain gradient-divergence approach developed above. Further results on the steel samples and fused silica, as well as a quantitative treatment of the oscillations are provided in the second part of the present research [10].

3.1 SSF Gradient and Divergence in Bulk Silicon

Traditionally in the nanoindentation analysis, the measurements of several single indentation tests are averaged out to estimate the mechanical properties of the material. Usually this is performed automatically by the software of the nanoindentation apparatus. However, at shallow penetration depths the averaged estimations commonly have a rather high variability (standard deviation), thus precluding the observations of specific peculiarities of the sample subsurface layer. Therefore, the analysis of single indentation test datasets is necessary before any automatic data averaging procedure. We carried out 8 single indentation tests on the crystalline Si(100)

sample, which we first analysed individually and then we applied the analysis to the averaged measurements as well (we observed that as little as 6 tests had already been sufficient to reliably calculate average material mechanical properties such as hardness, elastic modulus, storage modulus, loss modulus and complex modulus among others). Figure 1(a) shows a typical example of a single measurement in the CSM mode when hardness, H, and elastic modulus, E, were measured as a function of indentation depth, h, continuously along the characteristic of load-displacement, P-h. The relatively smooth P-h curve is contrasted with the corresponding total SSF gradient, P'-h, curve, which was derived using the approach introduced in Methods Section. The analysis revealed quasi-regular oscillations of the SSF gradient that could be observed already starting from 16 nm penetration depth. Initial fluctuations can also be observed for $h < 16$ nm, which were, however, interrupted by nanoindentation induced phase transformation [17], [18] when the indenter reached penetration depths of 13–15 nm. This clearly visible breach in the P'-h curve oscillations would be difficult to discover in the load-displacement curve. Phase transition at 13-15 nm in silicon is most likely related to structural changes from the cubic diamond structure of silicon (Si-I) to its amorphous metallic phase (Si-II) under small indentation load. This (Si-I)|(Si-II) phase transformation manifested by the P'-h curves was present in all the single indentation tests of silicon that we performed. The oscillations of SSF divergence, P''-h, also convincingly revealed this (Si-I)|(Si-II) phase transformation (Fig. 1(b)). The non-monotonic behaviour due to complicated plastic deformation events underneath the indenter is also manifested by distinct superstructure of the moving average trendline of the P'-h curve (not shown). Depending on maximum load and loading-unloading rate parameters one can observe complicated structural changes in cubic Si(100) [17], [18], beginning with the single diamond crystal structure (Si-I), amorphous metallic phase (Si-II), polycrystalline phase (Si-III) and ending with a mixed structure of nanocrystalline phase (Si-XII) encaged by amorphous a-Si phase.

The moving average trendline of the SSF gradient, P'-h, curve allows dividing the displacement h-axis into several intervals such as 2–13 nm, 16–38 nm, 40–58 nm, 60–86 nm, 116–288 nm and 500–900 nm, which could be attributed to some extent to the above-mentioned phase transformations. Undoubtedly, further structure and chemical bonding sensitive investigations such as selected area diffraction (SAD), Raman spectroscopy and XPS among others are needed to understand the nanoindentation behaviour of Si, including structural inhomogeneities in the subsurface layer.

Oscillations of the total SSF divergence, P''-h, total plastic SSF divergence, H''-h, and elastic normal SSF divergence, E''-h, shown in Fig. 1(b-d) highlight the fine structure of the plastic deformation mechanisms occurring underneath the loaded indenter during a single indentation test. The P''-h, H''-h and E''-h curves for all tests demonstrated quasi-regular oscillations around the abscissa where at each intersection point the divergence amplitude changed its sign. Positive amplitude means that the indented sample underneath the indenter within the interface between the encasing hydrostatic core and plastic zone undergoes a strain (work) hardening plastic deformation whereas negative divergence amplitude indicates different plastic deformation leading to strain (work) softening effects. Divergence oscillation am-

plitude quickly decreased as the penetration depth increased, indicating that material bulk properties began to dominate over the subsurface layer influence at larger penetration depths. The small amplitude of *P″-h* curve at h > 250 nm manifested that the steady state region was reached where indents became self-similar when indenter load was increasing. Meanwhile, the hardness-displacement, *H-h*, curve reached the saturation plateau but the plastic SSF gradient, *H′-h*, had very low-amplitude oscillations around zero (not shown). The oscillations of *H″-h* and *E″-h* curves were out of phase (Fig. 1(c)), which was in good agreement with the general nature of the elastic-plastic deformation events. Note that any discrete plastic deformation event has its own early elastic phase manifested here by the positive elastic SSF divergence (*E″(h)* > 0). Elastic phase can happen only up to the point where the elastic limit is not yet exceeded. After the local yield point is reached, the elastic strain triggers the corresponding plastic one.

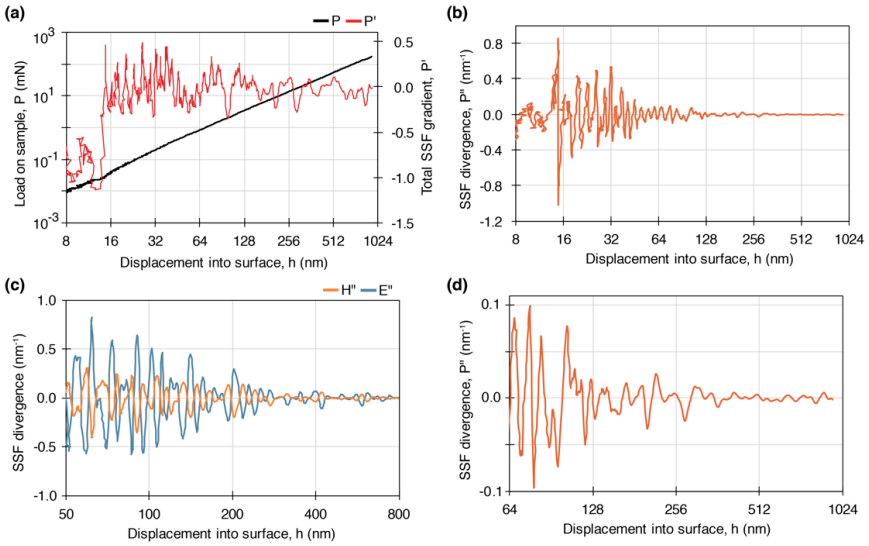

Fig. 1. Total stress-strain field gradient and divergence oscillations of the single indentation test in the Si(100) sample: **(a)** A typical example of the load-displacement, *P-h*, curve (black) and the total SSF gradient, *P′-h*, curve (red) obtained from a single indentation test in the CSM mode; **(b)** Total SSF divergence oscillations obtained from the same measurement; **(c)** Plastic normal (*H″-h* curve, orange) and elastic normal (*E″-h* curve, blue) SSF divergence oscillations calculated from the same measurement; **(d)** Close-up of the total SSF divergence low amplitude oscillations from (b) at greater penetration depths.

3.2 SSF Gradient-Divergence Analysis of the Averaged Dataset

The SSF gradients calculated from the averaged load-displacement, *P-h*, stiffness-displacement, *S-h*, hardness-displacement, *H-h*, and elastic modulus-displacement, *E-h*, curves (Fig. 2) were much smoother than the ones obtained from individual single measurements; the oscillations were much less salient. Similarly, the oscillations of the averaged SSF divergence could still be detected albeit they were markedly smaller in amplitude compared to the single indentation tests (not shown; see also Ref. 10). The smoothening occurred due to the averaging because the oscil-

lations of the single indentation tests were stochastically shifted in phase (along the *h*-axis) with respect to each other transforming the averaged SSF gradients into more quiet peak-valley system. However, it was still possible to detect less subtle fluctuations in the SSF gradients despite the averaging: each of the averaged SSF gradient curves demonstrated a sequence of peaks-valleys (see Fig. 2). The system of peaks-valleys in the averaged SSF gradient curves could be likely attributed to interfaces between mechanically distinct local microzones within the sample.

3.3 Calculation of True Hardness and True Elastic Modulus

One of the first questions that arise during the nanoindentation experiment is how to extract true hardness and true elastic modulus from raw indentation data such as the *P*-*h* and *S*-*h* curves or even from *H*-*h* and *E*-*h* curves calculated by Oliver-Pharr method [15] when they all are functions of the displacement within the whole displacement range. In this context, the averaged SSF gradients *H'*-*h* and *E'*-*h* play a significant role. In accordance with strain gradient plasticity concept, one should search for some special H_t- and E_t-points on the *H*-*h* and *E*-*h* curves where the corresponding strain gradients *H'*-*h* and *E'*-*h* intersect the displacement *h*-axis or approach it as close as possible, i.e., to find the deepest valley on the *H'*-*h* and *E'*-*h* curves if such intersection h_t-points do not exist. In the absence of the SSF gradients (i.e., zero gradient) *H*-*h* and *E*-*h* curves in the vicinity of these h_t-points may become state functions where apparent hardness, *H*, or elastic modulus, *E*, does not differ from the true hardness, H_t, or true elastic modulus, E_t. Following this approach, the true values of the hardness and elastic modulus could be read out from Fig. 2(c,d) as H_t = 12.3 GPa and E_t = 221.5 GPa, respectively.

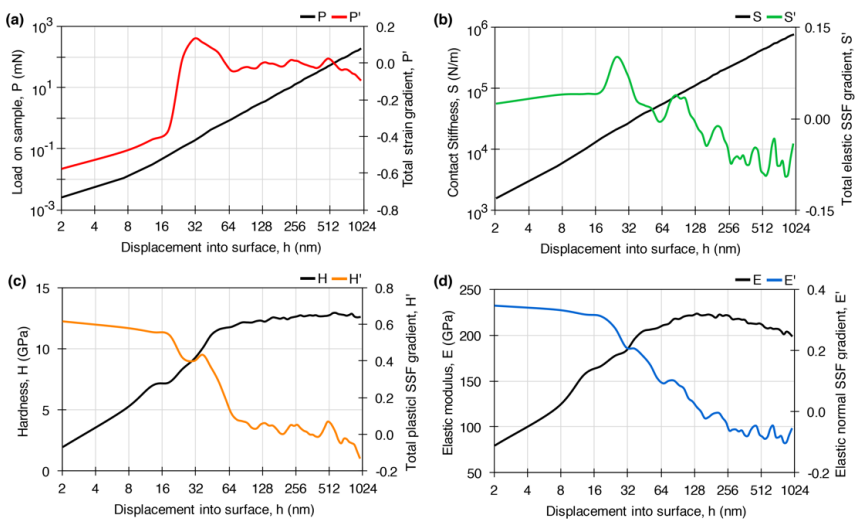

Fig. 2. Primary indentation characteristics and their corresponding SSF gradients calculated from the averaged datasets of the Si(100) sample (n=8 tests): **(a)** Load-displacement, *P*-*h*, curve and total SSF gradient-displacement, *P'*-*h*, curve; **(b)** Stiffness-displacement, *S*-*h*, and total elastic SSF gradient-displacement, *S'*-*h*, curve; **(c)** Hardness-displacement, *H*-*h*, and total plastic SSF gradient-displacement, *H'*-*h*, curve; **(d)** Elastic modulus-displacement, *E*-*h*, curve and elastic normal SSF gradient-displacement, *E'*-*h*, curve.

Some weak SSF gradient fluctuations up and down the h-axis may occur when the indentation steady state is reached. In such a case, several h_{ti}-points may appear instead of one critical h_t-point. If the h_{ti}-points are closely placed to each other and corresponding values of the primary function (e.g., H_{ti} or E_{ti}) differ only slightly then the mean value of them would be the most reasonable choice for the true value. Otherwise, when the h_{ti}-points are distantly placed then one should seek the global maximum on the indentation primary function to determine the corresponding true value.

4. CONCLUSIONS

In this study, a simple approach to assess stress-strain field (SSF) gradient and divergence from nanoindentation measurement data has been derived and applied in the analysis of the nanoindentation response of a bulk silicon sample. The total, *P′-h,* total elastic, *S′-h,* total plastic, *H′-h*, and elastic normal, *E′-h*, SSF gradients have been revealed as dimensionless functions by the SSF gradient-divergence approach using specific derivatives calculated of the empirically obtained primary indentation functions (load-displacement, *P-h*, stiffness-displacement, *S-h*, hardness-displacement, *H-h*, and elastic modulus-displacement, *E-h*, curves, respectively). In contrast to their corresponding primary functions, the SSF gradients did not contain slowly changing trends determined to some extent by indenter geometry and indentation mode. Instead, relatively weak undulations and peculiarities of the SSF caused by sample heterogeneities, interfaces between mechanically different mediums, phase transformations or other plastic deformation effects could now be observed more clearly and analysed. The traditionally measured averaged datasets describe the indentation response in a somewhat integrated way where the fine undulations can be to a large extent concealed. Therefore, it was important to analyse single indentation test datasets prior to any smoothening and averaging. Further applications of the strain gradient-divergence analysis approach to several steel, glass and fused silica samples, which are chosen as representative materials of bulk solids commonly used as substrates for thin film deposition, are demonstrated in the second part of the present research [10].

The stress-strain gradient approach is not limited to the investigation of bulk solids. The most promising application, in fact, is related to the studies of layered thin film coating structures, where the assessment of the mechanical properties is especially challenging [7], [19], [20]. The influences of the substrate surface are present throughout the thin film sample, which can result in indentation size effects that preclude a precise estimation of the true hardness and true elastic modulus. Furthermore, the thin films can be highly heterogeneous with gradients of changing chemical composition throughout the sample. In such cases, the strain gradient representations can be used to define an analytic criterion for determining the indentation depth at which the apparent values are the closest to the true values: the true mechanical properties should be read out in the most homogeneous regions within the sample, i.e., at the penetration depths where the strain gradient is the closest to zero. Stress-strain gradient representations can also inform about the microstructure of the thin film by revealing a pattern of strain gradient peaks and valleys which

could indicate interfaces between sub-layers of the thin film and relative "in-bulk" zones within the layered thin film structure, respectively.

ACKNOWLEDGEMENTS

The authors express their gratitude to Dr. Roberts Zabels at the Institute of Solid State Physics, University of Latvia for providing the datasets of the nanoindentation and AFM experiments, and Prof. Janis Maniks for encouraging and helpful discussions.

REFERENCES

1. Fischer-Cripps, A. (2004). *Nanoindentation*. New York: Springer-Verlag.
2. Oyen, M.L., & Cook, R.F. (2009). A practical guide for analysis of nanoindentation data. *J. Mech. Behav. Biomed., 2*, 396–407.
3. Guo, Y.B., & Warren, A.W. (2005). Microscale mechanical behavior of the subsurface by finishing processes. *J. Manuf. Sci. Eng.*, *126*, 333–338.
4. Warren, A.W., Guo, Y.B., & Weaver, M.L. (2006). The influence of machining induced residual stress and phase transformation on the measurement of subsurface mechanical behavior using nanoindentation. *Surf. Coat. Tech., 200*, 3459–3467.
5. Michel, J.P., Ivanovska, I.L., Gibbons, M.M., Klug, W.S., Knobler, C.M., Wuite, G.J.L., & Schmid, C.F. (2006). Nanoindentation studies of full and empty viral capsids and the effects of capsid protein mutations on elasticity and strength. *Proc. Natl. Acad. Sci. USA, 103*, 6184–6189.
6. Sangwal, K. (2000). On the reverse indentation size effect and microhardness measurement of solids. *Mater. Chem. Phys., 63*, 145–152.
7. Kanders, U., Kanders, K., Maniks, J., Mitin, V., Kovalenko, V., Nazarovs, P., & Erts, D. (2015). Nanoindentation response analysis of Cu-rich carbon–copper composite films deposited by PVD technique. *Surf. Coat. Tech., 280,* 308–316.
8. Saha, R., & Nix, W.D. (2002). Effects of the substrate on the determination of thin film mechanical properties by nanoindentation. *Acta Mater.*, *50*, 23–38.
9. Manika, I., & Maniks, J. (2008). Effect of substrate hardness and film structure on indentation depth criteria for film hardness testing. *J. Phys. D. Appl. Phys., 41*, 074010.
10. Kanders, U., & Kanders, K. (2017). Nanoindentation response analysis of thin film substrates-II: Strain hardening-softening oscillations in subsurface layer. *Proc. Latv. Acad. Sci. B, 71*.
11. Fleck, N., & Hutchinson, J. (1997). Strain gradient plasticity. *Adv. Appl. Mech., 33*, 295–362.
12. Gao, H., Huang, Y., & Nix, W.D. (1999). Modeling plasticity at the micrometer scale. *Naturwissenschaften*, *86*, 507–515.
13. Johnson, K.L. (1970). The correlation of indentation experiments. *J. Mech. Phys. Solids*, *18*, 115–126.
14. Johnson, K.L. (1985). *Contact Mechanics*. Cambridge: Cambridge University Press.
15. Hay, J.L., Agee, P., & Herbert, E.G. (2010). Continuous stiffness measurement during instrumented indentation testing. *Exp. Techniques, 34*, 86–94.
16. Oliver, W., & Pharr, G. (2004). Measurement of hardness and elastic modulus by instrumented indentation: Advances in understanding and refinements to methodology. *J. Mater. Res.*, *19*, 3–20.

17. Zarudi, I., Zhang, L.C., Cheong, W.C.D., & Yu, T.X. (2005). The difference of phase distributions in silicon after indentation with Berkovich and spherical indenters. *Acta Mater.*, *53*, 4795–4800.
18. Yan, J., Takahashi, H., Gai, X., Harada, H., Tamaki, J., & Kuriyagawa, T. (2006). Load effects on the phase transformation of single-crystal silicon during nanoindentation tests. *Mater. Sci. Eng. A*, *423*, 19–23.
19. Misra, A., Verdier, M., Lu, Y.C., Kung, H., Mitchell, T.E., Nastasi, M., & Embury, J.D. (1998). Structure and mechanical properties of Cu-X (X= Nb, Cr, Ni) nanolayered composites. *Scripta Mater., 39*, 555–560.
20. Maniks, J., Mitin, V., Kanders, U., Kovalenko, V., Nazarovs, P., Baitimirova, M., Meija, R., Zabels, R., Kundzins, K., & Erts, D. (2015). Deformation behavior and interfacial sliding in carbon/copper nanocomposite films deposited by high power DC magnetron sputtering. *Surf. Coat. Tech.*, *276*, 279–285.

VAKUUMA PĀRKLĀJUMU SUBSTRĀTU NANOINDENTĒŠANAS DATU ANALĪZE-I: DEFORMĀCIJAS GRADIENTA-DIVERĢENCES METODE

U. Kanders, K. Kanders

K o p s a v i l k u m s

Nanoindentēšanas metode tiek plaši izmantota mikromehānisku sistēmu mehānisko īpašību pētīšanai, kā, piem., maza izmēra objektu vai maza tilpuma materiālu cietība, Junga modulis, elastības limits vai slodžu izturība, u.c. parametri. Šajā pētījumā ir izstrādāta vienkārša empīriska metode, kā no parauga slogošanas-atslogošanas datiem nanoindentēšanas eksperimentā var izskaitļot indentēšanas radīto deformācijas gradientu un diverģenci. Šādai pieejai ir neaizvietojama praktiska nozīme, kas ļauj daudz drošāk analizēt materiālu cietības un Junga moduļa raksturlīknes atkarībā no indentora iespiešanās dziļuma. Deformācijas gradients un diverģence skaidri norāda uz deformācijas procesu īpatnībām nano-izmēra tilpumos, kas saistīti ar materiālu lokāliem uzkaldināšanas un atkaldināšanas procesiem, piem., masīvu materiālu pievirsmas slānī. Šajā rakstā gradienta-diverģences analīzes metode tika izmantota, lai analizētu masīvu silikona paraugu. Šī pētījuma otrajā daļā (U. Kanders, K. Kanders: Vakuuma pārklājumu substrātu nanoindentēšanas datu analīze-II: Uzkaldināšanas-atkaldināšanas oscilācijas pievirsmas slānī.) šī metode tika izmantota, lai analizētu dažādu tēraudu, stikla un kausēta kvarca masīvu paraugu pievirsmas deformācijas procesus.

09.01.2017.